Monte Carlo Conversion for the Australian Primary Standard of Absorbed Dose to Water in High Energy Photon Beams

Tracy Elizabeth Wright

Thesis submitted for the degree of Master of Science (Medical Physics)

School of Physical Sciences
University of Adelaide

August 2015

TABLE OF CONTENTS

ABSTRACT

Radiotherapy treatment entails the delivery of large radiation doses to malignant tissues in the human body. These doses must be accurate in order to balance tumour control and damage to healthy tissues. The first step in accurate dosimetry is the calibration of radiation dosemeters by the national primary standards laboratory. Any uncertainties in this fundamental step will be passed on to every radiotherapy patient in Australia. Absorbed dose to water is the quantity used for the calibration of linear accelerator (linac) beams and many treatment planning systems. The work in this thesis is devoted to the establishment of the Australian primary standard of absorbed dose with clinically used high energy photon beams, and in particular to the Monte Carlo methods employed.

The work described occurs in three stages: modelling of the accelerator head, modelling of the graphite calorimeter and water phantom in order to determine absorbed dose to water, and validation of the Australian primary standard of absorbed dose to water by comparison with international primary standards laboratories.

The EGSnrc user codes BEAMnrc and DOSXYZnrc have been used for this work. The linac model is built using BEAMnrc component modules to match the components inside the real linac head. Validation of the linac model is performed by comparison of modelled PDDs and profiles with their measured counterparts.

The ARPANSA measurement of absorbed dose to water is the basis for all absorbed dose calibrations performed in Australia. The determination of absorbed dose to water by ARPANSA begins with a measurement of absorbed dose to graphite. A graphite calorimeter is used to measure the heating caused by irradiation in order to determine the absorbed dose to graphite. The measured dose to graphite is converted to absorbed dose to water by a factor evaluated by Monte Carlo calculations. The conversion factor is calculated as the ratio of two components: the modelled dose to water at the reference depth in the absence of an ionisation chamber and the modelled dose to the core (the sensitive element) of the calorimeter. The calorimeter is modelled to replicate the device used with all Mylar coatings and air and vacuum gaps included. The physical calorimeter geometry is confirmed by kilovoltage imaging and gap corrections are calculated and

compared to similar calorimeters in the literature for added confidence in the calorimeter model.

The final stage of method validation involves comparisons with measurements performed by other researchers. Primarily this is done by comparing the determination of absorbed dose to water with other primary standards laboratories. This thesis presents a direct comparison performed in the ARPANSA linac beams and two indirect comparisons with measurements by the other participants completed at their respective laboratories. In all cases the ARPANSA measurement was lower than comparison participant. The difference between the ARPANSA measurement and that of the other participant was 0.02 to 0.46% at 6 MV, 0.41 to 0.76% at 10 MV and 0.68 to 0.80% at 18 MV. All results for the 6 MV beam agreed within 1σ. At 10 MV one measurement agreed within 1σ. The remaining 10 MV comparisons and all comparisons at 18 MV differed by between 1σ and 2σ. In addition to the validation methods, a detailed assessment of the uncertainties in the Monte Carlo conversion factor and the resulting calibration of an ionisation chamber are presented. The uncertainty in the calibration coefficient of an ionisation chamber after interpolation to the clinical beam energy is between 0.6 and 0.7%.

The resulting quantity of absorbed dose to water is used to determine the calibration factor, $N_{D,w}$, of an ionisation chamber. The ratio of calibration factors measured in a linac beam and in ^{60}Co is the measured energy correction factor, k_Q, at the linac beam quality. In addition to comparisons of absorbed dose to water, the measured k_Q values for commonly used ionisation chambers have been compared to measured and modelled values of k_Q published elsewhere.

An important consideration in changing from using the IAEA k_Q values published in the TRS-398 Code of Practice to directly measured k_Q values at megavoltage energies is the shift caused in chamber $N_{D,w}$ factors. This varies with chamber type and beam quality. In this thesis four chamber types were considered: the NE 2571 Farmer chamber, and the NE 2611A, PTW 30013 and IBA FC65-G Farmer-type chambers. At 6 MV the expected shift in $N_{D,w}$ ranges from -0.2% to -0.9% across the four chamber types. For the 10 MV beam quality the expected shift is -0.8% to -1.3% and at 18 MV -1.1% to -1.4% is expected. The reason for these differences is twofold. The IAEA k_Q values are typically higher than measured k_Q values published by many authors. In addition to this, the ARPANSA measured k_Q values tend to be low compared to the average of many measured k_Q values. Regardless of the reasons, the shift has an impact on the beam calibration of clinical linacs and the implications of this effect are discussed.

DECLARATION

I certify that this work contains no material which has been accepted for the award of any other degree or diploma in my name in any university or other tertiary institution and, to the best of my knowledge and belief, contains no material previously published or written by another person, except where due reference has been made in the text. In addition, I certify that no part of this work will, in the future, be used in a submission in my name for any other degree or diploma in any university or other tertiary institution without the prior approval of the University of Adelaide and where applicable, any partner institution responsible for the joint award of this degree.

I give consent to the copy of my thesis when deposited in the University Library, being made available for loan and photocopying, subject to the provisions of the Copyright Act 1968.

The author acknowledges that copyright of published work contained with this thesis resides with the copyright holder(s) of those works.

I also give permission for the digital version of my thesis to be made available on the web, via the University's digital research repository, the Library Search and also through web search engines, unless permission has been granted by the University to restrict access for a period of time.

_____ _____

Tracy Elizabeth Wright Date

ACKNOWLEDGEMENTS

First and foremost, I must thank all my supervisors. To my ARPANSA supervisors Jessica Lye and Duncan Butler, thank you for your ongoing support. In addition to your invaluable technical advice, your encouragement has helped me through the emotional challenges of a postgraduate degree. I could not have wished for two better supervisors to support me and keep me on track. And to my Adelaide-based supervisors Judith Pollard, Scott Penfold and Mohammad Mohammadi, thank you also for your support. Thank you to Judith for your help navigating the University system from a distance, and your understanding with a few surprise phone calls throughout the Masters journey. Thank you to Scott for your advice and clinical viewpoint which has been an important aspect of this work. And to Mohammad, thank you for your help early on and for our thought-provoking discussions.

Thank you to all my colleagues in the ARPANSA Radiotherapy section who have contributed through measurements and technical expertise throughout the project. In particular, the work performed by Ganesan Ramanathan and Peter Harty in the area of calorimetry is the key measurement for the primary standard of absorbed dose to water. Without your measurements my work toward the Monte Carlo conversion factor would be meaningless. And to the rest of my colleagues Chris Oliver, Viliami Takau and David Webb, thank you for your support and advice. I feel lucky to work with such a great group of people.

A huge thank you goes to Sean Reilly from the eResearch South Australia helpdesk for his help in making the EGSnrc submission scripts compatible with both the Hydra and Corvus supercomputers at different stages of the project. Without his help the modelling would have taken significantly longer and may not have been possible. Thanks also to Paul Marks for his assistance with the imaging for the calorimeter geometry validation and Keith Pardarlis for help converting the peer-reviewed publication to single page images for insertion into the Appendix.

For the advice I have received, I would like to thank Dave Rogers for a brief but valuable discussion on the uncertainties in the EGSnrc graphite stopping powers. Thanks also to the anonymous reviewers of the paper produced as a result of this work. Their comments and suggestions helped to improve the method and clarity of the uncertainty analysis in the

article and subsequently in this thesis. Lastly, thank you to Ivan Williams for your advice in the review of this thesis. It has improved the quality of the writing within and been a valuable lesson about writing structure.

Finally, I would like to thank my family. To my mum, thank you for your love, encouragement and understanding. And to my wonderful husband, I can't thank you enough for your stability, love and compassion. I'm sure I couldn't have made it without your endless support and encouragement.

LIST OF FIGURES

LIST OF TABLES

LIST OF ABBREVIATIONS

AAPM	American Association of Physicists in Medicine
ACPSEM	Australasian College of Physical Scientists and Engineers in Medicine
ANSTO	Australian Nuclear Science and Technology Organisation
ARPANSA	Australian Radiation Protection and Nuclear Safety Agency
BIPM	Bureau International des Poids et Mesures
DVM	Digital volt meter
ECUT	Electron cut off energy
ENEA-INMRI	Ente per le Nuove Tecnologie, l'Energia e l'Ambiente – Istituto Nazionale di Metrologia delle Radiazioni Ionizzanti (Italy)
EPOM	Effective point of measurement
ESDM	Estimated standard deviation of the mean
FWHM	Full-width half-maximum
IAEA	International Atomic Energy Agency
IMRT	Intensity-modulated radiation therapy
K6	Key comparison BIPM.RI(I)-K6
KCDB	Key comparison database
k_Q	Energy correction factor
KRISS	Korea Research Institute of Standards and Science (Korea)
Linac	Linear accelerator
LNE-LNHB	Laboratoire National de Métrologie et d'Essais – Laboratoire National Henri Becquerel (France)
MC	Monte Carlo
METAS	Swiss Federal Office of Metrology and Accreditation (Switzerland)
$N_{D,w}$	Calibration coefficient for the absorbed dose to water
NIST	National Institute of Standards and Technology (USA)

NMI	National measurement institute
NMIJ	National Metrology Institute of Japan
NPL	National Physical Laboratory (UK)
NRC	National Research Council (Canada)
PCUT	Photon cut off energy
PDD	Percentage depth dose
PDI	Percentage depth ionisation
PTB	Physikalisch-Technische Bundesanstalt (Germany)
QA	Quality assurance
SSD	Source-to-surface distance
TG-51	AAPM's TG-51 protocol for clinical reference dosimetry of high-energy photon and electron beams
TRS-398	IAEA Code of Practice for absorbed dose determination in external beam radiotherapy (Technical Report Series No. 398)
XCOM	NIST photon cross-section database

CHAPTER 1 INTRODUCTION

The basis of all radiotherapy treatments is a calibration that is traceable to a primary standard of air kerma or absorbed dose to water. In Australia, the Australian Radiation Protection and Nuclear Safety Agency (ARPANSA) is responsible for the dissemination of these standards. For high energy photon beams, clinics in Australia follow the guidelines in the International Atomic Energy Agency (IAEA) Code of Practice, TRS-398 (Andreo *et al.*, 2000) for a calibration in terms of absorbed dose to water. Currently, the reference for absorbed dose calibrations is a ^{60}Co beam and an energy correction factor is used to transfer the calibration to the user energies.

Calibrations at megavoltage photon energies similar to those used in clinics offer a number of advantages compared to ^{60}Co calibrations. A ^{60}Co beam is very different to clinical linear accelerator (linac) beams in energy, dose rate and temporal distribution. Energy correction factors require extrapolation from the average ^{60}Co beam energy and do not account for individual chamber characteristics. Additionally, TRS-398 recommends direct megavoltage calibrations as the preferred method, subject to availability.

The aim of this work is twofold. The first aim is to develop and validate the Monte Carlo models required to commission high energy photon reference beams for calibrations in terms of absorbed dose to water. The second aim is to compare the ARPANSA determination of absorbed dose to water in high energy photon beams to that of other national measurement institutes (NMIs) to assess the agreement with the international community.

This thesis is structured with intermediate results presented throughout the report. Chapter 2 gives an overview of the methods used for primary standard dosimetry and their application to the clinical user. For primary standards of absorbed dose to graphite, this chapter also describes the different methods used to convert the measured absorbed dose in graphite to the quantity of interest to the clinical user: absorbed dose to water.

Chapter 3 describes the model of the ARPANSA linac in detail. It includes a discussion of the selection of model parameters and consideration of variance reduction techniques. A description of the method of model validation and choice of commissioning tolerances is

also included. A key part of the model validation was the comparison of modelled dose distributions with benchmark percentage depth dose (PDD) and profile measurements performed by other ARPANSA staff members when the linac was first installed. This data set is the reference for the linac output (in terms of energy, flatness and symmetry) and regular QA and maintenance ensures the linac remains within an allowed tolerance of this condition. As such, it is the ideal benchmark of the linac model. Comparisons of measured and modelled PDD plots and profiles at 10 cm depth are shown for all beam energies. The graphite PDDs include a depth-dependent recombination correction. The measurements for this correction were performed by other ARPANSA staff.

The conversion of absorbed dose to graphite to absorbed dose to water is presented in Chapter 4. Here, the graphite calorimeter and its model are described along with the methods used to validate the model. The model of the water phantom and its validation are also covered in this chapter. Finally, the conversion of absorbed dose from graphite to water is described. A description of the methods used for graphite calorimetry are included in the chapter in order to describe the process completely, however this is not my work. My colleagues Ganesan Ramanathan and Peter Harty completed all the calorimetry measurements and analyses to obtain the absorbed dose to graphite. These measurements go hand-in-hand with the Monte Carlo conversion factor to obtain the absorbed dose to water. The Monte Carlo conversion method is explained and resulting conversion factors for the three high energy photon beams are presented. The measurement of the dimensions and density of the graphite plates used in the calorimetry work were performed by other ARPANSA staff. In addition, the imaging used for validation of the calorimeter geometry was assisted by another ARPANSA staff member. The validation of the conversion factor using the alternate method of cavity ionisation theory is also described in Chapter 4. The ionisation chamber calibration coefficients in graphite used for the cavity ionisation theory analysis were measured by other ARPANSA staff.

The most important result of the thesis is the comparison of the ARPANSA method against other NMIs, including that of the Bureau International des Poids et Mesures (BIPM) who provide the reference value for international equivalence. This is the subject of Chapter 5. All comparisons include contributions from many staff members. With the exception of the calibration coefficients in ^{60}Co for the NMIJ comparison, all comparison measurements were performed by other staff from ARPANSA and the other participating laboratories. Measurements cannot be compared without a thorough understanding of the uncertainty in the measurement. Hence, the uncertainty analysis is also included in Chapter 5. The uncertainties associated with the calorimetry measurements and ionisation chamber

calibration coefficients were calculated by other ARPANSA staff and I calculated the uncertainty contributions from all Monte Carlo aspects of the work. The measured energy corrections of four commonly used ionisation chambers are compared to other published values determined by calculation, measurement and Monte Carlo modelling.

In Chapter 6 the key results of the thesis are discussed. The consistency of international comparisons is considered and the ARPANSA uncertainties are compared to other NMIs that use similar methods. The importance of absolute dose accuracy and consistency of dose measurements are discussed from the perspective of patient treatments and outcomes. The expected shift in the calibration coefficients when moving from a ^{60}Co reference beam to the high energy photon beams is also assessed.

Lastly, conclusions of the thesis are drawn in Chapter 7. The complete set of linac model validation profiles at all depths is provided in Appendix B.

CHAPTER 2 PRIMARY STANDARDS FOR RADIATION DOSE

It is estimated that approximately 130,000 new patients will be diagnosed with cancer in 2015 in Australia (Australian Institute of Health and Welfare, 2012). Of those patients, about 50% would benefit from treatment with radiotherapy (Delaney *et al.*, 2005). Radiotherapy outcomes rely heavily on the accuracy of the radiation dose delivered in order to achieve a fine balance between good tumour control and minimal damage to healthy tissues (Nahum and Kutcher, 2007). The first step in accurate dosimetry is the calibration of radiation dosemeters by a national primary standards laboratory. Any uncertainties in this fundamental step will be disseminated to treatment facilities and their patients around Australia.

The human body is largely composed of water, which is a good surrogate for human tissue. For this reason, absorbed dose to water is the quantity used for the calibration of linac beams and many treatment planning systems (Ma and Li, 2011). In addition, water is widely available and reproducible so it makes an ideal standard material (Seuntjens *et al.*, 2005). An increasing number of planning systems calculate dose to medium (i.e. dose to the patient tissues) rather than dose to water. The use of absorbed dose to medium is a widely debated topic and currently the recommended quantity for beam calibrations remains absorbed dose to water (Andreo *et al.*, 2000). The work in this thesis is devoted to the establishment of the Australian primary standard of absorbed dose with clinically used high energy photon beams, and in particular the Monte Carlo methods employed.

2.1 Consistency of international doses

International consistency of absorbed dose is ensured through a network of primary and secondary standards laboratories and a programme of international comparisons. The BIPM oversees the comparison programme between participating countries and manages the key comparison database (KCDB) (Key Comparison Database, 2014). The BIPM provides the reference value for the comparisons, either directly in key comparisons or indirectly through a linking laboratory, and participants report their variation from the

reference value in terms of their degrees of equivalence. Comparisons are repeated on an approximately ten year cycle.

There are two ongoing international key comparisons of interest for the quantity of absorbed dose. The first is the key comparison BIPM.RI(I).K4 for the measurement of absorbed dose to water in ^{60}Co (Allisy-Roberts and Burns, 2005). This comparison has been running for over 20 years and has provided a basis for absorbed dose calibrations over this time. The second is a comparison of absorbed dose to water in high energy photon beams (key comparison BIPM.RI(I)-K6) that began in 2009 (Picard *et al.*, 2013c).

In participating countries, standards of absorbed dose are disseminated to radiotherapy clinics through NMIs that have determined their degrees of equivalence to the BIPM. In some cases a clinic will provide an ionisation chamber directly to the NMI for a calibration against the primary standard. Alternatively, the NMI will offer a calibration to one or more secondary standards laboratories which then provide traceable calibrations to the clinics. The second option is common in large countries where a single NMI cannot provide enough calibrations to satisfy the demand. In Australia, most calibrations are provided by the NMI (ARPANSA). A secondary standards laboratory at the Australian Nuclear Science and Technology Organisation (ANSTO) can also provide calibrations.

2.2 Calibration of clinical chambers

The Australian primary standard of absorbed dose is a graphite calorimeter. ARPANSA maintains a calibration service for radiotherapy clinics whereby the clinic's dosemeter is calibrated against the primary standard in a ^{60}Co reference beam. An energy correction factor, k_Q, is required to extrapolate a calibration in a ^{60}Co beam to the megavoltage x-rays produced by clinical linacs. The k_Q of an ionisation chamber can be calculated or determined experimentally.

Clinics in Australia follow the IAEA TRS-398 Code of Practice (Andreo *et al.*, 2000). According to TRS-398, the preferred method of obtaining k_Q is by a ratio of measured calibration factors in the reference beam and at or close to the user beam quality, according to the following equation:

$$k_Q = \frac{N_{\mathrm{D,w},Q_{\mathrm{user}}}}{N_{\mathrm{D,w}}} \tag{2.1}$$

where $N_{\mathrm{D,w},Q_{\mathrm{user}}}$ is the calibration factor measured at the user beam quality and $N_{\mathrm{D,w}}$ is the calibration factor measured in a ^{60}Co beam. In the absence of measured k_Q values, TRS-398 provides calculated correction factors for most types of ionisation chambers available commercially. The TRS-398 k_Q values are calculated using the approximation

$$k_Q \approx \frac{\left(s_{\mathrm{w,air}}\right)_Q}{\left(s_{\mathrm{w,air}}\right)} \cdot \frac{p_Q}{p}, \tag{2.2}$$

where $\left(s_{\mathrm{w,air}}\right)_Q$ and $\left(s_{\mathrm{w,air}}\right)$ are the spectrum averaged ratios of Spencer-Attix water/air stopping power ratios at beam qualities Q and ^{60}Co respectively and p_Q and p are the ionisation chamber perturbation correction factors at beam qualities Q and ^{60}Co respectively. Both p_Q and p are comprised of the corrections p_{wall} (for the difference between medium and chamber wall materials), p_{cav} (for the change in electron fluence within the chamber cavity due to the presence of the chamber), p_{dis} (for the displacement of material by the chamber cavity) and p_{cel} (for non-air equivalence of the central electrode). Stem effects are not accounted for in the calculation. The calculated k_Q values are tabulated for beam qualities of $\mathrm{TPR}_{20,10}$ from 0.50 to 0.84. Users interpolate between the tabulated points to obtain the k_Q value for their $\mathrm{TPR}_{20,10}$ and chamber type. TRS-398 estimates the standard uncertainty in k_Q to be 1%.

The uncertainty in the k_Q values that account for the difference between the ^{60}Co beam and the user beam quality is a limiting factor in the accuracy that can be achieved in clinical dose measurements. In addition to the large uncertainty in k_Q, the ^{60}Co beam is inherently different to a megavoltage x-ray beam. Where a ^{60}Co beam consists of two gamma ray energies and a small amount of head and source scatter, the linac beam has a continuous spectrum from near zero to the peak accelerating energy of the beam. ^{60}Co delivers a continuous beam; a linac delivers a pulsed beam with a peak dose rate roughly three orders of magnitude larger than ^{60}Co. Furthermore, the direct calibration method would also take into account deviations in individual chamber construction from the nominal design, and allows new chamber designs to be calibrated where tabulated corrections do not exist. Recognising this, ARPANSA has installed a medical linac to allow direct calibrations against a primary standard at user energies.

2.3 Clinical equipment for dose measurement

Reference class instruments are chambers with the required accuracy, precision and stability to provide the traceability link between the primary standards laboratory and a

clinical linac output. Andreo *et al.* (2000) define a reference chamber as a*n instrument of the highest metrological quality available at a given location, from which measurements at that location are derived*. A field instrument is one that is cross-calibrated periodically in the clinical beam against the reference chamber and then used for routine measurements. Recommendations are provided for the specification of reference class chambers by McEwen *et al.* (2014). The NE 2571 is the original Farmer chamber and has been one of the commonly-used reference class chambers. It is, however, not waterproof like many of the newer chamber types. The requirement for a waterproof sleeve adds uncertainty to the measurement and, more importantly in a clinical setting complicates the chamber setup.

2.4 Primary standard dosimetry

In the international metrology community, a primary standard is usually based on the measurement of a fundamental quantity. According to the BIPM,

> *"A **primary standard** is a standard that is designated or widely acknowledged as having the highest metrological qualities and whose value is accepted without reference to other standards of the same quantity."*
> *(http://www.bipm.org/en/convention/wmd/2004/standards.html, accessed 10 April 2014)*

Historically, primary standards of absorbed dose have been based on air-filled ionisation chambers (ionometry standards), chemical dosimetry (Fricke solutions) and calorimetry (graphite or water calorimeters).

In an ionometry standard, the charge collected within the chamber cavity is converted to absorbed dose using the average energy required to release an ion pair in air, W_{air}. The absorbed dose to water is determined by applying the graphite to air stopping power ratio, $s_{c,air}$, and a perturbation correction for the presence of the chamber in the water phantom. Ionometry standards have been used by the BIPM and the Institute of Nuclear Energy Research (Taiwan) but are not currently used as the primary standard for absorbed dose in megavoltage photon beams in any laboratories (Seuntjens and Duane, 2009).

In a Fricke solution, radiation converts Fe^{2+} ions to Fe^{3+} ions by oxidisation (Oldham, 2007). The chemical yield of Fe^{3+} (G_{Fe}^{3+}) is measured by the change in optical density of the solution. The solution is calibrated in terms of $1/(\varepsilon G)_{Fe^{3+}}$ where ε is the molar extinction coefficient. This quantity has been well characterised and is considered

acceptable for the purposes of a primary standard. The absorbed dose to the Fricke solution is usually converted to absorbed dose to water by Monte Carlo calculations (Seuntjens and Duane, 2009). Standards using ferrous sulfate (Fricke) solutions have been used by the German standards laboratory, Physikalisch-Technische Bundesanstalt (PTB), in the past, but they have now moved to water calorimetry as their primary standard method.

In calorimetry a temperature increase is measured in the sensitive volume of a calorimeter. The temperature is measured by thermistors embedded within the calorimeter. In radiation dosimetry the temperature rise is caused by irradiation of the calorimeter and can be related to the energy deposited. Fundamentally the specific heat capacity can be used to calculate the energy deposited from the temperature rise. In practice though most calorimeter designs include electrical heaters so that a known amount of energy can be deposited in the calorimeter in order to calibrate the temperature rise.

Although absorbed dose to water is the desired quantity, in the early days of calorimetry impurities and the heat defect (see *Water Calorimetry* below) limited the accuracy that could be achieved with water calorimeters. Graphite calorimeters provided an alternative with a material that had similar radiological properties to water. Now many of the difficulties with water calorimetry have been overcome and both water and graphite calorimeters are in use (Seuntjens and Duane, 2009). The following paragraphs provide a brief summary of the two calorimetry methods. A detailed discussion of the ARPANSA graphite calorimetry method is provided in Chapter 4.

Water calorimetry

The most common type of water calorimeter currently used for primary standard dosimetry is a sealed water calorimeter. These consist of a small volume of highly purified water enclosed in a glass vessel, often with the ability to bubble gases through the water. The vessel sits within a larger container of water maintained at 4°C to minimise convection. Heat dissipation occurs through convective heat transfer and conduction. A key principle of water calorimetry is the low rate of thermal conduction in water. The absorbed dose to a point in the water inside the glass vessel is measured by thermistors in close proximity to the point of interest (Seuntjens and Duane, 2009).

A heat defect in water arises from reactions that occur during irradiation due to impurities or dissolved gases in the water. The defect is the difference between the energy absorbed in the medium and the energy converted to heat that causes the water temperature to rise.

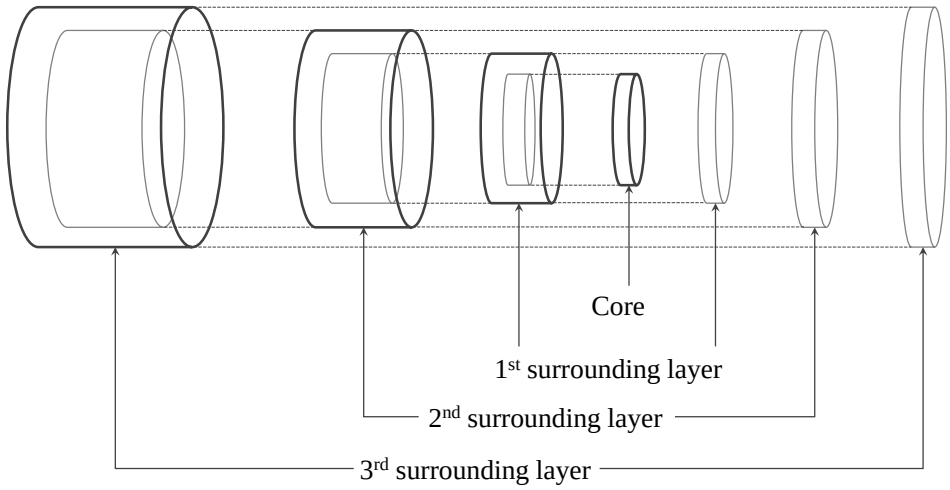

Figure 2-1: An exploded diagram of a generic calorimeter with the core surrounded by three isolated graphite bodies. Each surface except that of the core would be coated with aluminised Mylar. The bodies would be separated by small pieces of non-conducting material to ensure conductive isolation and the entire assembly would be sealed and evacuated to remove air from the gaps.

Some impurities cause an unstable heat defect, while for others the heat defect is stable and can be corrected. The purified water inside the vessel can be saturated with hydrogen or hydrogen peroxide enabling a consistent correction. Corrections are also applied for heat transfer due to conduction and convection, perturbation caused by non-water materials, the difference between doses at the point of interest and at the measurement point and the difference in density of the calorimeter and the water phantom used for calibration (due to temperature) (Seuntjens and Duane, 2009). One disadvantage that remains for water calorimetry is the specific heat capacity of water compared to graphite. The specific heat of water is almost six times that of graphite (Lide, 2009), so a much larger dose is required in water for the same temperature rise.

Graphite calorimetry

A graphite calorimeter consists of a measurement volume, known as the core, surrounded by thermally isolated layers of graphite. The bodies are separated by evacuated gaps and provide insulation from the external temperature. Aluminised Mylar coatings on all internal graphite surfaces except the core can further reduce the transfer of heat between the bodies. A simple depiction of a graphite calorimeter is shown in Figure 2-1.

Corrections are required with graphite calorimeters to correct for the reference position, beam uniformity across the detector area and calorimeter inhomogeneities leading to variations in the photon fluence. Where the reference position or scaled reference depths

cannot be achieved with the calorimeter setup, corrections are used to convert the measurements to the reference conditions. With the dose being averaged over the area of the core, the beam profile becomes important in determining the dose to a point on the central axis. A radial non-uniformity correction accounts for variations across the beam profile from the central axis dose. The presence of gaps and non-graphite materials in the calorimeter perturb the photon fluence from that in a solid phantom of graphite. A gap correction is used to correct for this effect. The corrections applied to the ARPANSA calorimeter will be described in detail in Section 4.1.4.

The average absorbed dose over the entire core area is measured by thermistors embedded at the edges of the core. It is not possible to measure the dose to a point in the core due to the high thermal conductivity of graphite. For this reason, the mass of the core must be known with a high degree of precision. Measurements are usually conducted with a beam that completely covers the core area.

The NMIs referenced in this thesis are listed in Table 2-1. The NPL, LNE-LNHB, METAS and NRC currently offer direct megavoltage calibration services (Seuntjens and Duane, 2009). Several other national standards laboratories are preparing to offer direct megavoltage calibrations. The NRC, PTB and NIST use water calorimeters as their primary standards in high energy photon beams (Picard *et al.*, 2010; Picard *et al.*, 2011; Picard *et al.*, 2013a). The BIPM, NPL, and ARPANSA use graphite calorimeters (Picard *et al.*, 2015) while LNE-LNHB (Pearce *et al.*, 2011) use an average of doses derived from graphite and water calorimeters. In addition to those laboratories with established calorimetry methods in high energy photon beams NMIJ and ENEA-INMRI use a graphite calorimeter as their primary standard in ^{60}Co (Guerra *et al.*, 1996; Morishita *et al.*, 2013),

Table 2-1: List of national measurement institute abbreviations and countries.

Abbreviation	Laboratory name	Country
BIPM	Bureau International des Poids et Mesures	International
ENEA-INMRI	Ente per le Nuove Tecnologie, l'Energia e l'Ambiente - Istituto Nazionale di Metrologia delle Radiazioni Ionizzanti	Italy
LNE-LNHB	Laboratoire National de Métrologie et d'Essais – Laboratoire National Henri Becquerel	France
METAS	Swiss Federal Office of Metrology and Accreditation	Switzerland
NIST	National Institute of Standards and Technology	USA
NMIJ	National Metrology Institute of Japan	Japan
NPL	National Physical Laboratory	UK
NRC	National Research Council	Canada
PTB	Physikalisch-Technische Bundesanstalt	Germany

and are both scheduled for participation in the BIPM.RI(I)-K6 comparison (Absorbed Dose Working Group, 2013). A significant downfall of graphite calorimetry when compared to water calorimetry is the medium in which the absorbed dose is measured. Graphite calorimeters measure the absorbed dose to graphite, which is not the quantity of interest. The measured dose must be converted to absorbed dose to water to make it useful for radiotherapy applications.

2.5 Conversion from absorbed dose to graphite to absorbed dose to water

Absorbed dose to graphite can be converted to absorbed dose to water by calculations based on ratios of electron density or stopping power ratios, or by Monte Carlo calculations of doses in the two media. Earlier standards for absorbed dose to water in ^{60}Co radiation used either the photon fluence scaling theorem or the cavity ionisation theory to achieve dose to water (Wise, 2001). The photon fluence scaling theorem predicts that the absorbed dose in one medium will be the same as that in a second medium at a depth that is scaled by the ratio of electron densities, according to the equation:

$$x' = \frac{\rho(e^-)}{\rho(e^-)'} x \tag{2.3}$$

where x and x' are the depths in the first and second medium respectively, and $\rho(e^-)$ and $\rho(e)'$ are the electron densities in the first and second medium respectively (Pruitt and Loevinger, 1982). The photon fluence scaling theorem relies on accurate knowledge of the position of the radiation source and assumes that Compton scattering is the only type of interaction in the phantoms (Huntley *et al.*, 1998). These conditions make this method less suitable for use in a linac beam.

Cavity ionisation theory uses ratios of stopping power ratios and perturbation corrections to convert the absorbed dose in graphite to absorbed dose in water at an equivalent depth (in terms of g/cm^2). In the cavity ionisation theory method, an ionisation chamber is calibrated for absorbed dose to graphite in a graphite phantom at the same depth and source to detector distance as the calorimeter core. The absorbed dose to water calibration coefficient is then calculated using ionisation chamber theory. The dose to water is calculated using the graphite dose and ratios of mean restricted stopping power ratios and perturbation corrections in graphite and water, according to:

$$\dot{D}_w = \dot{D}_g \frac{I_w}{I_g} \frac{\bar{s}_{\mathrm{w,a}}}{\bar{s}_{\mathrm{g,a}}} \cdot \frac{[p_{wall} p_{dis} p_{cel}]}{[p_{wall} p_{dis} p_{cel}]'} \tag{2.4}$$

where $\dot{D}_w$ and $\dot{D}_g$ are the absorbed dose rates in water and graphite respectively, I_w is the measured chamber current in the water phantom and I_g is the chamber current measured in a graphite phantom, $\bar{s}_{w,a}$ is the ratio of mean restricted stopping powers of water and air at the reference depth in water, $\bar{s}_{g,a}$ the ratio of mean restricted stopping powers of graphite and air at the reference depth in graphite, p_{wall} the perturbation correction for the difference between phantom and chamber wall materials, p_{dis} the perturbation correction for the displacement of phantom material by the chamber cavity and p_{cel} is the perturbation correction for non-air equivalence of the central electrode (Wise, 2001). Unprimed factors are evaluated at the reference point in water and double-primed factors at the reference point in graphite.

Cavity theory assumes that electrons deposit their energy locally. This assumption is incorrect for delta (high energy) electrons. Restricted stopping powers aim to exclude delta electrons by including only energy losses less than a cut-off energy, Δ. The value of Δ should be equivalent to the energy required by an electron to travel the mean chord length of the cavity (Nahum, 2007). An energy cutoff Δ of 10 keV is commonly used for thimble chambers of order a few mm (Andreo *et al.*, 2000).

2.6 Review of Monte Carlo methods to convert absorbed dose to graphite to absorbed dose to water

The principle of a Monte Carlo conversion from absorbed dose to graphite to absorbed dose to water is quite simple: models are established for the graphite calorimeter and the water phantom and doses are calculated in both models. The Monte Carlo code used, method of implementation and additional steps in the process vary among institutions. Monte Carlo methods are used by all laboratories with graphite calorimeters. Some rely entirely on Monte Carlo calculations to obtain absorbed dose to water from the measured absorbed dose to graphite while others apply Monte Carlo calculated corrections and otherwise use the more traditional methods of dose conversion.

The BIPM use the PENELOPE Monte Carlo code (Salvat *et al.*, 2009) and use an intermediate step with a ratio of ionisation chamber measurements in graphite and water phantoms. In order to achieve this they model doses in the core of the graphite calorimeter ($D_{c,MC}$), an ionisation chamber in graphite ($D_{cav,c,MC}$) and water ($D_{cav,w,MC}$) phantoms and in a water phantom ($D_{w,MC}$). The absorbed dose to water ($D_{w,BIPM}$) is calculated by the following:

$$D_{\mathrm{w,BIPM}} = D_{\mathrm{c}} \frac{Q_{\mathrm{w}}}{Q_{\mathrm{g}}} \left(\frac{D_{\mathrm{w}}}{D_{\mathrm{c}}} \right)^{\mathrm{MC}} \left(\frac{D_{\mathrm{cav,c}}}{D_{\mathrm{cav,w}}} \right)^{\mathrm{MC}} k_{\mathrm{m}} \tag{2.5}$$

where D_{c} is the measured absorbed dose to the core, Q_{w} and Q_{g} are the measured charge in the water and graphite phantoms respectively and k_{rn} is a correction for the radial non-uniformity of the beam (Picard *et al.*, 2014).

The NPL also make use of an ionisation chamber in their calculation of absorbed dose to water (Pearce *et al.*, 2011). The measured calorimeter dose (D_{core}) is converted to the absorbed dose to a homogenous graphite phantom ($D_{\mathrm{g,cal}}$) using a modelled calorimeter gap correction (k_{gap}) according to Equation 2.6.

$$D_{\mathrm{g,cal}} = D_{\mathrm{core}} k_{\mathrm{gap}} \prod_i k_{i,\mathrm{cal}} \tag{2.6}$$

The gap correction is modelled using the EGSnrc user code DOSRZnrc. $\prod_i k_{i,\mathrm{cal}}$ are corrections for impurities in the core, beam uniformity and heat loss. An NE2611 ionisation chamber is calibrated for absorbed dose to graphite ($D_{\mathrm{g,ch}}$) by Equation 2.7 to obtain a calibration factor, $N_{\mathrm{D,g}}$ according to Equation 2.8. $Q_{\mathrm{g,ch}}$ is the charge measured in the determination of the absorbed dose to graphite calibration factor. $\prod_i k_i$ are additional corrections.

$$D_{\mathrm{g,ch}} = D_{\mathrm{g,cal}} \prod_i k_i \tag{2.7}$$

$$N_{\mathrm{D,g}} = \frac{D_{\mathrm{g,ch}}}{Q_{\mathrm{g,ch}}} \tag{2.8}$$

The absorbed dose to water calibration factor ($N_{\mathrm{D,w,NPL}}$) is achieved with a ratio of measured charges in water (Q_{w}) and graphite (Q_{g}) phantoms and a ratio of Monte Carlo calculated doses in both materials as follows:

$$N_{\mathrm{D,w,NPL}} = N_{\mathrm{D,g}} \frac{Q_{\mathrm{g}}}{Q_{\mathrm{w}}} \frac{D_{\mathrm{w}}}{D_{\mathrm{g}}} \tag{2.9}$$

where D_{w} and D_{g} are the Monte Carlo doses in water and graphite phantoms respectively. The doses are calculated using DOSXYZnrc.

The method used at NMIJ to obtain absorbed dose to water in a ^{60}Co beam relies on cavity theory, but uses a calorimeter gap correction calculated with the EGS5 Monte Carlo code

(Hirayama *et al.*, 2005) and a ^{60}Co spectrum calculated using the MCNP4 code (Briesmeister, 2000). Likewise, at ENEA the conversion to absorbed dose to water in ^{60}Co is assessed using cavity theory with Monte Carlo calculated gap corrections. The gap corrections are calculated using DOSRZnrc. In addition, the photon energy fluence spectra and perturbation due to the presence of the ionisation chamber have been calculated using FLURZnrc, another user code of EGSnrc. The modelled spectra were used to calculate the ratio of mean mass energy absorption coefficients in graphite and water (Guerra *et al.*, 2007).

At ARPANSA we have adopted a conceptually and experimentally simple approach that does not use an intermediate chamber. Instead there is a direct modelled conversion of the calorimeter dose to water dose. This method was established in 2010 for ^{60}Co calibrations (Lye *et al.*, 2013) and is here extended to megavoltage linac beams. Both the calorimeter and water phantom are modelled using the EGSnrc user code BEAMnrc. The gaps are explicitly included in the calorimeter model so no gap correction is required. A radial non-uniformity correction (k_{rn}) is applied to allow for variations in the beam profile compared to the central axis. The absorbed dose to water ($D_{\mathrm{w,ARP}}$) is calculated by:

$$D_{\mathrm{w,ARP}} = D_{\mathrm{c}} \left(\frac{D_{\mathrm{w}}}{D_{\mathrm{c}}} \right)^{\mathrm{MC}} k_{\mathrm{m}} \qquad (2.10)$$

where D_{c} is the dose measured in the calorimeter core and $(D_{\mathrm{w}}/D_{\mathrm{c}})^{\mathrm{MC}}$ is the ratio of Monte Carlo calculated dose to water in a water phantom and dose to the calorimeter core.

LNE-LNHB also use a direct modelled conversion for high energy photon beams, however the details of their method and associated uncertainties are yet to be published. The Korean standards laboratory, KRISS, is also developing a method using graphite calorimetry but little information is available on their method (Delaunay *et al.*, 2011).

2.7 Requirements for a Monte Carlo conversion

The direct Monte Carlo conversion approach requires exceptional accuracy from the Monte Carlo modelling. There are three key steps required to ensure the method is sound. Firstly, the input source (the linac model) must be validated to ensure it is an accurate representation of the real beam. Secondly, the models of the calorimeter and water phantom must be validated. Finally, the calculated conversion factor is meaningless

without a thorough evaluation of the uncertainties associated with the method. These steps are described in detail in Chapters 3, 4 and 5.

CHAPTER 3 LINAC MODELLING

Monte Carlo methods have been used to model medical linacs since the late 1970s (McCall *et al.*, 1978; Petti *et al.*, 1983). Although there are numerous codes available that are capable of modelling medical linacs (EGS4, MCNP, PENELOPE, EGSnrc, Geant4), EGSnrc (Kawrakow, 2000) is the most widely used code for this application today (Rogers, 2006). The EGSnrc user codes, BEAMnrc (Rogers *et al.*, 2007) and DOSXYZnrc (Walters *et al.*, 2007) have been used for this work. The general principle of modelling a linac is that a volume is divided into sections by boundaries and materials are assigned to the spaces within the boundaries. In BEAMnrc sections are easily delineated using pre-defined component modules. Particles (including photons) can be input as a source at a point, area or plane defined by the user. One by one, the particles are traced through the geometry that has been defined. The energy, position and direction of the particle are tracked as it moves through the geometry. The distance and direction a particle travels, and the interaction that occurs at the destination, are decided by probability tables based on photon cross-sections and electron and positron stopping powers. Any particles that are created are added to a stack. Once the original particle loses all its energy or exits the geometry, particles in the stack are traced before a new source particle (history) begins. The accuracy and precision of the results depends to a large extent on the number of histories used in the simulation.

Modelling a linac enables accurate calculation of the dose that is deposited by that linac in a medium of interest. Typical media include phantoms, patient CT data and dosemeters such as film or ionisation chambers. A phase space file can be created at a plane between the linac head and the medium for calculating dose. The energy and particle type, and the position and direction coordinates of every particle that reaches the plane are recorded in the phase space file. This file can then be used as an input source for many dose calculations. This approach simplifies dose calculations and saves considerable computation time, particularly for primary standards work where much of the work is performed using a 10×10 cm^2 reference field with a large number of particles required for statistical precision.

The EGSnrc parameters used for this work are described in Section 3.1, followed by a description of the ARPANSA linac model in Section 3.2 and the model validation process in Section 3.3.

3.1 Selection of options in EGSnrc

EGSnrc offers a number of options enabling the user to achieve the optimum balance between calculation speed and accuracy. These options for the beam transport parameters relate to the algorithms used for cross sections and travel between interactions, angular sampling options, energy cut-offs and other interaction options. The selected parameters are listed in Section 3.1.1. In addition to the selection of transport parameters, variance reduction techniques can improve the statistical uncertainty in the calculation without increasing the calculation time. Variance reduction techniques must be carefully selected to avoid errors in the results, and these are considered in Section 3.1.2.

3.1.1 EGSnrc parameters

The optimum selection of parameters was investigated by Lye (2012) and has not been repeated here. For most of the parameters the default settings for the BEAMnrc and DOSXYZnrc user codes were used. The two exceptions were the BEAMnrc bremsstrahlung angular sampling and the DOSXYZnrc boundary crossing algorithm. The BEAMnrc bremsstrahlung angular sampling was set to 'KM' which engaged the complete modified Koch-Motz 2BS equation (Rogers *et al.*, 2007). Ali *et al.* (2012) found the 'KM' setting was important for calculation accuracy when compared to the default 'Simple' setting which only uses the leading term of the KM equation. In DOSXYZnrc the EXACT boundary crossing algorithm was set so that boundary crossings occur in single scattering mode (Walters *et al.*, 2007).

The 521ICRU pegs4 data, which provide cross section data for electron energies down to 0.521 MeV, were used for all simulations. Consistent with this selection, values of global ECUT and PCUT were 0.521 and 0.01 respectively. Unless otherwise stated, the settings used for all the simulations in this study are listed in Table 3-1.

3.1.2 Variance reduction methods

The purpose of variance reduction techniques is to improve the efficiency of a calculation; that is, to reduce the variance of the result without increasing the number of histories required. Common methods for achieving this are modifying the likelihood of an interaction occurring or the number of particles created during an interaction (with the contribution of each particle reduced by a weighting factor). Resulting particles are known as 'low weight' particles, while particles with a weight of unity are described as being 'fat'. Much effort has been dedicated to ensuring these modifications do not change the result when compared to a calculation performed without any variance reduction techniques. A detailed discussion of the many variance reduction techniques available can be found in Seco and Verhaegen (2013). The model in this project used directional bremsstrahlung splitting and range rejection.

Table 3-1: Beam transport parameters used in BEAMnrc and DOSXYZnrc. Deviations from the default settings are marked by an asterisk (*).

Transport parameter	BEAMnrc	DOSXYZnrc
Global ECUT	0.521	0.521
Global PCUT	0.01	0.01
Global SMAX	5	5
ESTEPE	0.25	0.25
XIMAX	0.5	0.5
Boundary crossing algorithm	EXACT	EXACT*
Skin depth for BCA	3	3
Electron-step algorithm	PRESTA-II	PRESTA-II
Spin effects	On	On
Photon cross sections	SI	SI
Brems angular sampling	KM*	Simple
Brems cross sections	BH	BH
Bound Compton scattering	Off	Off
Compton cross sections	Default	Not specified
Pair angular sampling	Simple	Simple
Pair cross sections	BH	BH
Photoelectron angular sampling	Off	Off
Rayleigh scattering	Off	Off
Atomic relaxations	Off	Off
Electron impact ionization	Off	Off

Directional bremsstrahlung splitting

The purpose of bremsstrahlung splitting is to create many more particles and photons at the location of interest (phase space plane or dose scoring region) than would otherwise have reached that location for the same number of histories. Transport of electrons is much more time consuming than transport of photons so up to the exit surface of the flattening filter all electrons are fat and photons are split unless they are directed away from the region of interest.

Russian roulette is inherent in the directional bremsstrahlung splitting algorithm (Rogers *et al.*, 2007). In the Russian roulette implementation, low weight particles or photons that are not directed toward the region of interest are given a survival probability equal to their weight. Their survival is determined by a random number, and if they survive their weight is increased by the inverse of the survival probability (i.e. their weight becomes 1). This technique can also be used in combination with the uniform bremsstrahlung splitting or selective bremsstrahlung splitting algorithms, however these were not utilised for this project.

In the directional bremsstrahlung splitting algorithm the region of interest, or splitting field, is defined by a radius around the central axis at a given depth. When interactions occur that produce fat photons (bremsstrahlung and annihilation events, Compton events from fat photons) each resulting photon is split into N photons of weight $1/N$ and the properties of each photon are determined independently. For each photon, if it is directed toward the splitting field it remains a low weight photon. Any photons directed away from the splitting radius undergo Russian roulette and surviving photons have their weight increased by a factor of N. Low weight photons must survive Russian roulette (i.e. become fat) before they are allowed to undergo interactions that create electrons (Compton, pair production, photoelectric effect).

A Russian roulette plane is defined above an electron splitting plane. Electron splitting is optional but is required if the dose delivered by primary electrons is important in the calculation (i.e. in electron beams or surface dose calculations). Electron splitting was implemented in this model. Beyond the Russian roulette plane, Russian roulette is no longer applied. Rogers *et al.* (2007) recommend the electron splitting plane be located at the rear surface of the flattening filter. At the electron splitting plane all fat charged particles are split N times with resulting weights of $1/N$. This way all particles and photons reaching the splitting field have an equal weight of $1/N$.

A more thorough description of the directional bremsstrahlung splitting algorithm can be found in Rogers *et al.* (2007) and Kawrakow *et al.* (2004). For this project, directional bremsstrahlung splitting was implemented with a splitting number *N* of 500 and a splitting radius of 11 cm defined at a source to surface distance of 100 cm.

Charged particle range rejection

Range rejection is used to reduce the number of unnecessary calculations caused by tracking charged particles that can't escape their current region. If the residual range of the particle (the energy it will have at the boundary) is less than the cut-off energy, the history is terminated and the energy is deposited in the current region.

The use of range rejection neglects the production of bremsstrahlung photons that would carry energy out of the region. There is an option to restrict range rejection to particles below an energy threshold to limit the loss of bremsstrahlung photons. In BEAMnrc the threshold is called ESAVE. For this project ESAVE was set to 2 MeV everywhere except the target, and 0.521 MeV within the target. Sheikh-Bagheri *et al.* (2000) found that this selection included 99.9% of photons that reached the phantom surface.

3.2 ARPANSA linac model description

The ARPANSA linac was installed in 2009 with the primary purpose of providing calibrations at megavoltage energies to Australian radiotherapy centres. The linac, an Elekta Synergy, has a total of seven photon energies available through the use of different filter sets. Each filter set has three photon beam options. The set most commonly used offers nominal beams at 6 MV, 10 MV and 18 MV, selected to cover the beam qualities most commonly used in Australia. These beams have been modelled using BEAMnrc version 4 (revision 2.3.1).

Elekta has provided detailed specifications of the components in the linac head under a confidentiality agreement (Elekta, 2009). These specifications were originally used by Lye (2012) to build the linac model. Minor modifications have been made to the flattening filter and backscatter plate in this work. Although minor, the modifications require re-validation to ensure the models match the measured data within the required tolerances. Additional corrections have been made in the validation process. The measured PDD has been corrected for recombination and the density of the water in the model has been

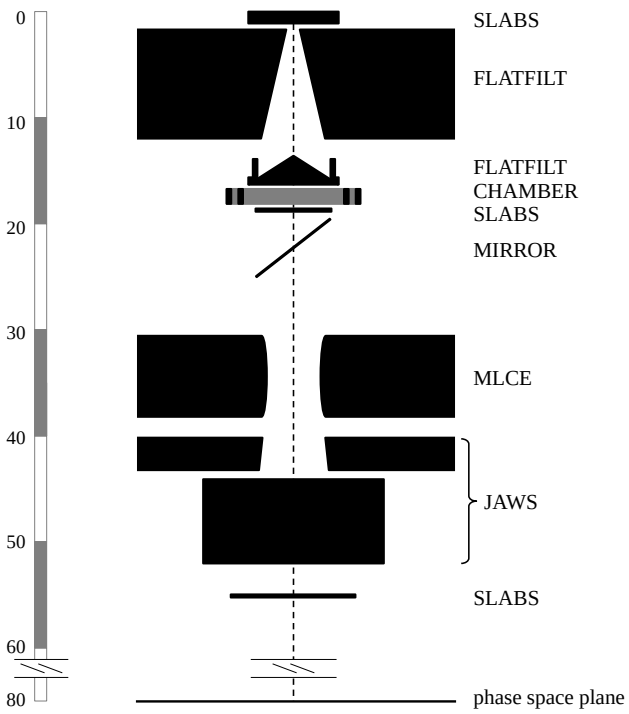

Figure 3-1: Schematic of the component modules in the BEAMnrc model of the ARPANSA linac.

modified to reflect the operating temperature of the linac laboratory. These modifications are outlined in Section 3.3.

Figure 3-1 shows a schematic of the components of the linac model. All components except the last SLABS module are standard in the linac head. For primary standard measurements an additional transmission chamber, a PTW 786 large size plane parallel transmission chamber, is mounted in the accessory tray to monitor short-term variations in the output of the linac. 3 mm of Perspex build-up is also included in front of the transmission chamber to increase the sensitivity of the chamber. The thin transmission chamber is not explicitly modelled but the Perspex plate is included (the final SLABS module).

The input source in the BEAMnrc model is a circular electron beam with a Gaussian radial distribution incident normal to the target component module on the central axis. The electron beam has a Gaussian distribution of electron energy with a full-width half-maximum (FWHM) of 500 keV based on manufacturer specifications. The two free parameters that were adjusted in order to match the model to measured dose distributions were the electron energy and the size of the electron beam (the spot size). At the field sizes used for validation (10×10 cm^2 and 30×30 cm^2) the model was quite insensitive to the spot size and a FWHM of 0.05 cm was used for all three beam qualities. It is acknowledged,

however, that for small fields the spot size and shape becomes critical in accurately modelling the linac beams (Scott *et al.*, 2009). When the linac model is extended to smaller fields the beam spot size will need to be re-visited.

The phase space file was scored at 80 cm from the front face of the target in air. This allows flexibility in the application of the phase space file as it can be used for isocentric or source-to-surface distance (SSD) setups. In an isocentric setup, the reference point is positioned at 100 cm from the source; in SSD setups the phantom surface is located at 100 cm from the source. The running parameters for each of the beam qualities for the 10×10 cm^2 fields are listed in Table 3-2. The 10×10 cm^2 fields are the most important for the calculation of the Monte Carlo conversion between absorbed dose to graphite and absorbed dose to water. The simulations were performed on the eResearch SA (eRSA) Corvus supercomputer (http://www.eresearchsa.edu.au/corvus_guide) and the run time (in total CPU hours) and the number of processors used are also listed in Table 3-2.

3.3 Validation of linac model

Detailed specifications of the linac provided by the manufacturer are an excellent starting point for a linac model. In fact, it would be virtually impossible to model the machine without this information. Nevertheless, following the specifications does not guarantee the model will match a specific linac. A thorough validation process is required to ensure the dose distributions produced by the model are consistent with the measured beam output. The following sections detail the methods used for the model validation, acceptance tolerances selected, corrections applied and the results of the validation.

Table 3-2: Running parameters for the production of phase space files for the 10×10 cm^2 fields used for validation and Monte Carlo calculated dose conversion.

Beam quality	6 MV	10 MV	18 MV
Histories	2×10^8	5×10^7	1×10^7
Run time (CPU hours)	176	82	23
Processors used	15	9	3
Particles in phase space file (*n*)	1.3×10^8	7.6×10^7	3.3×10^7
$\sqrt{n}$	1.1×10^4	8.7×10^3	5.7×10^3

3.3.1 Method of validation

A linac beam has a complex energy spectrum that varies with the depth in an absorbing medium and also with radial distance from the central axis. The energy spectra of all radiation beams change with depth as the beams lose energy due to absorption. In addition the conical flattening filter preferentially hardens the beam on the central axis. It produces a relatively flat beam necessary for conformal planning techniques that require a uniform dose distribution within the treatment volume. However, this also means the relationship between the dose on the central axis and the dose in the peripheral beam changes with depth due to the spectral differences across the beam profile.

Beam models are validated by comparing modelled distributions to measurements (Libby *et al.*, 1999). Typically, PDD curves and profiles of the beam in the in-line and cross-line directions in a water phantom are used as benchmarks for a modelled beam. A PDD verification assesses the match of the central axis beam energy through a range of depths. Profiles at multiple depths confirm the energy spectrum across the field. Additionally a graphite phantom PDD was matched for further confidence in the beam model and attenuation coefficients used in the EGSnrc code. Based on the comparison with measurements, the incident electron energy and electron beam spot size were adjusted in 2-parameter space until a good match with measurements was obtained. This method is consistent with that reported elsewhere (Lye *et al.*, 2012; Nutbrown *et al.*, 2002; Pearce *et al.*, 2011).

Water

Water percentage depth ionisation curves (PDIs) and profiles were measured in a scanning water phantom using a Wellhöfer CC13 ionisation chamber. The chamber has a radius of 3.0 mm and a volume of 0.13 cm^3. The thimble wall and collecting electrode are air-equivalent C-552 plastic. PDIs were measured with a field size of 10×10 cm^2.

An air filled ionisation chamber in a water phantom displaces the water at the position of measurement. The reduced attenuation in the lower density medium (air) causes an increased fluence when compared to that in water. With the chamber centred at the measurement position the PDI appears to penetrate deeper than the corresponding PDD as shown in Figure 3-2. There are two ways this effect can be corrected in an ionisation chamber measurement. One option is applying a correction, p_{dis}, to the ionisation chamber measurement. Beyond d_{max} a single p_{dis} correction is appropriate (Andreo and Nahum,

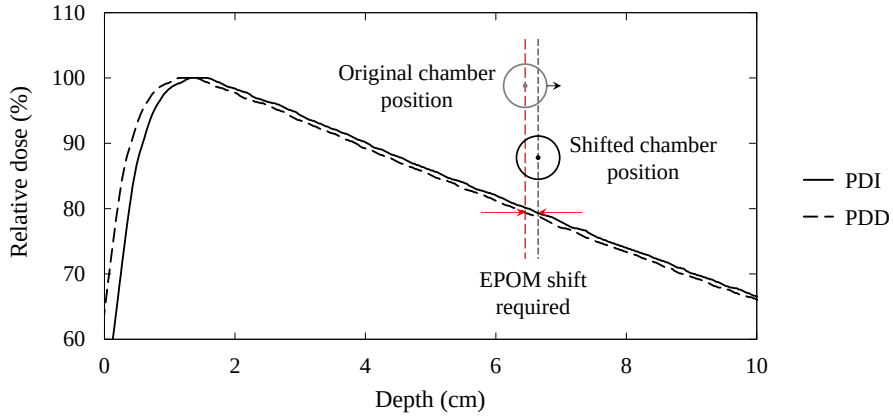

Figure 3-2: A PDI curve measured with a CC13 chamber and corresponding PDD curve after shifting the measured data by an EPOM of 1.8 mm (0.6*r*). The horizontal separation between the two curves shows the magnitude of the EPOM shift and the shift direction is indicated by the chamber positions shown. The original chamber position with the central electrode at the measurement position is shown in grey. The shifted chamber position with the measurement point (the red dashed line) upstream of the central electrode is shown in black.

2007). This approach is used later in this work where the cavity ionisation method is applied for method validation (see Chapter 4). An alternative is to shift the chamber deeper into the water phantom so that the effective point of measurement (EPOM) is upstream of the central electrode. This method is represented in Figure 3-2 and is the approach used here. The PDIs used for model validation were converted to PDDs by shifting the chamber to correct for the EPOM of the chamber and applying a depth-dependent recombination correction.

The EPOM shift employed was 0.6*r* toward the source (where *r* is the radius of the chamber cavity) as recommended by Andreo *et al.* (2000) and Almond *et al.* (1999). There is some conjecture on the required shift for chamber EPOM (McEwen *et al.*, 2008). Tessier and Kawrakow (2010) found the optimal EPOM shift varied depending on chamber type but for all chambers considered was less than 0.6*r* upstream with the major differences occurring before d_{max}. In the data presented by Tessier and Kawrakow there was little difference in the spread of the ratio of doses in water and chamber cavity at depths beyond d_{max}. Prior to comparing the PDDs, they were normalised to the reference depth of 10 cm. Given the agreement between measurement and modelled data is assessed between d_{max} and 20 cm depth, the normalisation method makes the matching process less sensitive to uncertainties in the selection of EPOM. Considering this and the spread of dose ratios for an EPOM shift of 0.6*r* reported by Tessier and Kawrakow (2010), the uncertainty in the dose at the reference depth due to EPOM errors in our specified range is estimated to be 0.1%. This includes variations in the stopping power ratios with depth and chamber perturbation effects. It should be mentioned that better accuracy could be achieved by

modelling the chamber in the water tank to compare directly to the measured PDI. This approach removes the need for corrections or approximations of the perturbation corrections and stopping power ratios, and in particular the change in these parameters with depth. This has not yet been completed and will be the subject of future work.

Profiles were measured for 10×10 cm^2 and 30×30 cm^2 fields at depths of d_{max}, 5 cm, 10 cm and 20 cm. Water PDDs and profiles were modelled using DOSXYZnrc (Walters *et al.*, 2007) with a water density of 0.99821 g/cm^3 for water at 20°C (Lide, 2009). For all 10×10 cm^2 fields the measurements and model were completed both with and without the external transmission chamber. All results shown here include the transmission chamber. The frame that supports the transmission chamber is smaller than the 30×30 cm^2 field so the profile validation for this field size was performed without the chamber in place. Measured and modelled PDDs in water for the 6 MV, 10 MV and 18 MV beams with 10×10 cm^2 are shown in Figure 3-3. The differences between the measured and modelled data are also shown in the figure and a linear fit is applied at the validation depths from d_{max} to 20 cm. The reduced range for the linear fit provides a large range around the reference depth of 10 cm. Depths beyond 20 cm were avoided due to the increased noise with diminishing dose. Profiles were normalised to the central axis dose. Comparisons of 10×10 cm^2 and 30×30 cm^2 profiles at a depth of 10 cm are shown in Figures 3-4 and 3-5. The comparisons of profiles at all other depths (d_{max}, 5 cm, 10 cm and 20 cm) are provided in Appendix B.

Graphite

Graphite PDIs were measured in a cylindrical graphite phantom using an NE 2611A ionisation chamber. As with water, the graphite PDDs were obtained by applying corrections to the measured data for EPOM and depth-dependent recombination. The EPOM in a graphite phantom was estimated by calculating the shift required to correct for the displacement correction factor, p''_{dis}, based on the gradient of the PDD at the reference depth. The value of p''_{dis} was calculated by the method described in Section 4.7 using Equation 4-6. Graphite PDDs were modelled using the FLATFILT component module in EGSnrc. The graphite PDDs were normalised to the reference depth in graphite of 5.465 cm (equivalent to 10 cm depth in water). Dose was scored in 1 cm steps along a central core with a radius of 0.4 cm to match the half-length of the ionisation chamber. Measured and modelled PDDs in graphite for the three beam energies are shown in Figure 3-6. The differences between the measured and modelled data are shown under the PDD in the figure.

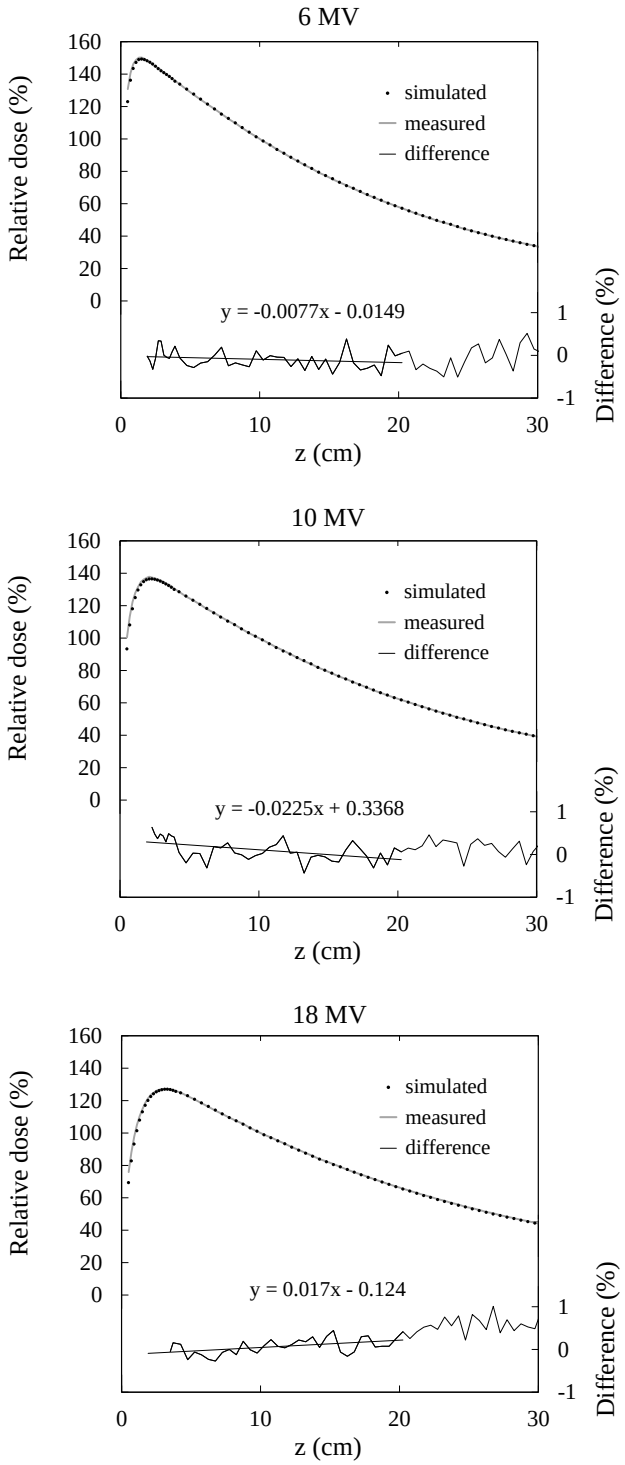

Figure 3-3: Comparison of measured and modelled PDDs in a water phantom for a 10×10 cm^2 field for three beam qualities. PDDs are normalised to the reference depth of 10 cm. The relative difference between the measured and simulated data is shown underneath each PDD.

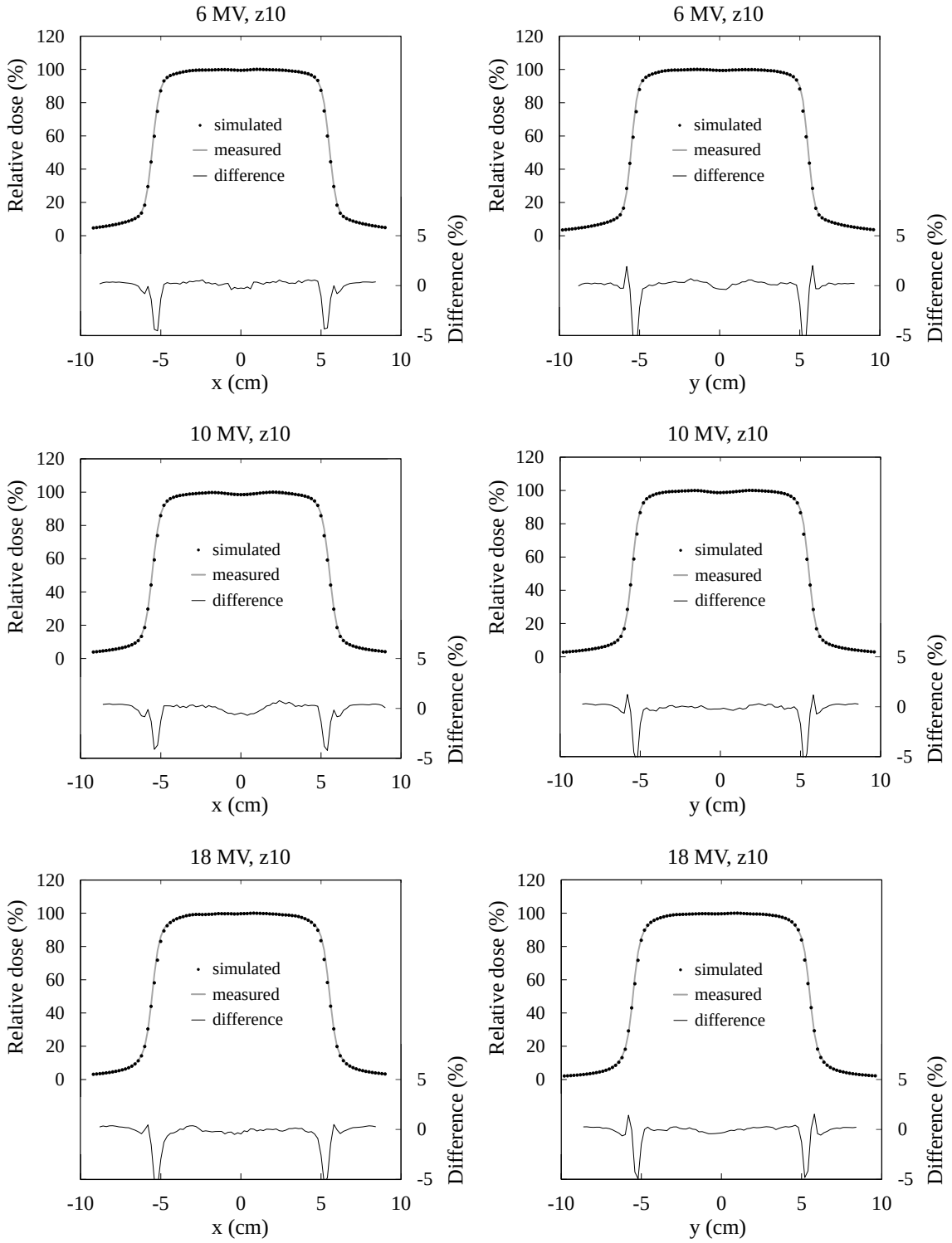

Figure 3-4: Comparison of measured and modelled profiles in water for the 6 MV, 10 MV and 18 MV beams at a depth of 10 cm for a 10×10 cm^2 field. The differences between measured and modelled profiles relative to the central axis dose are shown underneath each profile.

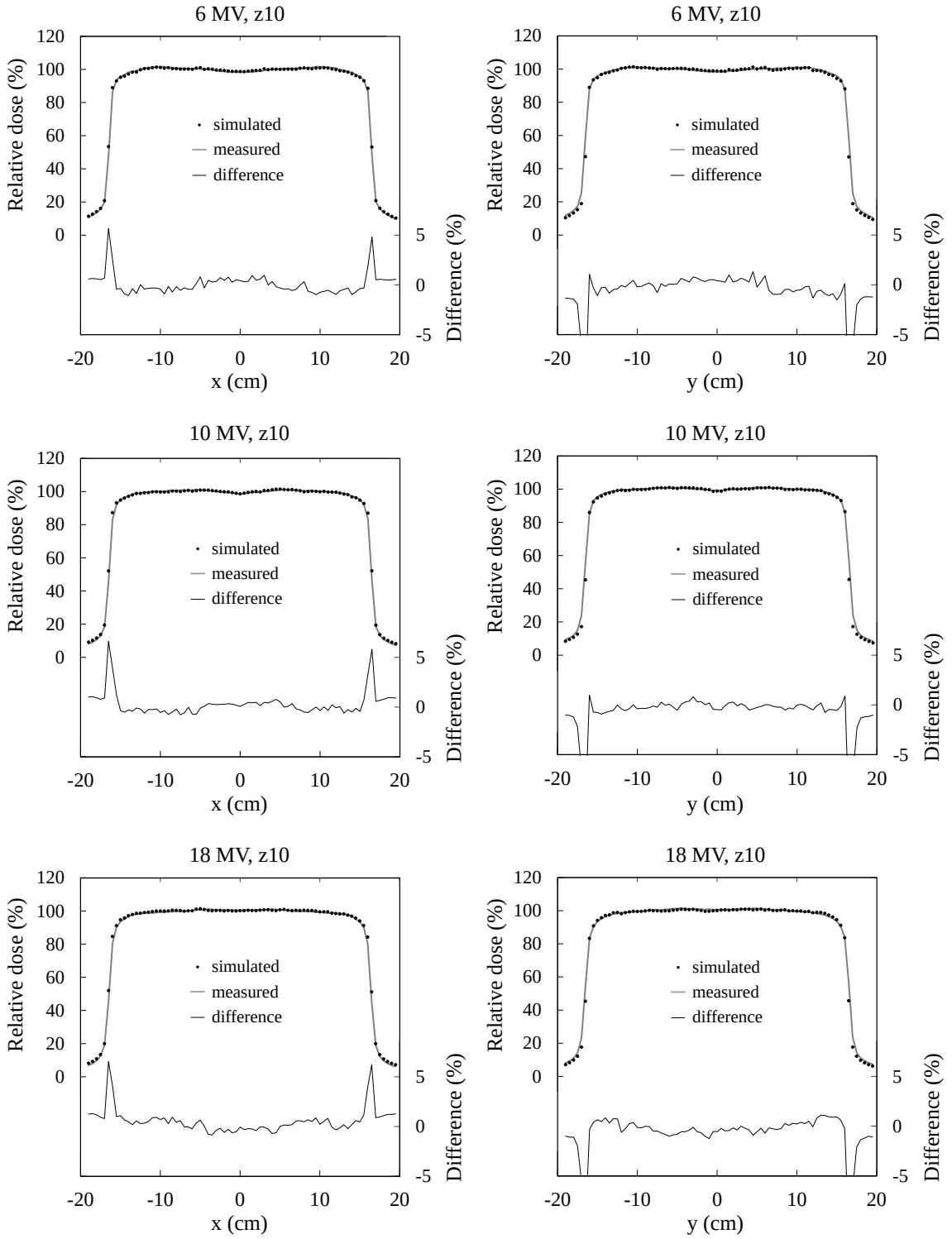

Figure 3-5: Comparison of measured and modelled profiles in water for the 6 MV, 10 MV and 18 MV beams at a depth of 10 cm for a 30×30 cm^2 field. The differences between measured and modelled profiles relative to the central axis dose are shown underneath each profile.

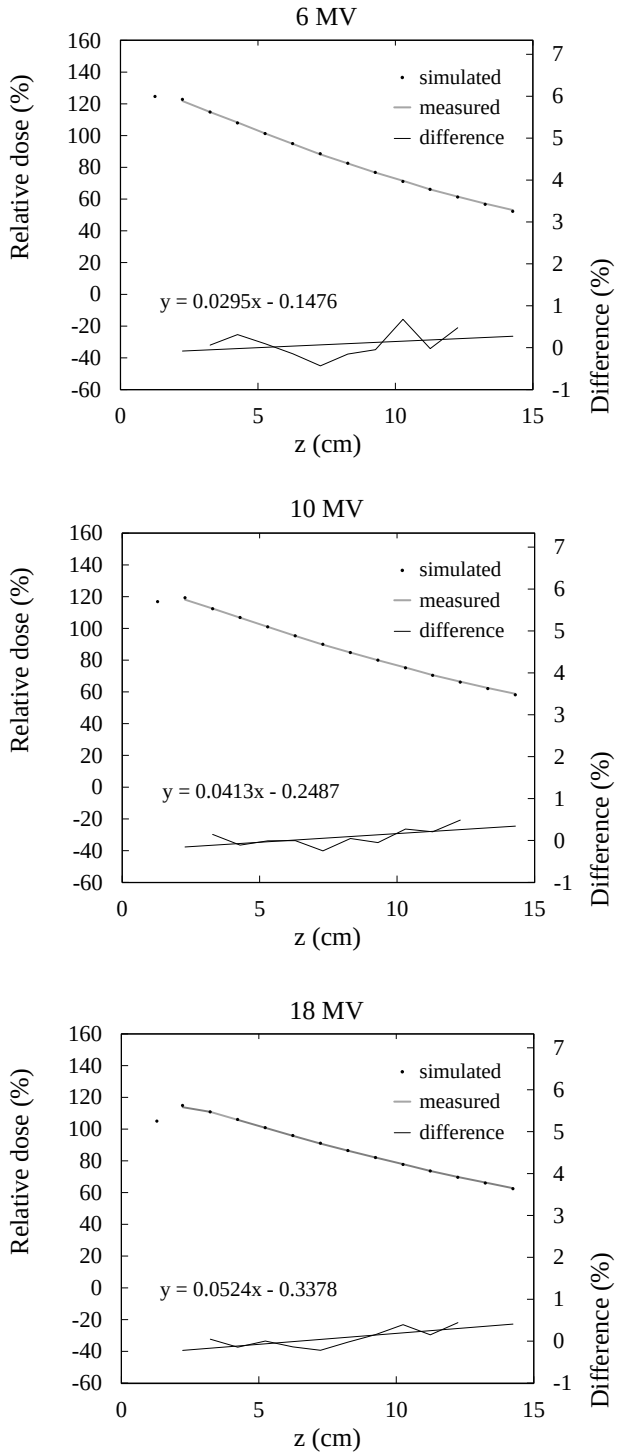

Figure 3-6: Comparison of measured and modelled PDDs in a graphite phantom for a 10×10 cm^2 field. PDDs are normalised to the reference depth of 5.465 cm. The relative difference between the measured and simulated data is shown underneath each PDD.

3.3.2 Matching tolerances

Tolerances typically used for the validation of beam models for radiotherapy applications include PDD local difference less than 1.5 – 2% at depths beyond d_{max}, central region local differences less than 2%, 10% local difference in the penumbra region or a 1 mm distance to agreement, field width difference less than 0.5 mm and 3.5% difference with respect to the central dose for regions outside the beam edge (Hartmann Siantar *et al.*, 2001; Mesbahi *et al.*, 2005; Rangel *et al.*, 2007; Verhaegen and Seuntjens, 2003). The purpose of beam modelling in the majority of these cases is to calculate doses for clinical treatment. The required uncertainty from a primary standard calibration is much lower and these tolerances are not sufficient. The critical area is a radius of 1 cm around the central axis. This is the calorimeter core area over which the dose ratio is calculated. In the commissioning of the beams in this work the primary focus has been on matching the PDDs in water and graphite, ideally to within 0.3% from d_{max} to the reference depth. The degree of mismatch between the modelled and measured PDDs in both materials is included in the uncertainty budget, as described in Section 5.1. The tolerance on the profiles is kept to <1% local dose difference in the central 80% of the field width.

3.3.3 Corrections and other considerations

Recombination

The principle of an ionisation chamber measurement is that *all* the charge created by irradiation of a small volume of air is collected. However, this is never correct. A small proportion of the ions that are created recombine before they are collected. The amount of recombination that occurs depends on the voltage that is applied to chamber, and more importantly the density of ions in the chamber volume. The recombination in a chamber is usually corrected for during absolute measurements, but for relative measurements (such as PDDs) it is usually ignored. The reduction in intensity in a water PDD from d_{max} to 20 cm depth causes a small but measurable reduction in the correction required for recombination. Similarly, in a graphite PDD the recombination correction reduces with depth. The recombination was obtained at depths of 3.12, 7, 10, 15 and 20 cm in water using the ‘two voltage’ technique (Andreo *et al.*, 2000). Data collected by ARPANSA staff were used to calculate the recombination in graphite at depths of 3.52, 7.52 and 11.52 cm. The results in both materials are shown in Figure 3-7. The correction varied by up to 0.4% across the range of depths relevant for matching the model. Second order polynomials

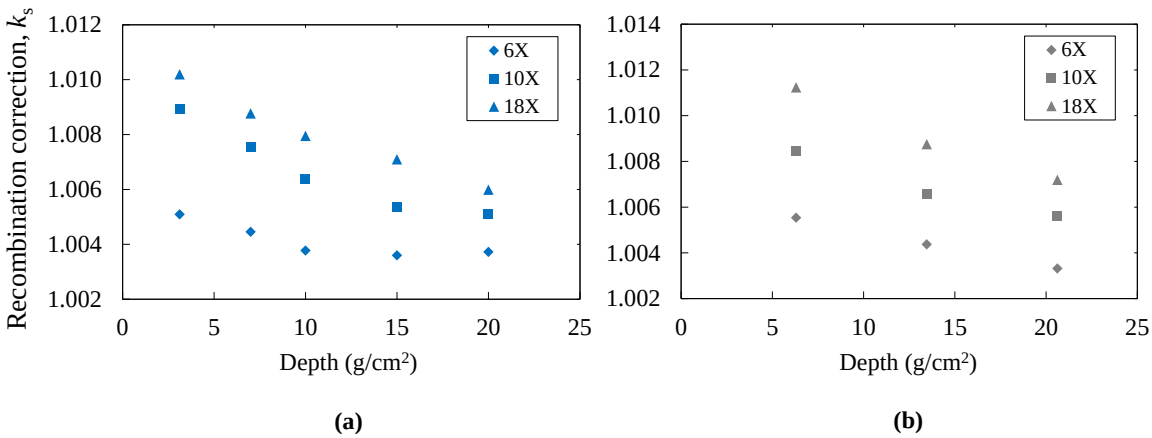

Figure 3-7: Recombination as a function of depth for (a) a CC13 chamber in a water phantom and (b) an NE 2571 chamber in a graphite phantom.

were fitted to the data for each phantom material and a calculated correction was applied to the measured PDIs before comparison with the modelled distributions.

Water temperature and pressure

The default density of water in the generation of pegs4 data is 1 g/cm^3, which is the density of water at 0°C. The temperature of the linac laboratory lies within the range 22-23°C and calibrations are corrected to a standard temperature of 20°C. The water material used in the water phantom model and calculation of absorbed dose to water was created with a density of 0.99821 g/cm^3 for water at 20°C. An uncertainty of 4°C was assigned in the uncertainty budget to cover the range up to 24°C.

Over the range of pressures from 100 kPa to 1000 kPa water density only varies by 0.04% (Lide, 2009). In the range of operating laboratory air pressures the variation in water density is insignificant and the pegs4 data were produced with the default pressure.

3.3.4 Optimisation method

The quality of the match between the modelled distributions and the measured data were assessed based on the local differences of the normalised data sets. PDDs are particularly important when determining the accuracy of the beam energy and spectrum. The differences between measured and modelled PDDs (relative to the measured PDD) were plotted against depth and the gradient determined (shown in Figures 3-3 and 3-6). This gradient will be referred to as the ‘difference gradient’, which for the purposes of the

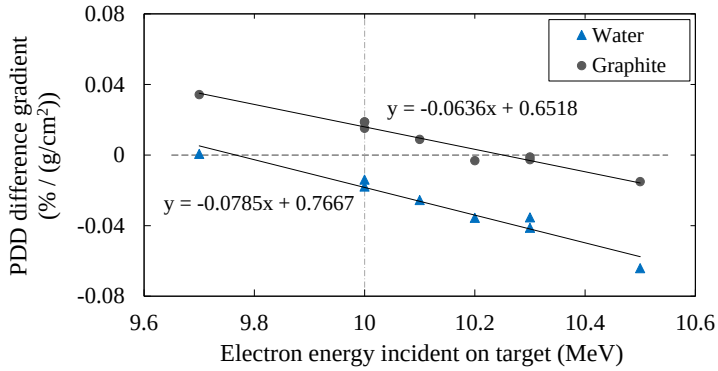

Figure 3-8: Difference gradients in water and graphite phantoms for multiple incident electron energies for the nominal 10 MV beam. The depth in the graphite phantom has been scaled to the water-equivalent depth. The darker dashed line shows the ideal gradient of zero. The electron energy has been selected to minimise the deviation from the dashed line for both materials.

uncertainty analysis has units of '% per cm', and is discussed further in Section 5.1.3. For two perfectly matched PDDs, the difference gradient would be zero.

As part of the model optimisation, the incident electron energy was adjusted based on the difference gradients in both materials. A plot of difference gradients versus energy for the nominal 10 MV beam is shown in Figure 3-8, from which two observations can be made. Firstly there is a linear relationship between the difference gradient and electron energy. Secondly there is some separation between the plots for water and graphite. This should not be the case for an ideally-matched model. Inaccuracies in the Monte Carlo interaction coefficients could cause such separation. In order to compare the two materials in Figure 3-8 the difference gradients have been scaled by density, converting from the units of '% per cm' to '% per (g/cm^2)'. The optimum electron energy is found using a least squares analysis. Since the doses calculated in both media are of equal importance, the gradients for both media are weighted equally. The minimum sum of squared difference gradients occurs at an electron energy of 10.0 MeV, shown by the lighter dash-dotted line. Despite the variation in difference gradients over the range shown, the variation in Monte Carlo dose conversion factor (described in Chapter 4) is less than the statistical uncertainty in the calculation of doses in the two media.

Once the validated models of the linac beam qualities are complete they can be used repeatedly for calculations of point doses or dose distributions in the linac beam. There are two points worth noting before we proceed to the next stage of calculations. Firstly, there is no dose scored in the linac head itself (for example, in the monitor chamber). This is not a problem, but it means the model can only be used to model relative doses or dose ratios. A dose ratio is the specific purpose of this project so the inability to calculate absolute dose is of little consequence. Secondly, it is recognised that validating linac models for most

applications by modelling two field sizes would be insufficient. For the application of primary standards, however, the 10×10 cm^2 field is the reference field used for the majority of work and the accurate modelling of the reference field is more important than modelling a range of field sizes. The extension of the linac model to a wider range of field sizes, in particular small fields defined by both the multi-leaf collimator and cones, is beyond the scope of this work.

CHAPTER 4 CONVERSION FROM DOSE TO GRAPHITE TO DOSE TO WATER

A calibration for absorbed dose to water by ARPANSA begins with a measurement of absorbed dose to graphite. A graphite calorimeter is used to measure the heat rise caused by irradiation and the absorbed dose to graphite is determined. The measured dose to graphite is converted to absorbed dose to water using a factor evaluated by Monte Carlo calculations. The derived absorbed dose to water is then used to determine the calibration factors of transfer and client ionisation chambers.

This chapter is devoted to explaining the methodology in the determination of absorbed dose to water at ARPANSA. The text that follows includes a detailed discussion of the techniques of graphite calorimetry, the modelling of the calorimeter and water phantom and validation of both models. Finally, previous methods of converting dose to graphite to dose to water are considered for the purposes of comparison with the new Monte Carlo method.

The key parameters in the calorimetry measurement are the mass of graphite, the change in temperature as determined by the change in thermistor resistance and the irradiation time. The dose rate in the linac beam is assessed using the calorimeter operated in both the quasi-adiabatic and quasi-isothermal modes. The agreement between the two independent methods provides validation of the method. The quasi-isothermal mode is selected as the primary means to determine the dose rate of the beam because it is less sensitive to uncertainties in the calorimeter calibration factors.

All the graphite calorimetry work at ARPANSA is performed by my colleagues and has been described in detail in a technical report (Ramanathan *et al.*, 2014). Details of the method have been included in Section 4.1 to show an understanding of the entire process and to complete the picture for the reader.

4.1 Measurement of absorbed dose to graphite

The basic principle of calorimetry for radiation measurements is that the increase in temperature due to radiation interactions is directly related to the amount of energy

deposited in the calorimeter. The temperature increase can thus be used to determine the absorbed dose in the calorimeter material. There are three common modes of operation of graphite calorimeters to determine the heat rise: quasi-adiabatic, iso-thermal (constant temperature) and quasi-isothermal (constant temperature rise) modes (Seuntjens and Duane, 2009; Witzani *et al.*, 1984). At ARPANSA the principal method employs the quasi-isothermal mode and the quasi-adiabatic mode is used as a validation.

In adiabatic mode the temperature rise of the core in response to an irradiation is measured. The specific heat capacity (or a recent calibration of the temperature rise of the core in response to different electrical heating powers) is used to convert the radiation induced temperature rise into power. For this to be valid, heat lost from the calorimeter must be the same during the calibration and radiation phases of the measurement. This can lead to increased uncertainty if the heat loss is not well matched. The two other modes, quasi-isothermal and quasi-adiabatic, are not susceptible to this problem and are the most common modes of operation at ARPANSA. In quasi-isothermal mode the rate of heating caused by irradiation is reproduced by electrical heating and the energy deposited is equated to the electrical power. In quasi-adiabatic mode no electrical heating is employed during the measurement. The temperature of the core is measured continuously and the heating caused by irradiation is equated to the energy deposited by applying an electrical calibration (Ramanathan *et al.*, 2014).

4.1.1 Quasi-adiabatic mode of operation

In quasi-adiabatic mode the temperature of the core is measured by one or more thermistors before, during and after irradiation. Linear fits are applied to the pre-irradiation and post-irradiation drift temperature data and both are extrapolated to the middle of the irradiation period. The difference between the extrapolated fits at the mid-point of the irradiation is used to determine the voltage difference or temperature rise. This is shown in Figure 4-1.

The specific heat capacity of the core can be measured and used to convert the rise in temperature to the absorbed dose to the core (D_c) according to Equation 4-1. The specific heat capacity of the core ($c_{m,core}$) has units of $J.kg^{-1}.K^{-1}$ and the rise in temperature (ΔT, units of K) is evaluated by thermistor calibration which converts the measured resistance to temperature.

$$D_c = c_{m,core} \Delta T_c \tag{4-1}$$

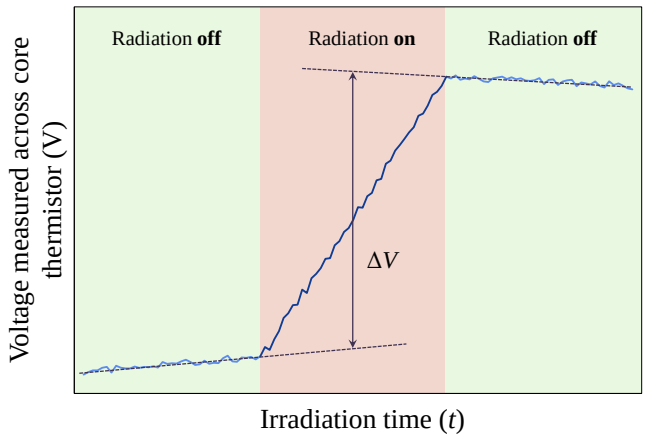

Figure 4-1: Artificial sample data collection from a quasi-adiabatic measurement run. The temperature rise (ΔT) is determined using the thermistor calibration. The difference between the pre-irradiation and post-irradiation drifts is measured at the midpoint of the irradiation.

It is difficult to measure the specific heat capacity of the core in the ARPANSA calorimeter because it cannot be completely isolated from the surrounding graphite bodies. Instead, an electrical calibration is used where heating thermistors dissipate a known quantity of energy in the core and the change in voltage across the core thermistor is measured. The electrical calibration requires two calibration factors: the DVM calibration factor (C_{DVM}) and the electrical calibration factor (C_{ECF}). The DVM calibration factor converts the voltage drop across the core thermistor to the change in core thermistor resistance and the electrical calibration factor relates the change in resistance to the heating energy dissipated in the core. The core is calibrated in terms of electrical heating according to the following equation:

$$D_{\mathrm{c}} = \frac{\left(\Delta V \cdot C_{\mathrm{DVM}} \cdot C_{\mathrm{ECF}}\right)}{m_{\mathrm{c}}} \cdot \prod k_i \tag{4-2}$$

where ΔV is the measured change in voltage between due to irradiation, m_{c} is the mass of the core and Πk_i are the various corrections required (Ramanathan *et al.*, 2014). The corrections are described in more detail in Section 4.1.4.

4.1.2 Quasi-isothermal mode of operation

'Isothermal' generally describes a system or process with a constant temperature. In quasi-isothermal mode rather than keeping the calorimeter temperature constant, the rate of temperature increase is kept as constant as possible. To do this, the core is heated electrically before and after irradiation. The heating rate due to irradiation is predicted or

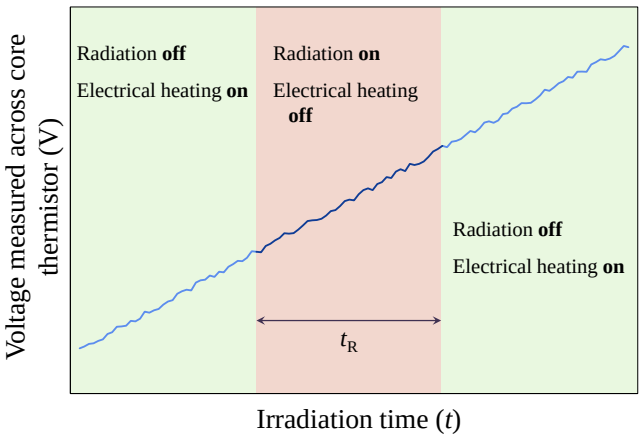

Figure 4-2: Artificial sample data collection from a quasi-isothermal measurement run. In this illustration the electrical heating rate (shown in the green sections) matches the rate of heating during irradiation (central red section).

determined by preliminary irradiations and the electrical heating is closely matched to that of the irradiation. This is shown in Figure 4-2. Since the heating rates are matched, the energy deposited in the core during irradiation can be determined from the electrical heating applied.

As with the quasi-adiabatic mode and electrical calibration, the quasi-isothermal mode does not rely on the specific heat capacity of the core. The absorbed dose to the core is calculated using the power dissipated in the core (P_e), the duration of the irradiation (t_R), the mass of the core and the product of corrections (described in Section 4.1.4) according to Equation 4-3.

$$D_c = \frac{(P_e \cdot t_R)}{m_c} \cdot \prod k_i \tag{4-3}$$

4.1.3 ARPANSA calorimeter description

The ARPANSA calorimeter is a Domen-type design (Domen and Lamperti, 1974) with a core 2.0 cm in diameter and a thickness of 2.75 mm. The core is insulated by layers of graphite separated by evacuated gaps. Each graphite surface (except the core) is coated with an aluminised Mylar sheet. The combination of Mylar and vacuum gaps ensures good thermal and electrical isolation.

The jacket immediately surrounds the core, followed by the shield. The medium is the outermost layer with a thicker aluminised Mylar coating on the outer front surface. The

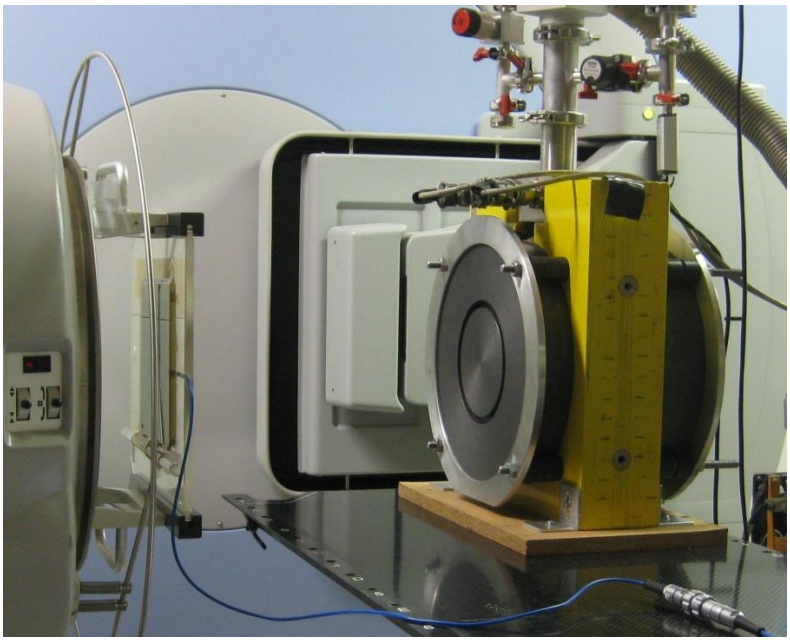

(a)

(b)

(c)

Figure 4-3: Photos of the complete assembled calorimeter with front plates attached on the linac table (a) and the inner part of the calorimeter separated from the outer bodies (b). The vacuum pump that evacuates the calorimeter attaches at the top of the device. The graphite phantom the calorimeter sits within is shown in (c) and the screw threads that hold the build-up and backscatter plates in place can be seen.

core has two sensing thermistors and one heating thermistor attached at the edges of the disc. The jacket and shield both have one heating and one sensing thermistor. Further details of the design are available in a report by Ramanathan *et al.* (2014). Additional graphite plates are attached to the front of the calorimeter so that a depth of approximately 10 g/cm^2 is achieved to match the reference depth in water. Photos of the calorimeter can be seen in Figure 4-3 and a schematic of the entire calorimeter, including additional plates, is shown in Figure 4-4.

4.1.4 Corrections for the ARPANSA calorimeter

Several corrections need to be made to a calorimetry measurement so it can be used to calculate dose at the reference depth and distance in water. The product of all required corrections is denoted Πk_i and is applied as described in Equations 4-2 and 4-3. The corrections required are described in Table 4-1.

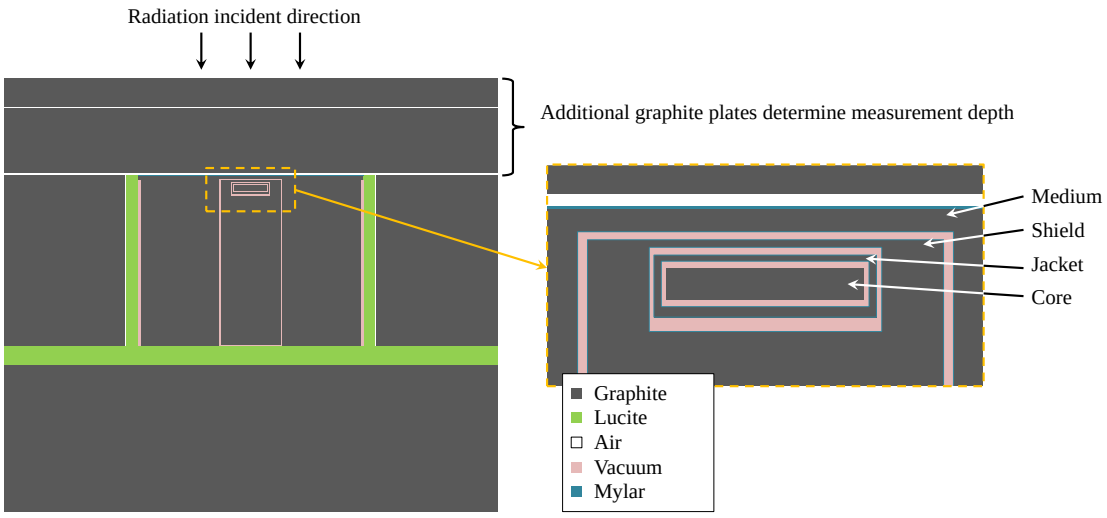

Figure 4-4: Detailed schematic of the calorimeter model. The key internal components surrounding the core have been enlarged and labelled to the right of the figure.

In practice, in the method adopted by ARPANSA the absorbed dose to water is calculated at the correct reference depth and distance and the calorimeter gaps are included in the model. Hence, no further corrections are required for k_d, k_z and k_{gap}. The linac beam is axially symmetric over the small thickness of the core so k_{an} is equal to 1.000. The radial non-uniformity corrections were calculated by a radial integration using measured profiles in the in-line and cross-line directions. Over the radius of the calorimeter core the k_{rn} corrections were 1.0000, 0.9948 and 1.0006 for the 6 MV, 10 MV and 18 MV beams respectively.

In addition to the corrections applied to the calorimeter measurement, the measured core mass requires corrections for buoyancy and non-graphite materials in or attached to the

Table 4-1: Corrections applied to the ARPANSA calorimeter measurements in the determination of absorbed dose to water.

Correction	Purpose
Distance correction (k_d)	Corrects for deviation from the reference distance of 1100 mm by inverse square law.
Depth correction (k_z)	Corrects for deviation from the reference depth of 10 g/cm^2 where the graphite plates could not exactly match the reference depth. The correction is calculated using empirical attenuation data.
Gap correction (k_{gap})	Corrects for perturbations in the photon fluence caused by vacuum gaps and non-graphite materials around the calorimeter core.
Axial non-uniformity correction (k_{an})	Corrects for the axial (z direction) non-uniformity of the linac beam.
Radial non-uniformity correction ($k_{rn,core}$)	Corrects for the radial non-uniformity of the linac beam.

core (thermistors and wires, epoxy and polystyrene mounts). These corrections are described further in the report by Ramanathan *et al.* (2014).

4.2 Modelling the calorimeter

A gap correction is required by a primary standards laboratory when the calculated graphite dose is obtained by modelling a homogenous graphite phantom. The gap correction is used to correct the measured core dose for perturbations caused by air and vacuum gaps in the calorimeter and obtain the dose in a homogenous graphite phantom. At ARPANSA we elected to forgo the use of gap corrections. Rather, we modelled the complete calorimeter using the FLATFILT component module. Air gaps between the added plates and vacuum gaps and insulating Mylar layers within the calorimeter were explicitly included in the model. The internal dimensions of the calorimeter were obtained from detailed design drawings and notes written during construction and were confirmed by imaging as described in Section 4.3.1. The dimensions and densities of the attached plates were obtained from physical measurements. The Monte Carlo transport parameters were the same as those used for the linac model.

4.3 Validation of calorimeter model

The calorimeter geometry can be considered in two parts: the actual calorimeter and the additional plates added to the front and back of the calorimeter for build-up and backscatter. The effect of small changes to the thickness of the sections behind the core were investigated as part of this work and were found to have no discernible influence on the dose scored in the core. The thicknesses of the build-up plates and calorimeter layers in front of the core, however, are of critical importance in the modelling of the dose to the core.

The build-up plates have been measured and weighed to determine their dimensions and density. Many of the plates varied in thickness between the centre of the plate and the edge due to the method of production. The central thickness was used in the model, and gaps between the plates calculated by the outer dimensions. Although the dimensions of the individual plates are well characterised, kilovoltage imaging was used to confirm the plate gaps when the calorimeter was assembled as the actual gaps depend on uniformity of the plate surface and tensioning of the clamped assembly.

The calorimeter itself cannot be disassembled for inspection so the original dimensions were based entirely on documentation produced during assembly of the calorimeter. As with the plate gaps, radiographs were used to measure the thicknesses of the internal layers and gaps within the calorimeter. In addition to the imaging, gap corrections were calculated and compared to values in the literature for similar calorimeters as an additional 'sanity check'.

4.3.1 Imaging the calorimeter

Figure 4-5 shows the experimental setup for imaging the calorimeter. The focus-to-surface distance (FSD) was made as large as possible to minimise distortion due to beam divergence through the thickness of the calorimeter and from the calorimeter to the digital radiography detector. The calorimeter including buildup and backscatter plates was clamped in the usual arrangement with an additional plate at the front to prevent the clamps obscuring the front plate edge. The focus-to-surface distance used was approximately 2 m and the calorimeter was suspended on a thin board approximately 1 cm above the detector. The detector used was a Carestream DRX-1. The field size was reduced to minimise the area of the detector in the direct beam. A small area at the front of the calorimeter was unavoidably exposed, and this was covered with lead sheet. The internal dimensions of the calorimeter were imaged using beam settings of 140 kV and 142 mAs. The distances between the plates could not be measured with these settings, however, because direct transmission and detector saturation cause broadening of the apparent gap. The front plates were imaged using beam setting of 140 kV and 126 mAs with an additional steel filter approximately 2 mm thick covering the gaps between the plates.

The images were saved in DICOM format and processed with ImageJ image processing software. Images were rotated so that the central axis was horizontal and an average profile collected using the rectangular selection tool over the largest possible area, avoiding interference from artefacts or internal components such as screws. The profile data consisting of position versus pixel intensity were exported to Microsoft Excel. The natural log of the pixel intensity values were plotted to reveal local maxima relating to areas of graphite and minima relating to air or vacuum gaps as shown in Figure 4-6. The TREND function was used to find the position of the mid-point between each minimum and adjacent maximum and the distances between the mid-points determined the thicknesses of the layers. In some images there was a distinct gradient in the pixel intensity values. In these images the gradient was calculated and removed from the data prior to the mid-points

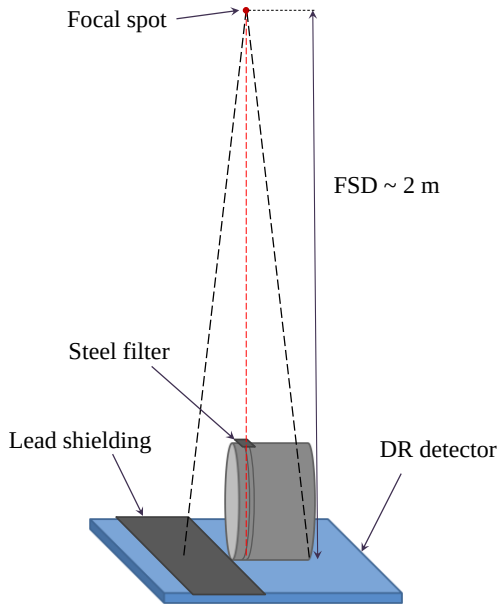

Figure 4-5: Setup for kilovoltage imaging of calorimeter. The central beam axis (depicted by the red dotted line) was aligned with the areas of interest. Lead shielding was used to protect the detector from the direct beam. A steel filter was placed over the gaps between the plates to prevent detector saturation by direct transmission of the beam. The beam width is shown by the dark dotted lines.

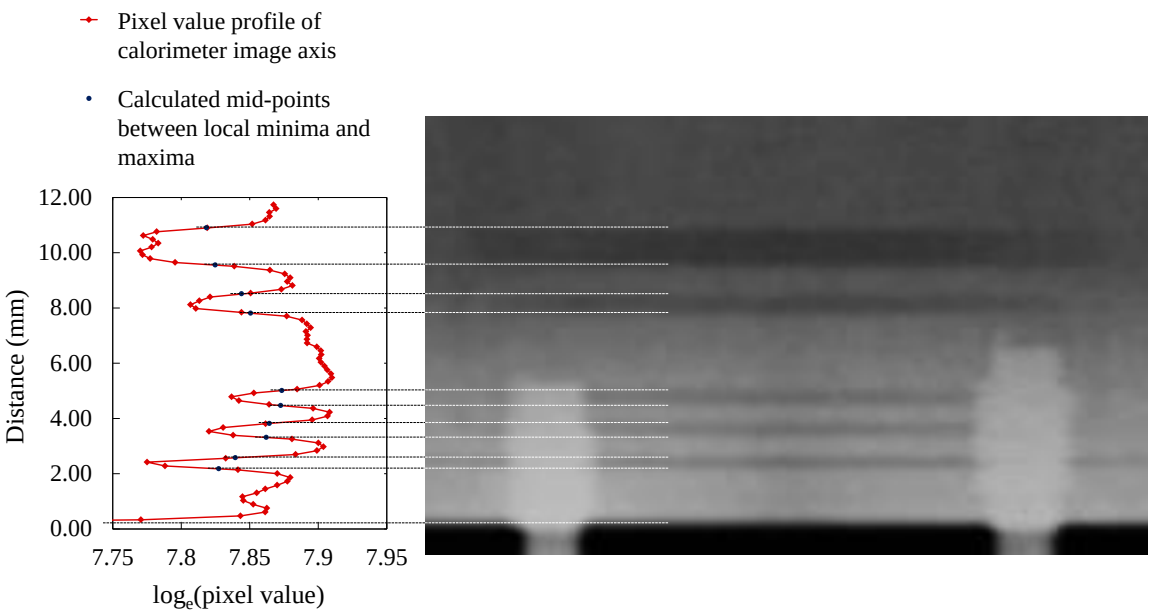

Figure 4-6: Sample pixel value data for a slice along the axis of a calorimeter image. The actual data are shown in red and the calculated mid-points between each local minimum and maximum shown in black. A corresponding image is shown to the right of the plot.

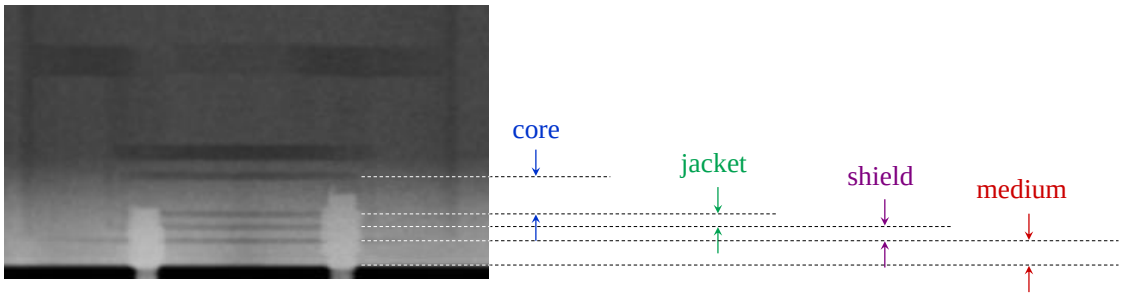

Figure 4-7: Radiograph of the calorimeter without front plates attached. The separation between the core, jacket, shield and medium can be clearly identified.

being determined. Figure 4-6 shows a sample of the data output and calculated mid-points with a corresponding image.

The radii of the internal layers in the calorimeter are small compared to the outer radius and the edges between the internal parts could be seen quite clearly. From the original set of images, the thicknesses were measured of all components from the front of the calorimeter (without plates attached) to beyond the core. The gaps between the plates, with radii the same as the outer radius of the calorimeter, were distorted at distances more than a few millimetres from the beam central axis due to the expanding beam. For this reason, it was not possible to clearly see the edge of more than one plate in a single image. Sample radiographs are shown of the internal calorimeter layers in Figure 4-7 and of the calorimeter with front plates attached in Figure 4-8. The front of the first plate was aligned with the beam central axis and the distance between the first plate and the rear of the core measured along the centre of the cylindrical geometry. Taking into account the measured thicknesses of the internal parts of the calorimeter, the measured central thickness of each plate and the expected gaps between the plates from the measured outer thickness, the extra distance measured was divided evenly between the three plate gaps and added to the expected gap thickness. The original and corrected dimensions are listed in Table 4-2.

Efforts to scale the distances to an external reference (for example a micrometer) had limited success and did not produce reliable results. During production of the calorimeter, careful measurements of the core dimensions were performed and results recorded. The mass of the core is critical in the calculation of the dose deposited during irradiation so the dimensions of the core are well documented. The thickness of the core was selected as the reference distance from which to scale the rest of the dimensions.

Another important consideration is distortion of the image across the field due to beam expansion. Although this should be minimal with the focus-to-surface distance used, it was

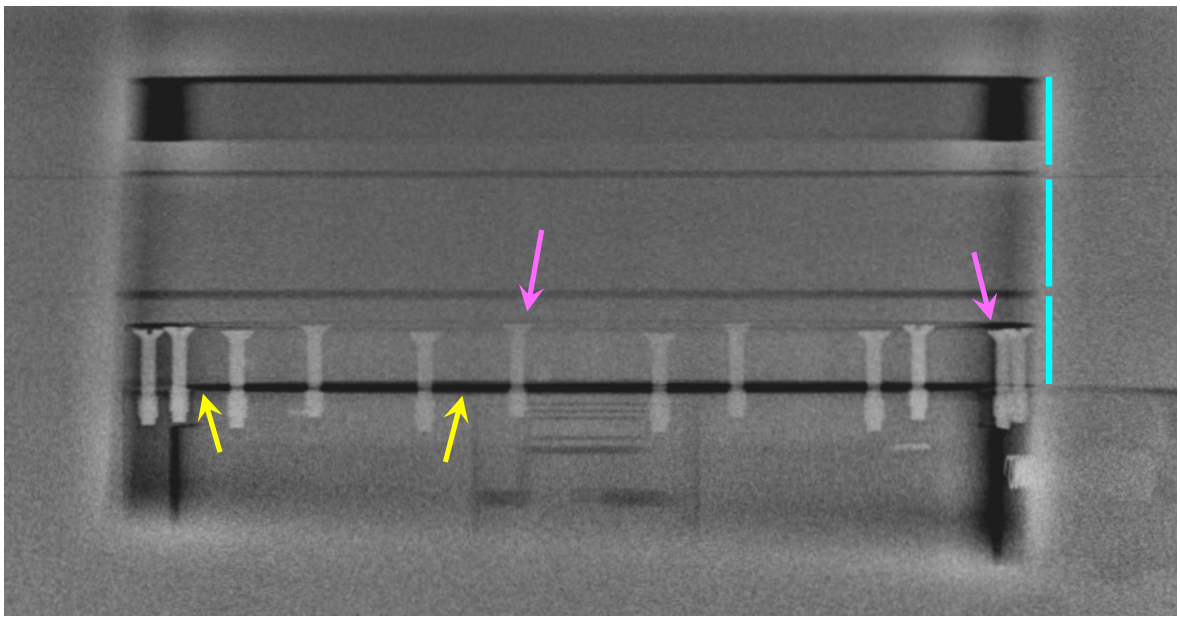

Figure 4-8: Radiograph of the calorimeter with the front plates (indicated by blue lines) attached. The distortion in the definition of plate gaps away from the focal plane can be seen particularly in the gap closest to the calorimeter (yellow arrows) and the screws around the edge (pink arrows). The beam expansion through the thickness of the calorimeter causes widening of the gap in the centre of the image where the front and rear surfaces are furthest apart.

Table 4-2: Original and corrected thicknesses of each layer in the calorimeter model.

Calorimeter part	Original thickness (mm)	Corrected thickness (mm)	Difference (mm)
Plate C15	15.31	15.31	
Gap1	0.00	0.50	0.50
Plate C20	19.815	19.815	
Gap2	0.18	0.68	0.50
Plate P15	14.86	14.86	
Gap3	0.60	1.10	0.50
Mylar	0.138	0.138	
Medium	2.00	2.00	
Gap	0.65	0.65	
Shield	0.744	0.744	
Gap	0.65	0.65	
Jacket	0.546	0.546	
Gap	0.55	0.55	
Core	2.75	2.75	
Gap	0.55	0.70	0.15
Jacket	0.546	1.00	0.454
Gap	0.65	1.30	0.65

checked by imaging a metal ruler with grooves at 1 cm intervals. The ruler was imaged in the position of the calorimeter with the scale markers covering the relevant area of the field in both the *x* and *y* directions. The distances between the grooves were measured using the same method as the calorimeter measurements with a resolution of 0.14 mm. No distortion was observed in either direction.

4.3.2 Calculation of gap corrections

Gap corrections were calculated by removing all air, vacuum and Mylar from the calorimeter model and calculating the dose to the calorimeter core. All graphite pieces were collapsed toward the core, keeping the core in the same position as the original calorimeter model. The correction is calculated as the ratio of the dose without gaps to the dose with gaps. For the ARPANSA beams the modelled gap corrections are 1.009(2) for the 6 MV beam ($TPR_{20,10}$ = 0.673), 1.006(1) for the 10 MV beam ($TPR_{20,10}$ = 0.734) and 1.004(1) for the 18 MV beam ($TPR_{20,10}$ = 0.777). Quantities in brackets are the relative standard uncertainty (k = 1) for each correction. These values are comparable with those reported by Pearce *et al.* (2011) who found gap corrections in the range of 1.006 to 1.002 for beams with $TPR_{20,10}$ from 0.633 to 0.800 for a calorimeter of similar type to that used at ARPANSA.

4.4 Modelling the water phantom

The reference conditions for calibration in a megavoltage beam are a 100 cm source to phantom surface distance and a depth of 10 g/cm^2 in water. These conditions are consistent with the TRS-398 protocol (Andreo *et al.*, 2000). The water phantom is irradiated from the side and the beam passes through a 0.24 cm polycarbonate window. The window thickness is converted to an equivalent water thickness of 0.29 cm using a polycarbonate density of 1.2 g/cm^3. Taking this into account, the ionisation chamber is positioned at a depth of 9.95 cm from the external window surface which equates to 10 g/cm^2.

The water phantom was modelled using a combination of SLABS and BLOCK component modules. The front window and water in front of and behind the scoring volume were modelled using SLABS. The BLOCK component module was used to model the scoring volume because it allowed a cylindrical scoring volume set within a rectangular water phantom. The shape and dimensions of the scoring volume were selected to approximate

those of the calorimeter core. Dose scoring in the water phantom is considered further in Section 4.6.

4.5 Validation of water phantom model

The water phantom is a relatively simple geometry to replicate so there is little validation required for the physical geometry. With water temperature taken into account as explained in Section 3.3.3, the only remaining concerns were the use of the BLOCK component module and the equivalence of doses calculated using different component modules and user codes. In the early simulations, the water phantom was modelled using the FLATFILT component module so that the dimensions of the scoring volume could be matched exactly to that of the calorimeter core. However, FLATFILT has a completely radial geometry which does not match the rectangular water tank used experimentally. A simple solution would be to create a water phantom in DOSXYZnrc, however the scoring zone would be rectangular and would not match the cylindrical shape of the calorimeter core.

The BLOCK component module offers a rectangular geometry with user-defined shape inside. The scoring volume was defined by 16 points evenly spaced around the circumference of a cylinder to approximate the cross section of the graphite core. The BLOCK component module places a mandatory 0.1 mm air gap in front of the scoring layer. Air gaps can affect the build-up of electrons and affect the dose deposited directly adjacent to the gap. A staged approach was taken to investigate the effect of the air gap on the calculated dose. The transition between a rectangular water phantom with a cylindrical scoring volume and a solid rectangular block of water (only possible in DOSXYZnrc) requires three changes: removal of gaps, a change in user code and a change in scoring volume shape. Changing the shape of the scoring volume should not affect the dose deposited provided the scoring areas are the same. A larger area than the core was chosen to improve the efficiency of the calculation. Rectangular scoring volumes were defined with a half width of 2.00 cm and cylindrical volumes with a radius of 1.128 cm. All scoring volumes had a depth of 2.75 mm.

BEAMnrc and DOSXYZnrc are both built on the same EGSnrc code so doses calculated in both programs should be equivalent. However, there is the possibility of modifying settings within the codes independently. In order to identify the cause of differences between calculated doses, should differences be found, multiple simulations were performed with only a single change made between any two geometries. The simulation steps are shown in

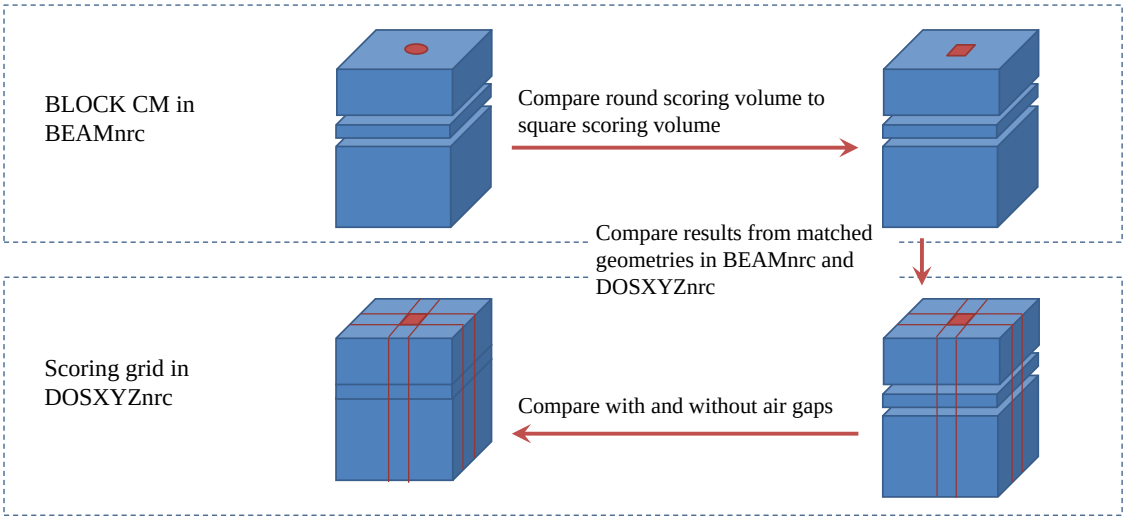

Figure 4-9: This figure shows the staged approach to assessing influences on the dose calculated in an equivalent-sized volume using different user codes and the effect of gaps around the scoring volume. The red shapes at the top of each block of water depict the area of the scoring volume. In each simulation, the dose was assessed in the middle layer of the phantom, shown by either gaps or heavy blue lines. The red lines in the DOSXYZnrc section show the vertical voxel boundaries.

Figure 4-9. No effect on the absorbed dose could be observed above the 0.1% statistical uncertainty level between any of the simulation steps.

4.6 Converting from graphite dose to absorbed dose to water using Monte Carlo

Absorbed dose to graphite (D_g) at a point is obtained by applying the radial non-uniformity correction to the graphite dose measured by the calorimeter as explained in Section 4.1. The absorbed dose to graphite is converted to absorbed dose to water (D_w) at the reference depth using BEAMnrc. In the calorimeter model, dose was scored in a single scoring volume that encompassed the entire graphite core. This corresponds directly to the measurement of absorbed dose in the calorimeter where the average energy absorbed by the core is measured.

In the water phantom, dose was scored in an approximately cylindrical volume with a 1.00 cm radius and a depth of 2.75 mm. The scoring volume was approximately equal to the scoring volume within the calorimeter model. Matching the cross sectional areas of the two scoring volumes eliminates the need to apply corrections for radial non-uniformity between the two calculations. The scoring voxel was centred at the reference depth used for ionisation chamber calibrations. When combined with the measured graphite point dose, the calculated conversion factor provides the absorbed dose to water at a point at the

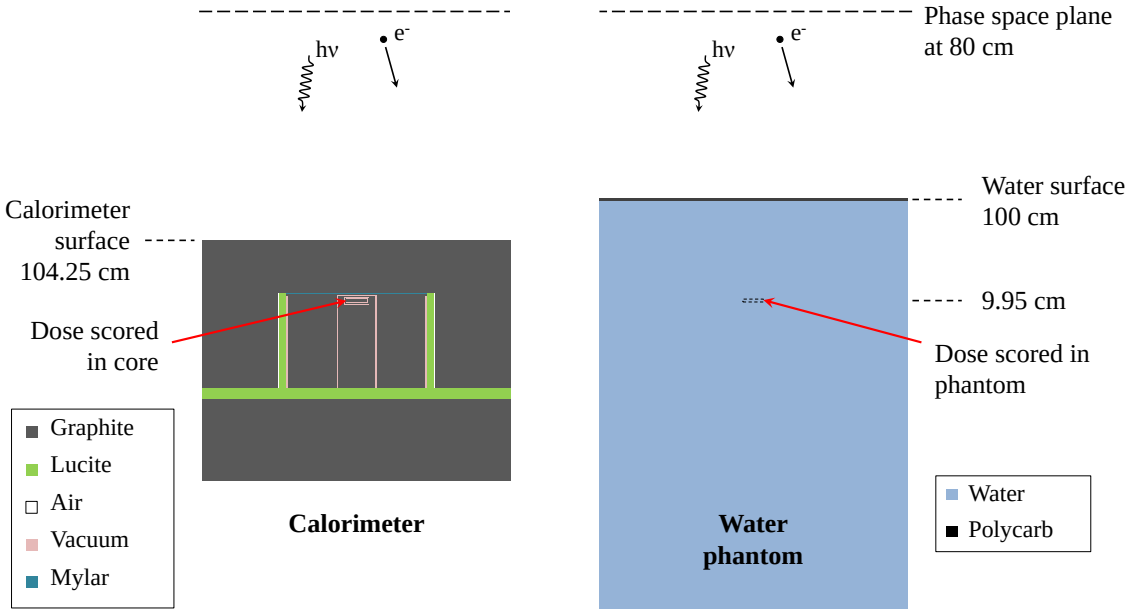

Figure 4-10: Schematic of the calorimeter and water phantom models used to obtain the $[D_w/D_g]_{MC}$ conversion ratio. The figure shows the models side by side to show that the positions of dose scoring are at the same distance from the source. The details of the calorimeter model can be seen in Figure 4-4.

reference depth. Calibrating an ionisation chamber then requires a non-uniformity correction to correct the measured dose to water (averaged over the chamber dimensions) to a point dose at the reference depth.

For both the calorimeter and water phantom models, the phase space files scored at 80 cm were used as the input source. The geometry of both models is shown in Figure 4-10. The ratio of the absorbed dose in the calorimeter graphite core to absorbed dose to water at the reference position becomes the conversion factor, and is denoted by $[D_w/D_g]_{MC}$. Doses derived by Monte Carlo calculation are denoted by the letters 'MC' in the subscript to distinguish them from measured quantities. The calculated conversion factors for the 6 MV, 10 MV and 18 MV beams are listed in Table 4-3 along with the measured $TPR_{20,10}$ beam qualities. The standard uncertainty in Type A uncertainties (statistically-based

Table 4-3: Monte Carlo conversion ratios for the three beam qualities available on the ARPANSA linac. The ESDM is reduced by running the simulation with a large number of histories to ensure confidence in the conversion ratio.

Beam quality	6 MV	10 MV	18 MV
$TPR_{20,10}$	0.674	0.734	0.777
$[D_w/D_g]_{MC}$	0.9616	0.9404	0.9252
ESDM (%)	0.09	0.11	0.12

uncertainties where the uncertainty is reduced by increasing the sample size) is the estimated standard deviation of the mean (ESDM). The ESDM is calculated as $\sigma/\sqrt{n}$ (ISO/IEC, 2008).

4.7 Converting from graphite dose to absorbed dose to water using cavity ionisation theory

A rigorous method of validating the calculation of absorbed dose to water is to compare a second, independent method of converting from absorbed dose to graphite. Earlier standards for absorbed dose to water in ^{60}Co radiation used either the photon fluence scaling theorem or the cavity ionisation theory to achieve dose to water (Wise, 2001). The photon fluence scaling theorem relies on accurate knowledge of the position of the radiation source and assumes that Compton scattering is the only type of interaction in the phantoms. These conditions make this method less suitable for linac megavoltage energies. The cavity ionisation theory is suitable for megavoltage energies and appropriate for comparison.

The cavity ionisation method was explained in some detail in Section 2.5. In short, the method involved calibrating an ionisation chamber for dose to graphite in a graphite phantom, and then converting the calibration for absorbed dose to water analytically. The equation used at ARPANSA is shown below (Equation 4-4). It is the same as Equation 2.4 from Chapter 2, except that $\dot{D}_w/I_w$ is replaced with $N_{D,w,CIT}$ since the validation method does not require a measurement in water. $N_{D,w,CIT}$ is the calibration coefficient determined by the cavity ionisation method. The remaining variables are the same as those defined earlier. The method is shown schematically in Figure 4-11.

$$N_{D,w,CIT} = \frac{\dot{D}_g}{I_g} \frac{\bar{s}_{w,a}}{\bar{s}_{g,a}} \cdot \frac{[p_{wall}\, p_{dis}\, p_{cel}]}{[p_{wall}\, p_{dis}\, p_{cel}]''} \tag{4-4}$$

The values of mean restricted stopping power ratios were interpolated from the graphite/air and water/air Spencer-Attix stopping power ratios in Table 4 of Andreo and Brahme (1986). The displacement correction factors were calculated for each chamber by Equations 4-5 and 4-6 (Wise, 2001) which are based on Johansson *et al.* (1978). The displacement factor, *k*, is interpolated from the values provided by Johansson *et al.* (1978), however the interpolation is only approximate since accelerating potential is the only beam

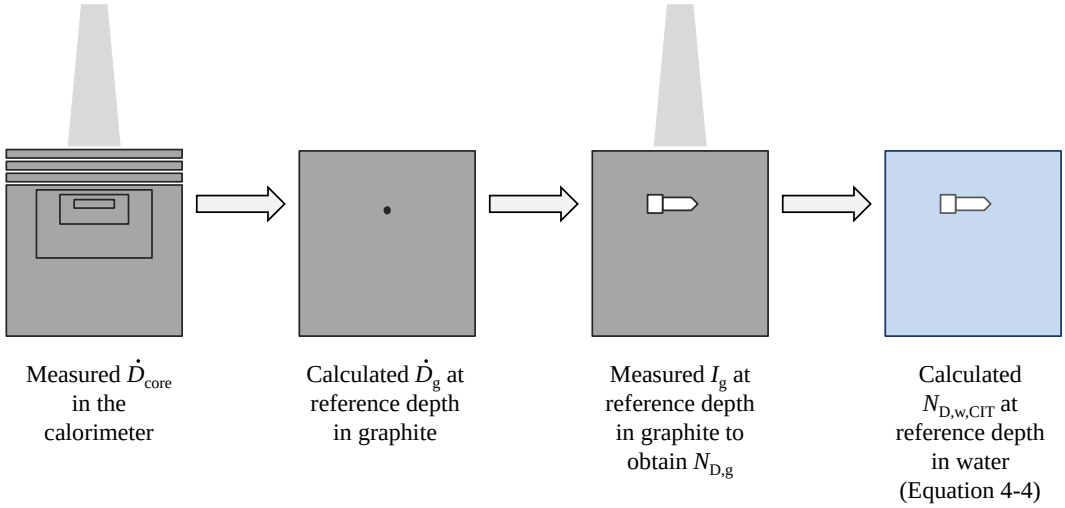

Figure 4-11: The steps of the cavity ionisation method. Details of the corrections required at each step are available in the report by Ramanathan *et al.* (2014).

quality provided in the original reference. $\rho^{e}_{g,w}$ is the ratio of electron densities in graphite and water and r is the internal radius of the chamber cavity.

$$p_{dis} = 1 - kr \tag{4-5}$$

$$p''_{dis} = 1 - k\rho^{e}_{g,w} r \tag{4-6}$$

For the NE 2611A chamber, the p_{wall} corrections were interpolated from the values calculated by Wise (2001) which include a waterproof sleeve. For the NE 2571 the p_{wall} corrections were interpolated from corrections for the NE 2571 with sleeve calculated by Wulff *et al.* (2008) using Monte Carlo methods. The values of each of the corrections are

Table 4-4: Cavity ionisation method parameters and resulting ratio between the calibration coefficients derived by cavity ionisation theory and the Monte Carlo method.

Chamber	**Beam quality**	p_{wall}	$\frac{p_{dis}}{p''_{dis}}$	$\frac{\bar{s}_{w,a}}{\bar{s}_{g,a}}$	$\left[N_{D,w,Q_{ARP}}\right]^{CIT}_{MC}$
NE 2571[a]	6 MV	1.0008	1.0080	1.1330	1.002
NE 2611A	6 MV	0.9933	1.0099	1.1330	1.001
NE 2571[a]	10 MV	1.0020	1.0057	1.1359	1.001
NE 2611A	10 MV	0.9961	1.0081	1.1359	1.001
NE 2571[a]	18 MV	1.0029	1.0048	1.1332	0.998
NE 2611A	18 MV	0.9995	1.0055	1.1332	1.001

[a] The results for an NE 2571 chamber are the average of the two chambers used.

listed in Table 4-4 with the results. For both graphite-walled chambers the p''_{wall} correction is unity, as is $\frac{p_{\mathrm{cel}}}{p''_{\mathrm{cel}}}$.

An NE 2611A and two NE 2571 ionisation chambers were calibrated for dose to graphite and the calibration coefficient in terms of dose to water calculated for each beam quality ($\left[N_{\mathrm{D,w},Q_{\mathrm{ARP}}}\right]_{\mathrm{CIT}}$) using cavity ionisation theory. The calibration coefficients for the same chambers calculated using the derived $[D_{\mathrm{w}}/D_{\mathrm{g}}]_{\mathrm{MC}}$ conversion ratio ($\left[N_{\mathrm{D,w},Q_{\mathrm{ARP}}}\right]_{\mathrm{MC}}$) by the direct MC method were compared to the $\left[N_{\mathrm{D,w},Q_{\mathrm{ARP}}}\right]_{\mathrm{CIT}}$ values for each beam quality. The ratios of calibration coefficients ($\left[N_{\mathrm{D,w},Q_{\mathrm{ARP}}}\right]_{\mathrm{MC}}^{\mathrm{CIT}}$) for the three chambers are also shown in Table 4-4. The results of the cavity ionisation method to convert the graphite dose to absorbed dose to water are in excellent agreement with the direct Monte Carlo method, providing confidence in the validity of the Monte Carlo conversion method.

Using a range of validation methods provides confidence in the various elements of the method and in the overall result. However, the most rigorous way to test a new method is to undertake comparisons with independent organisations. In the case of the determination of absorbed dose to water, formal and informal intercomparisons have been performed with other international primary standards laboratories to assess the accuracy of the ARPANSA measurement. The following chapter presents the results of all the intercomparisons performed and a complete analysis of the uncertainty budget for the method.

CHAPTER 5 UNCERTAINTY ANALYSIS AND INTERNATIONAL COMPARISONS

The preceding chapters have described the steps in the process to determine absorbed dose to water from the measured absorbed dose to graphite at ARPANSA. The resulting quantity of absorbed dose to water is used to determine the calibration coefficient, $N_{D,w}$, of an ionisation chamber. Validation of the method has been performed at each step.

A critical part of any scientific outcome is an analysis of the uncertainty in the result. In particular, comparisons require an uncertainty budget to determine the significance of the result. Although the direct Monte Carlo conversion method is conceptually straightforward, the Monte Carlo method and the underlying physics have inherent uncertainties. The extent of these uncertainties is not immediately obvious and must be assessed. In Section 5.1 a detailed assessment of the uncertainties in the Monte Carlo conversion factor is presented. The resulting uncertainty in the calibration of an ionisation chamber is presented in Section 5.2.

The final stage of method validation is to compare the ARPANSA determination of absorbed dose to water with values obtained by other researchers. The most fundamental comparison is with other primary standards laboratories, and the most accurate method is via a direct comparison where all participants measure the absorbed dose in the same linac beam. This is a costly and time-consuming exercise because primary standard equipment is generally not portable. The key comparison BIPM.RI(I)-K6 organised by the BIPM is a direct comparison (CCRI, 2014). Alternatively, in an indirect comparison the calibration coefficient of a transfer standard ionisation chamber is measured in similar beams in two independent primary standards laboratories and the results compared. This is much simpler than a direct comparison, but requires interpolation for differing beam qualities and results in a slightly higher uncertainty. Both types of comparisons have been performed for this work and each is described in Section 5.3.

In addition to the comparisons of absorbed dose to water, the energy correction factor, k_Q, is validated by comparing it against published calculated and measured values. The k_Q value is the ratio of calibration coefficients measured in a linac beam and in ^{60}Co. In Section 5.5 the measured k_Q values for commonly used ionisation chambers are compared

to the IAEA TRS-398 values (currently used in Australia) and the Monte Carlo calculated k_Q values used in the 2014 addendum to the American Association of Physicists in Medicine (AAPM) protocol.

5.1 Analysis of the uncertainty in the Monte Carlo conversion factor

The uncertainty in the Monte Carlo calculation of the dose conversion ratio, $[D_w/D_g]_{MC}$, can be broken down into five components:

- the uncertainty in the calorimeter geometry (Section 5.1.1);
- the uncertainty in the water phantom geometry (Section 5.1.2);
- the uncertainty in the Monte Carlo cross-sections (Section 5.1.3);
- the uncertainty in the Monte Carlo transport (Section 5.1.4), and
- the statistical uncertainty in the Monte Carlo calculations (Section 5.1.5).

The contribution from uncertainties in the geometry of the calorimeter (vacuum and air gaps, thicknesses and densities) is estimated using the sensitivity of the dose at the reference depth to changes in these quantities. The contribution from the Monte Carlo interaction cross-sections is the most difficult to quantify and an estimate of the uncertainty is found by considering the degree to which the modelled PDDs match the measurements. The accuracy of the spectrum produced by the linac model must also be considered, however the uncertainty analysis for the Monte Carlo calculation in both materials of interest is assumed to account for small errors in the linac spectrum. The accuracy of the transport algorithms in EGSnrc has been investigated by the code developers. Finally, statistical uncertainties are inherent in any Monte Carlo calculation.

Table 5-1 provides a summary of the total uncertainty in the Monte Carlo conversion ratio for all three beams. The individual uncertainty components are summed in quadrature to obtain the combined relative standard uncertainty in the dose conversion ratio. The coverage factor, k, specifies the confidence with which the uncertainty is given. A coverage factor of $k = 1$ gives a confidence level of 68%, or stated another way there is a 68% probability that the real value lies in the range 'calculated value - stated uncertainty to calculated value + stated uncertainty' (i.e. calculated value ± stated uncertainty). The uncertainties in this thesis are stated at the $k = 1$ confidence level.

The complete analysis for the 6 MV beam quality is described in detail in the following five sections. In some tables it is appropriate to show the data for the three energies modelled. Where this is not the case, the corresponding analyses for the 10 MV and 18 MV beams are given in Appendix C.

5.1.1 Uncertainties due to calorimeter geometry

The calorimeter consists of a core at a depth of approximately 5 mm of graphite, surrounded by layers of graphite that are separated by vacuum gaps. Three graphite plates are added to the front of the calorimeter, separated by small air gaps.

Uncertainties in the calorimeter geometry arise from uncertainties in the densities of the graphite pieces, the thicknesses of the gaps and the mass of the core. The density of the graphite plates is calculated using the measured mass and volume (determined by measuring the dimensions of the plates). Since the plate thickness is used to determine the density, the uncertainty in thickness is inherent in the density uncertainty. Each of the contributions for a 6 MV beam are listed in Table 5-2. The density of the build-up plates has a smaller uncertainty than that of the calorimeter body due to the ability to inspect and measure the external plates. (The larger contribution to the total uncertainty is simply because the plate thickness is an order of magnitude greater than that of the total calorimeter thickness.) The large uncertainty applied to the calorimeter body is estimated by the range of quoted densities of graphite pieces obtained from the calorimeter manufacturer.

For each uncertainty contribution, Table 5-2 shows the value (for example, the plate density of 1.79 g/cm^3) and the relative standard uncertainty in that value (0.49% of the

Table 5-1: Total combined relative standard uncertainty in the conversion ratio, $[D_w/D_g]_{MC}$.

Uncertainty contribution	**Relative standard uncertainty in $[D_w/D_g]_{MC}$ (%)**		
	6 MV	**10 MV**	**18 MV**
Combined uncertainty in D_g due to calorimeter geometry – see Section 5.1.1	0.16	0.15	0.13
Combined uncertainty in D_w due to water phantom geometry – see Section 5.1.2	0.01	0.01	0.01
Combined uncertainty in $[D_w/D_g]_{MC}$ due to the MC cross-sections – see Section 5.1.3	0.30	0.35	0.31
Accuracy of MC transport (excluding cross-sections) – see Section 5.1.4	0.1	0.1	0.1
Statistical uncertainty of MC calculation – $[D_w/D_g]_{MC}$ – see Section 5.1.5	0.1	0.1	0.1
Combined relative standard uncertainty in $[D_w/D_g]_{MC}$ (k = 1)	*0.37*	*0.40*	*0.37*

Table 5-2: Uncertainties in calorimeter geometry and resulting uncertainty in the dose to the core, D_g at 6 MV. The estimate is nearly the same for 10 and 18 MV (see Appendix C).

Uncertainty contribution	Value	Relative standard uncertainty (k = 1)	Comment on uncertainty	Sensitivity	Comment on sensitivity	Standard uncertainty in D_g (%)
Density of three build-up plates	1.79 g/cm^3	0.49%		0.20% (change in relative dose at reference depth) per 1% increase in density	Assessed by MC density analysis	0.10
Calorimeter body density	1.79 g/cm^3	3%	variation in the manufacturer specifications	0.025% Calculated by 0.20% (change in relative dose at reference depth) per 1% increase in density × ratio of calorimeter-only depth to total reference depth (0.48/5.48)	Assessed by MC density analysis	0.05
Calorimeter vacuum gaps	0.19 cm	10%	0.02 cm, estimated from design specs and radiographs	3% per cm	Assessed by MC gap correction (calculated by gap uncertainty / gap used to calculate correction)	0.06
Plate air gaps (affecting distance to core from front of calorimeter)	0.2 cm	25%	estimated from radiographs	2% per cm	Inverse square law	0.1
Core mass	1.5622 g	0.01%		1	1:1	0.01
Combined uncertainty in D_g due to calorimeter geometry						*0.16*

plate density). It also shows the 'sensitivity'. This relates how much a 0.49% change in density affects the dose to graphite. The sensitivity is assessed for the first two density components in Table 5-2 by changing the density in the Monte Carlo code by 1% and calculating how much the dose changes at the reference depth of 5.5 cm in graphite. The standard uncertainty in the dose to graphite is the product of the relative standard uncertainty and the sensitivity.

The uncertainty in the calorimeter vacuum gaps is estimated to be 0.2 mm from the design specifications and the radiograph validation. This equates to 10% of the thickness of the vacuum gaps in the calorimeter. The sensitivity of the dose to graphite to uncertainties in the calorimeter vacuum gaps is the Monte Carlo calculated gap correction (0.57%) divided by the magnitude of the vacuum gaps. The uncertainty in the air gaps between the front plates is larger than the vacuum gap uncertainty due to the difficulties in imaging the large diameter plates (described in Section 4.3.1). The sensitivity of the plate air gaps is calculated by the inverse square law at the source-to-surface distance of 100 cm. An uncertainty in the core mass relates directly to the uncertainty in the dose to graphite so the sensitivity is unity.

5.1.2 Uncertainties due to water phantom geometry

The uncertainty associated with the modelled water tank geometry is estimated solely from the uncertainty in the water density. The Monte Carlo dose calculation uses water at 20°C

Table 5-3: Uncertainties in water phantom geometry and resulting uncertainty in the dose to water, D_w at 6 MV. The estimate is nearly the same for 10 and 18 MV (see the comment below the table).

Uncertainty contribution	Value	Relative standard uncertainty (k = 1)	Comment on uncertainty	Sensitivity	Comment on sensitivity	Standard uncertainty in D_w (%)
Density of water at 20°C	0.99821 g/cm^3	0.05%	±4 °C	0.27% (change in relative dose at reference depth) per 1% increase in density[a]	Assessed by MC density analysis	0.01
Combined uncertainty in D_w due to calorimeter geometry						*0.01*

[a] The sensitivity at 10 MV is 0.21% per 1% change in density and at 18 MV is 0.18% per 1% change in density. All three beams result in a standard uncertainty in D_w of 0.01%

and the uncertainty budget allows for variations in temperature up to ±4°C. As with the graphite density, the sensitivity of the dose to water at the reference depth of 10 cm to uncertainties in water density was assessed by a Monte Carlo study. The water density in the Monte Carlo code was changed by 1% and the resulting change in dose to water calculated. The details of the uncertainty analysis for the 6 MV beam are provided in Table 5-3.

5.1.3 Uncertainties in the Monte Carlo interaction cross-sections

An important uncertainty in Monte Carlo calculations arises from the radiation-matter interaction cross-sections. The photon interaction cross-sections are thought in general to have an "envelope of uncertainties of the order of 1% to 2%" (Hubbell, 1982). However for well-characterised low Z materials like graphite and water, the uncertainties could well be lower. Ali (2012) analysed his own graphite transmission measurements and measurements reported in the literature to arrive at a standard uncertainty of 0.35% for the NIST XCOM photon cross-sections used in EGSnrc for graphite over the range 0.1 - 40 MeV.

An estimate of the uncertainty in the Monte Carlo calculation in this particular application is obtained from the quality of the fit to the measured PDDs. The argument takes the form: *the modelled PDDs in graphite and water agree with the measured PDDs to within X%, therefore the ratio of absolute doses at the reference depths cannot be wrong by more than Y%*. Such an argument is approximate and requires that the calculated PDDs are already very close to the measured values. As with the previous two sections, this method relies on an uncertainty value and a sensitivity that relates that value to an uncertainty in the dose conversion ratio. The uncertainty value is the residual, or difference gradient between the measured and modelled PDDs. The sensitivity is established by investigating the relationship between the agreement in modelled and measured PDDs and the dose at the reference depth by changing the mass density of the water and graphite. The resulting change in dose at the reference depth is then correlated with the accompanying change in relative dose (the PDD).

The same correlation should hold if the photon interaction cross-sections are changed. A change in atomic cross-sections by a factor q should result in the same change in the corresponding macroscopic cross-sections (which are used to determine the distance to the next interaction in the Monte Carlo code). The macroscopic cross-sections are nearly proportional to mass density, so a change in atomic cross-sections can be modelled by the

same percent change in mass density. Stopping powers also change with mass density, however the depth-dose distribution for photons incident on a homogeneous phantom is, beyond the build-up region, insensitive to stopping powers[1]. Hence, the mass density may be used as an approximate surrogate to investigate the effects of errors in the photon cross-sections.

It is assumed that any errors in the cross-sections are not strongly energy dependent. Consider the 6 MV beam where nearly all of the primary photon interactions are Compton scattering events and therefore depend predominantly only on the electron density, which is proportional to the mass density. (The application of this argument to the 10 MV and 18 MV is assumed to be correct at least to first order as well.) Here the mass density argument is applied to investigate the uncertainties which arise from uncertainties in the cross-sections. That is, the changes in $[D_w/D_g]_{MC}$ and in the PDD arising from a change in density are calculated. The relationship between the dose ratio and PDD is assumed to apply equally if it were the cross-sections which were changed. The uncertainty in the measured PDD (and the residuals from the fit between the calculated and measured PDD) is then used to calculate the uncertainty in $[D_w/D_g]_{MC}$. This argument is an attempt to quantify the effect that would be produced on the dose-ratio by a mis-match between the modelled and measured PDDs. The PDDs are related to the attenuation of the beam. If the PDD is correct, then the absolute dose at the reference depth should also be correct within the derived uncertainty.

When two depth dose profiles, PDD_1 and PDD_2, are very similar, the difference between the curves can be quantified by a single number obtained by dividing one PDD by the other point-by-point and fitting a straight line to the residuals (excluding the build-up region). The gradient of the fit to PDD_1/PDD_2, m, is a measure of the difference between the two PDDs. An alternative would be to take the difference between a quantity such as the $D_{20,10}$ value for the two situations. However, by dividing the two PDDs we make use of all the data, and the result is less sensitive to noise on the individual points. The gradients of the residuals are given in Figure 3-3 for the water PDDs and Figure 3-6 for the graphite PDDs.

By forcing a change to the default density used in DOSXYZnrc for a homogenous water or graphite slab, an un-normalised PDD in a material with the default density can be compared to one with the density increased by 1%. The relative difference between the two

[1] If the electron stopping powers are increased, for example, the electron track would be contracted but the density of energy deposition would also be condensed. Provided the conditions of transient charged particle equilibrium are met, the dose deposited in a small volume of a homogenous medium would not change with an artificial variation of stopping powers, provided the photon attenuation was unchanged.

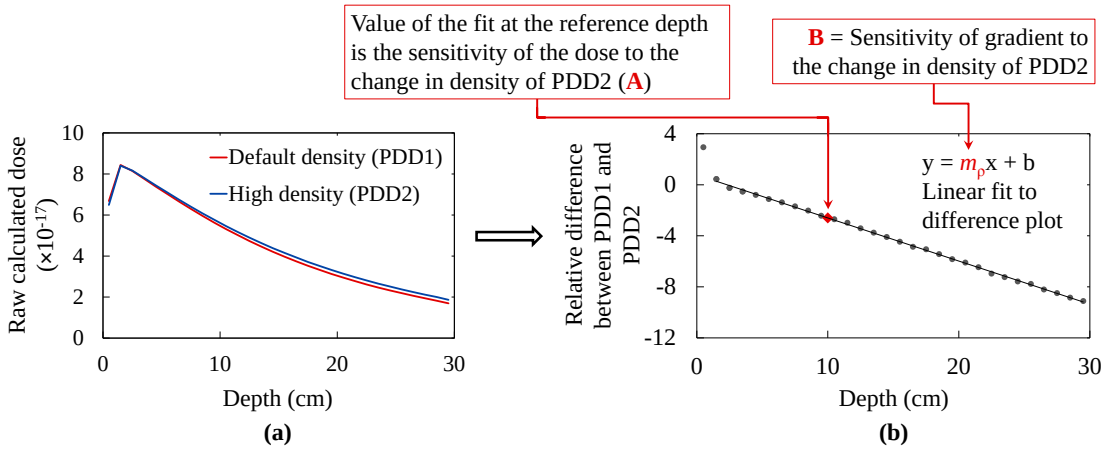

Figure 5-1: A graphical representation of the derivation of the sensitivity factors used in the uncertainty analysis for the density of water and graphite. (a) shows an exaggerated version of two un-normalised PDDs calculated using DOSXYZnrc (one with an artificially increased density) and (b) is the local relative difference between the two calculated PDDs. If a linear fit is applied to the difference plot, the gradient of the fit is the sensitivity of the gradient to the change in density of PDD2. The value of the linear fit at the reference depth, $y(10)$, is the sensitivity of the dose at the reference depth to the change in density. Although the figure in (a) shows a density difference of 10% so that the curves are visibly different, in practice a density difference of 1% is applied.

calculated doses at each depth can be plotted and the linear fit reveals the sensitivity of dose at the reference depth to the change in density. Figure 5-1 gives a visual depiction of the parameters of the sensitivity to density uncertainties. The values of these parameters are given in Table 5-4 for all three beams. The final row of this table gives the relationship between the dose at the reference depth and changes in the gradient of our PDD ratio, m_ρ. The subscript ρ is used to distinguish the gradient of the theoretical PDD ratio in the

Table 5-4: Sensitivity of dose at reference depth, and the gradient of the ratio of measured and calculated PDDs, to a change in density of water or graphite. Here m_ρ is the gradient of the ratio of two calculated PDDs in units of cm^{-1} per 1% increase in density (**B**). Quantity **C** is used to calculate the uncertainty due to an imperfect match between the measured and modelled PDD.

	Quantity	Beam	Graphite	Water	Units
	Reference depth	All	5.48	10.0	cm
A	Sensitivity of dose at reference depth, z_{ref}, to density	6 MV	-0.20	-0.27	% per 1% increase in density
		10 MV	-0.19	-0.21	
		18 MV	-0.15	-0.18	
B	Sensitivity of gradient m_ρ to density	6 MV	-5.3×10^{-4}	-3.8×10^{-4}	cm^{-1} per 1% increase in density
		10 MV	-4.1×10^{-4}	-3.2×10^{-4}	
		18 MV	-4.9×10^{-4}	-2.4×10^{-4}	
C = A/B	Change in dose at reference depth per change in gradient m_ρ	6 MV	3.7×10^{2}	7.1×10^{2}	% . cm
		10 MV	4.5×10^{2}	6.7×10^{2}	
		18 MV	3.1×10^{2}	7.6×10^{2}	

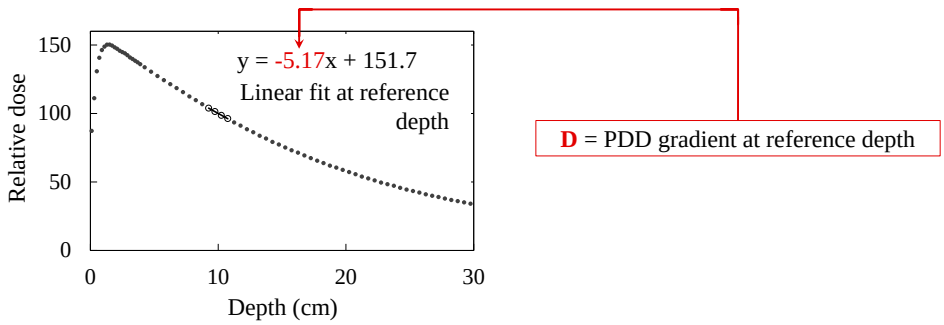

Figure 5-2: A graphical representation of the derivation of the sensitivity factor used in the uncertainty analysis for chamber positioning uncertainties. The sensitivity is determined by the gradient of the PDD at the reference depth.

density investigation from that of the residual (difference) gradient between modelled and measured data.

The last sensitivity required for the uncertainty calculation is the sensitivity of the doses in water and graphite to chamber positioning uncertainties in the PDD measurement. This is determined by the gradient of the PDD at the reference depth in the material of interest. This is shown graphically in Figure 5-2 for the 6 MV water PDD. The parameters are shown for both graphite and water for all beam qualities in Table 5-5.

Using the sensitivities in Tables 5-4 and 5-5 the effect of errors in density and PDD measurements on the ratio of doses in graphite and water can be estimated. The uncertainty contributions for the 6 MV beam are detailed in Table 5-6. Of particular note is the gradient, *m*, of the local relative difference between measured and modelled PDDs as a function of depth. The values for these are derived from the difference gradients shown in Figures 3-3 and 3-6, but have been converted from units of '% per cm' to cm^{-1} by reducing by a factor of 100. The sensitivity is obtained directly from Table 5-4.

Table 5-5: Sensitivity of dose at reference depth, and the gradient of the ratio of measured and calculated PDDs, to a change in measurement depth in water and graphite. Here the gradient at the reference depth is the relative change in dose at that point, in % per cm.

	Quantity	Beam	Graphite	Water	Units
	Reference depth	All	5.48	10.0	cm
D	Gradient of PDD at reference depth, z_{ref}	6 MV	-6.68	-5.20	% per cm
		10 MV	-5.70	-4.48	
		18 MV	-5.04	-4.40	

Table 5-6: Uncertainties in the Monte Carlo model of the linac beam and resulting uncertainty in the conversion ratio, $[D_w/D_g]_{MC}$, for the 6 MV beam. The first section relates how an imperfect match between the measured and modelled PDDs affects the dose conversion ratio and is obtained from the difference between the measured and modelled PDDs (see Figures 3-3 and 3-6). The second section combines the contributions of the uncertainty in the measured PDD. The uncertainties due to modelling and measurement are then combined to give the uncertainty in the model representation of the real beam. The combined uncertainty estimates for the 10 MV and 18 MV beams are available in Appendix C.

Uncertainty contribution	Material	Value	Standard uncertainty (k = 1)	Comment on uncertainty	Sensitivity	Comment on sensitivity	Standard uncertainty in $[D_w/D_g]_{MC}$ (%)
Uncertainty in the match between the modelled and measured beams							
Gradient, *m*, of the relative difference between measured and modelled PDDs	graphite	3.0×10^{-4} cm^{-1}	3.0×10^{-4} cm^{-1}	Difference gradients from Figs 3-3 and 3-6	3.7×10^{2} %.cm	Sensitivity of dose at the reference depth to a change in the residual gradient **(C)**	0.11
	water	-7.7×10^{-5} cm^{-1}	7.7×10^{-5} cm^{-1}		7.1×10^{2} %.cm		0.05
Combined uncertainty in the match between the modelled and measured beams							*0.12*
Uncertainty in the PDD measurement							
Density	graphite	1.79 g/cm^3	0.49%		0.20% (change in relative dose at reference depth) per 1% increase in density	Assessed by MC density analysis	0.10
	water	0.99821 g/cm^3	0.05%	±4 °C	0.27% (change in relative dose at reference depth) per 1% increase in density	Assessed by MC density analysis	0.01
EPOM	graphite	2.64 mm	Uncertainty in dose (>d_{max}) estimated directly from Tessier and Kawrakow (2010), see Section 3.3.1				0.1
	water	1.8 mm					0.1
Stopping powers	graphite water	Included in the uncertainty in EPOM					
Relative positioning of chamber	graphite	Variable	0.025 cm		-6.68% per cm	Gradient of PDD at reference depth **(D)**	0.17
	water	Variable	0.025 cm		-5.2% per cm		0.13
Combined uncertainty in the PDD measurement							*0.27*
Combined uncertainty in $[D_w/D_g]_{MC}$ *due to the model representation of the real beam*							*0.30*

[a] Uncertainties in density are expressed as a relative standard uncertainty.

5.1.4 Uncertainties due to Monte Carlo transport

Once the uncertainties in the Monte Carlo cross-sections have been isolated, the remaining uncertainty in the Monte Carlo calculation can be attributed to the accuracy of the electron transport parameters. EGSnrc differs from the earlier EGS4 code primarily in its handling of electron transport. More specifically, the new EGS version has improved handling of multiple scattering and energy loss, electron-step algorithm, boundary crossing algorithm and use of the fictitious cross-section method to determine the distance to the next interaction site. The new implementation of the condensed history technique in EGSnrc has been demonstrated by Kawrakow (2000) to be accurate against its own cross-sections to better than 0.1%.

5.1.5 Statistical uncertainty in the Monte Carlo calculation

The statistical uncertainty in the water dose and graphite dose calculated for the Monte Carlo conversion were assessed using the estimated standard deviation of the mean (ESDM) of the calculated doses. In both materials the dose was calculated using at least 12 parallel processors. (The actual number used in each case was dependent on the supercomputer availability and required accuracy.) For each parallel run the calculated dose per particle was reported along with the total number of particles that contributed to the dose calculation. The average dose, $\overline{D}$, was calculated as the weighted average of individual doses (where each parallel run was weighted by the number of particles). The standard deviation of the weighted doses was then calculated by:

Table 5-7: Number of particles contributing to and the ESDM in the dose calculations for the dose conversion ratio, $[D_w/D_g]_{MC}$.

Beam quality	Material	Number of particles	ESDM in calculated dose (%)	ESDM in conversion ratio (%)
6 MV	graphite	1.5E+10	0.07	0.09
	water	1.1E+11	0.06	
10 MV	graphite	9.8E+09	0.07	0.11
	water	9.8E+10	0.08	
18 MV	graphite	5.0E+10	0.07	0.12
	water	4.4E+10	0.09	

$$\sigma = \frac{\sqrt{\sum_i w_i \left(D_i - \overline{D}\right)^2}}{n} \tag{5.1}$$

where w_i is the weight (by number of particles) of parallel run i, D_i is the weighted dose reported from the parallel run and n is the number of parallel runs. Finally the ESDM is calculated as $\sigma/\sqrt{n}$.

Table 5-7 lists the number of particles required to reduce the ESDM in the conversion ratio, $[D_w/D_g]_{MC}$, to approximately 0.1%. The ESDM of the water and graphite doses are also listed.

5.2 Uncertainty in the clinical calibration coefficient $N_{D,w,Q_{user}}$

The calibration of a clinical chamber is performed against a reference chamber which has been calibrated against the primary standard. The entire process is depicted in Figure 5-3.

The uncertainty in the calibration coefficient of the reference chamber, $N_{D,w,ref}$, is due to the measured dose to graphite, the $[D_w/D_g]_{MC}$ conversion ratio, chamber and phantom positioning, chamber drift and repeatability and the corrections applied to the measurement. Corrections are applied for radial non-uniformity of the beam, temperature and pressure, recombination, polarity and electrometer calibration. For the purposes of this thesis the following beam quality definitions are used:

Q_0 is the ^{60}Co reference beam;

Q_{ARP} refers to any ARPANSA megavoltage beam, and

Q_{user} is a clinical beam.

The beam quality subscript refers specifically to the beam in which the measurement was performed, and not the owner of the chamber. For example, a user chamber will have a calibration coefficient $N_{D,w,Q_{ARP}}$ for the measurements performed at ARPANSA and an $N_{D,w,Q_{user}}$ once the calibration has been corrected to the user beam quality (by interpolation from the ARPANSA beam qualities). The uncertainty in the $N_{D,w,Q_{ARP}}$ of the user chamber under test (in the ARPANSA beam) includes chamber positioning, current measurement, recombination, polarity and temperature and pressure corrections and repeatability. In addition, the uncertainty in the $N_{D,w,Q_{user}}$ of the clinical chamber includes possible variations in spectra for a nominal $TPR_{20,10}$ of the users beam. Lye *et al* (2012) found spectral differences between beams with matching $TPR_{20,10}$ could result in discrepancies of

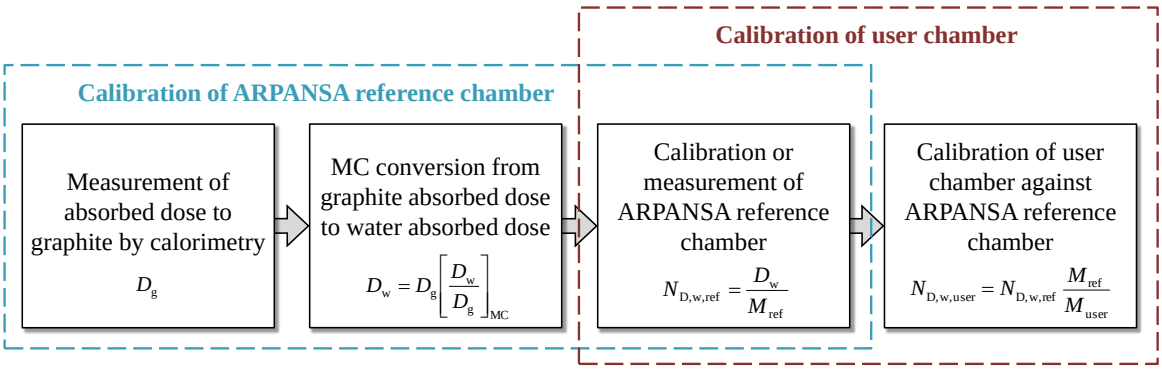

Figure 5-3: Flowchart of the complete method for the calibration of a user chamber. *M* is the charge collected during irradiation and the subscripts 'ref' and 'user' relate to the ARPANSA reference chamber and user chamber respectively. The boxes represent tasks that are performed together.

up to 0.4% in the $N_{D,w,Q_{user}}$ of an NE 2561 chamber in a nominal 6 MV beam. An uncertainty of 0.4% has been included in the $N_{D,w,Q_{user}}$ of the clinical chamber to account for this possible discrepancy. The uncertainties in the $N_{D,w,Q_{ARP}}$ for a direct calibration of the user chamber are listed in Table 5-8 with their corresponding values for each beam quality. The uncertainties in the $N_{D,w,Q_{user}}$ after interpolation to the user beam quality are shown in Table 5-9. The estimated uncertainty in the TRS-398 values of k_Q is 1% (Andreo *et al.*, 2000). When combined with the uncertainty in the calibration at the ^{60}Co beam quality, the uncertainty in $N_{D,w,Q_{user}}$ at the user beam qualities is 1.1% (k = 1). The recent AAPM TG-51 protocol addendum k_Q values (McEwen *et al.*, 2014) have a standard uncertainty of 0.4% and result in an uncertainty in $N_{D,w,Q_{user}}$ similar to this direct method.

5.3 International comparisons

Three international comparisons have been performed for the determination of absorbed dose to water in each of the three linac beams. A direct comparison of the standards of absorbed dose to water in high energy photon beams has been completed between ARPANSA and the BIPM (Picard *et al.*, 2014). In addition, ARPANSA has completed indirect comparisons with the National Research Council (NRC) Canada and the National Metrology Institute of Japan (NMIJ). Each of the comparisons and the results are described in the following sections.

In most cases the measurements upon which the comparisons are based were performed by ARPANSA staff. The only exception is the measurement in ^{60}Co for the comparison with

Table 5-8: Uncertainties in the $N_{\mathrm{D,w},Q_{\mathrm{ARP}}}$ of a clinical ionisation chamber calibrated in a megavoltage beam.

Source of uncertainty	**Relative standard uncertainty (%)**		
	6 MV	**10 MV**	**18 MV**
Determination of transfer standard $N_{\mathrm{D,w,ref}}$			
Measured dose to the calorimeter core (D_{g})	0.13	0.13	0.13
Radial non-uniformity corrections for core and chamber	0.03	0.14	0.03
Monte Carlo conversion ($[D_{\mathrm{g}}/D_{\mathrm{w}}]_{\mathrm{MC}}$)	0.37	0.40	0.37
Positioning and depth of chamber	0.17	0.17	0.17
Chamber drift	0.03	0.03	0.03
Other corrections (k_{TP}, k_{s}, k_{pol}, k_{elec})	0.08	0.08	0.08
Standard uncertainty of the mean of $N_{\mathrm{D,w,ref}}$	0.05	0.05	0.05
Combined uncertainty in determination of transfer standard $N_{\mathrm{D,w,ref}}$	*0.44*	*0.48*	*0.44*
Determination of clinical chamber $N_{\mathrm{D,w},Q_{\mathrm{ARP}}}$			
Chamber positioning	0.11	0.09	0.08
Current measurement	0.07	0.07	0.07
Other corrections (k_{TP}, k_{s}, k_{pol})	0.05	0.05	0.05
Repeatability	0.10	0.10	0.10
Combined uncertainty in determination of clinical chamber $N_{\mathrm{D,w},Q_{\mathrm{ARP}}}$	*0.17*	*0.16*	*0.15*
Combined relative standard uncertainty (k = 1)	*0.47*	*0.51*	*0.46*

Table 5-9: Uncertainties in the $N_{\mathrm{D,w},Q_{\mathrm{user}}}$ of a clinical ionisation chamber calibrated in a megavoltage beam.

Source of uncertainty	**Relative standard uncertainty (%)**		
	6 MV	**10 MV**	**18 MV**
Uncertainty in $N_{\mathrm{D,w},Q_{\mathrm{ARP}}}$ of the ionisation chamber	0.47	0.51	0.46
Spectral differences between calibration and clinical beam	0.40	0.40	0.40
Combined relative standard uncertainty (k = 1)	*0.62*	*0.65*	*0.61*

the NMIJ. The comparison results are presented here because they form a critical component in the validation of the work performed for this thesis.

5.3.1 Key comparison reference value

Internationally accepted metrology practice is to use the value reported by the BIPM as the comparison reference value. This practice is not ideal as the BIPM is a single entity that may not represent the actual value of the comparison quantity. A significant responsibility lies with the BIPM to ensure the integrity of the reference value they measure. In this respect the participant average may be a more accurate value with the advantage of many standards laboratories contributing to the value. However, the average of many participants is a changing quantity. The changeable nature of an average makes it unsuitable as a long-term reference value. For these reasons, the K6 comparison results are presented in two ways in the following section. The ARPANSA difference to the BIPM value provides a long-term equivalence value that can be used to compare the ARPANSA absorbed dose standard to other international standards. The ARPANSA difference to the participant average offers additional information concerning the accuracy of the ARPANSA absorbed dose standard.

5.3.2 Direct comparison with the BIPM

The most important comparison for the validation of the ARPANSA standard of absorbed dose to water in megavoltage beams is the BIPM.RI(I)-K6 comparison between ARPANSA and the BIPM . This comparison allows ARPANSA to establish their degree of equivalence to the international standards community. Measurements for the comparison were performed in September 2012 using the ARPANSA linac. The ARPANSA standard of absorbed dose to water is the graphite calorimeter combined with the direct Monte Carlo

Table 5-10: Key comparison BIPM.RI(I)-K6 results (KCDB, 2014). In columns 3 and 4 the ARPANSA result is shown relative to the BIPM (Picard *et al.*, 2014), and in the final two columns the ARPANSA result is compared to the average result of all participants in the comparison (Picard *et al.*, 2015).

Nominal beam energy	ARPANSA $TPR_{20,10}$	Ratio of $N_{D,w,ARPANSA}/N_{D,w,BIPM}$	ARPANSA difference to BIPM	Average of $N_{D,w,Lab}/N_{D,w,BIPM}$ ratio for all participants	ARPANSA difference to average
6 MV	0.673	0.9965 (55)	-0.35%	0.9985	-0.20%
10 MV	0.734	0.9924 (60)	-0.76%	0.9981	-0.57%
18 MV	0.777	0.9932 (59)	-0.68%	0.9958	-0.26%

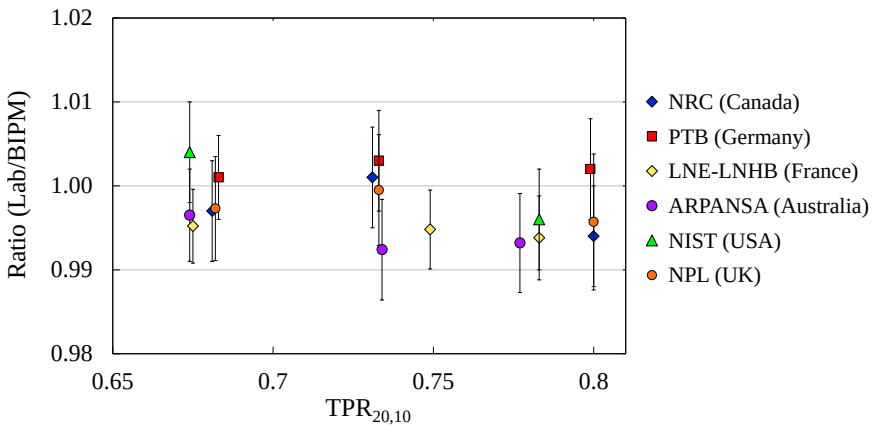

Figure 5-4: BIPM.RI(I)-K6 comparison results to date. All results are shown with reference to the BIPM $N_{\mathrm{D,w},Q_{\mathrm{ARP}}}$ and error bars include the uncertainty of the participant laboratory and the BIPM (reproduced from Picard *et al*. (2015)).

conversion. The BIPM also used a graphite calorimeter with a Monte Carlo conversion. The BIPM method includes an additional step with an ionisation chamber simulation and measurement in a graphite and a water phantom. The BIPM method is described in detail by Picard *et al* (2014). An NE 2571 ionisation chamber was used as a transfer standard and the ratio of the ARPANSA $N_{\mathrm{D,w}}$ ($N_{\mathrm{D,w,ARPANSA}}$) to the BIPM $N_{\mathrm{D,w}}$ ($N_{\mathrm{D,w,BIPM}}$) was the result of the comparison. Table 5-10 shows the comparison results between ARPANSA and the BIPM. The quantities in brackets are the relative standard uncertainty ($k = 1$) for each comparison. The results of the BIPM.RI(I)-K6 comparison for all participants to date are shown in Figure 5-4.

The ARPANSA $N_{\mathrm{D,w},Q_{\mathrm{ARP}}}$ for the 6 MV beam is in good agreement with the BIPM and with the other comparison participants. At 10 MV and 18 MV the $N_{\mathrm{D,w},Q_{\mathrm{ARP}}}$ is within 2σ of the BIPM value and within 1σ of the participant average. The largest variation of the ARPANSA $N_{\mathrm{D,w}}$ to the participant average is -0.54% for 10 MV. The radial non-uniformity correction is much larger for the 10 MV beam than for the 6 MV and 18 MV beams, and although a correction is made for this it may have some effect on the result. The low $N_{\mathrm{D,w},Q_{\mathrm{ARP}}}$ value for the 10 MV beam quality warrants further investigation.

5.3.3 Indirect comparison with the National Research Council Canada

The NRC have an established megavoltage dosimetry programme. NRC was the first participant to undertake the BIPM.RI(I)-K6 comparison in 2009 (Picard *et al.*, 2010). The NRC linac is an Elekta Precise and has three beam energies: 6 MV ($\mathrm{TPR}_{20,10}$ = 0.681),

10 MV ($TPR_{20,10}$ = 0.731) and 25 MV ($TPR_{20,10}$ = 0.800). The NRC primary standard for absorbed dose to water is a sealed water calorimeter.

In November 2012 an indirect comparison was undertaken with the NRC. The ARPANSA $N_{\mathrm{D,w},Q_{\mathrm{ARP}}}$ was measured for two model NE 2571 chambers. The chambers were then sent to NRC and the calibration coefficients, $N_{\mathrm{D,w},Q_{\mathrm{NRC}}}$, were measured in their linac beams. The measured $N_{\mathrm{D,w},Q_{\mathrm{NRC}}}$ were interpolated to the ARPANSA beam qualities and compared to the calibration coefficients measured at ARPANSA. A third order polynomial fit was used for the interpolation. It is worth noting the interpolation for the 18 MV beam covers a large energy span in both directions. The results of the comparison are shown in Table 5-11.

The uncertainty in the ratio of $N_{\mathrm{D,w}}$ coefficients is calculated by summation in quadrature of the following contributions:

- $N_{\mathrm{D,w},Q_{\mathrm{ARP}}}$: The uncertainty in the ARPANSA calibration coefficient as described in Table 5-8.
- $N_{\mathrm{D,w},Q_{\mathrm{NRC}}}$: The uncertainty in the NRC calibration coefficient. A value of 0.37% was reported for all beam qualities.
- *Interpolation*: The uncertainty in the interpolated $N_{\mathrm{D,w}}$ due to the chosen method of interpolation. The difference between coefficients calculated using second-order and third-order polynomials is less than 0.1%. 0.1% was used in the uncertainty calculation.
- *Spectral uncertainty*: As previously mentioned, Lye *et al.* (2012) found spectral differences for a matching $TPR_{20,10}$ could result in up to 0.4% variation in chamber responses. Since the interpolation relies solely on $TPR_{20,10}$, 0.4% has been included in the uncertainty estimate.

The two calibration coefficients agree well at 6 MV. At 10 MV the comparison result is just within 1σ and the $N_{\mathrm{D,w}}$ measured at ARPANSA in the 18 MV beam is within 2σ of the

Table 5-11: Results of the comparison between NRC and ARPANSA. The results presented are the average ratios of calibration coefficients of the two NE 2571 chambers used in the comparison.

Nominal beam energy	ARPANSA $TPR_{20,10}$	Ratio of $N_{\mathrm{D,w,ARP}}$ / $N_{\mathrm{D,w,NRC}}$	ARPANSA difference to NRC
6 MV	0.673	0.9954 (72)	-0.46%
10 MV	0.734	0.9929 (75)	-0.71%
18 MV	0.777	0.9920 (71)	-0.80%

$N_{D,w}$ interpolated from the NRC measurements. The results follow a similar trend to those obtained in the BIPM.RI(I)-K6 comparison between ARPANSA and the BIPM. However, based on the ARPANSA and NRC key comparison results, this comparison result at 18 MV is lower than expected.

5.3.4 Indirect comparison with the National Metrology Institute of Japan

The NMIJ have a long established calibration service for the absorbed dose to water in ^{60}Co and have recently developed their procedures for direct megavoltage calibrations. They are due to undertake the BIPM.RI(I)-K6 comparison in 2015. The NMIJ linac is an Elekta K. K., Precise and has three beam energies: 6 MV ($TPR_{20,10}$ = 0.679), 10 MV ($TPR_{20,10}$ = 0.729) and 15 MV ($TPR_{20,10}$ = 0.758). As for ARPANSA, the NMIJ primary standard is based on a Domen-type graphite calorimeter.

In May 2013, three ionisation chambers calibrated in the NMIJ linac beams (with calibration coefficients $N_{D,w,Q_{NMIJ}}$) were brought to ARPANSA for comparison. The chambers were an Exradin A12 and two PTW 30013 chambers. Details of the comparison have been published (Shimizu *et al.*, 2015). A quadratic interpolation was applied to the $N_{D,w,Q_{NMIJ}}$ coefficients to obtain calibration coefficients at the ARPANSA beam qualities. The results of the comparison are shown in Table 5-12.

The uncertainty in the ratio of $N_{D,w}$ coefficients is calculated by summation in quadrature of the following contributions:

- $N_{D,w,Q_{ARP}}$: The uncertainty in the ARPANSA calibration coefficient as described in Table 5-8.
- $N_{D,w,Q_{NMIJ}}$: The uncertainty in the NMIJ calibration coefficient. A value of 0.40% was used for all beams (Shimizu *et al.*, 2015).

Table 5-12: Results of the comparison between NMIJ and ARPANSA. The PTW 30013 results are the average ratios of calibration coefficients of the two chambers used in the comparison.

Nominal beam energy	ARPANSA $TPR_{20,10}$	PTW 30013		Exradin A12	
		Ratio of $N_{D,w,ARP}$ / $N_{D,w,NMIJ}$	ARPANSA difference to NMIJ	Ratio of $N_{D,w,ARP}$ / $N_{D,w,NMIJ}$	ARPANSA difference to NMIJ
6 MV	0.673	1.0001 (73)	0.01%	0.9998 (74)	-0.02%
10 MV	0.734	0.9977 (76)	-0.23%	0.9959 (76)	-0.41%
18 MV	0.777	0.9936 (73)	-0.64%	0.9920 (74)	-0.80%

- *Interpolation*: The difference between the NMIJ calibration coefficients calculated using second order and third order polynomials is 0.1% for the 6 MV and 10 MV beams and this value was used in the calculation. The 18 MV beam requires extrapolation rather than interpolation since the highest energy NMIJ beam is 15 MV. The uncertainty for this was estimated using a comparison of a quadratic fit to all data and a linear fit to the 10 MV and 15 MV data points, and an uncertainty of 0.15% was used.
- *Spectral uncertainty*: As with the NRC comparison, a value of 0.4% has been included to account for differences in chamber response due to spectral variations in the $TPR_{20,10}$ beam quality definition.
- *Sleeve effect*: An additional 0.12% uncertainty was included in the uncertainty of the Exradin A12 chamber measurement due to the use of a waterproof sleeve in the NMIJ laboratory.

The NMIJ method of obtaining absorbed dose to water is very similar to that of ARPANSA: both use a graphite calorimeter and both use an EGS Monte Carlo calculation to convert from dose to graphite to dose to water (NMIJ use EGS5 and ARPANSA use EGSnrc). The similarity in methods leads to correlations in the uncertainties. Correlations for the Monte Carlo transport parameter and the heat defect of graphite combine to 0.15%. This is removed from the factors above to reach the final comparison uncertainty.

This uncertainty analysis is slight different to that presented by Shimizu *et al*. (2015). Shimizu *et al*. estimated an uncertainty of 0.3% for the interpolation and did not include a separate component for the possible spectral differences or remove correlated uncertainties. The resulting uncertainties using the two methods differ by only 0.05%.

The comparison results for both chamber types at 6 MV and 10 MV agree to within 1σ. At 18 MV the PTW 30013 chamber results agree within 1σ but the Exradin A12 ratio is just outside the 1σ limit. The results of all three comparisons are plotted together in Figure 5-5. This figure shows a consistent trend: the ARPANSA calibration coefficients are lower than those of their international counterparts, and get slightly lower for higher energies. Note that the results are interpolated to the ARPANSA $TPR_{20,10}$ values but are separated slightly on the plot for clarity of display.

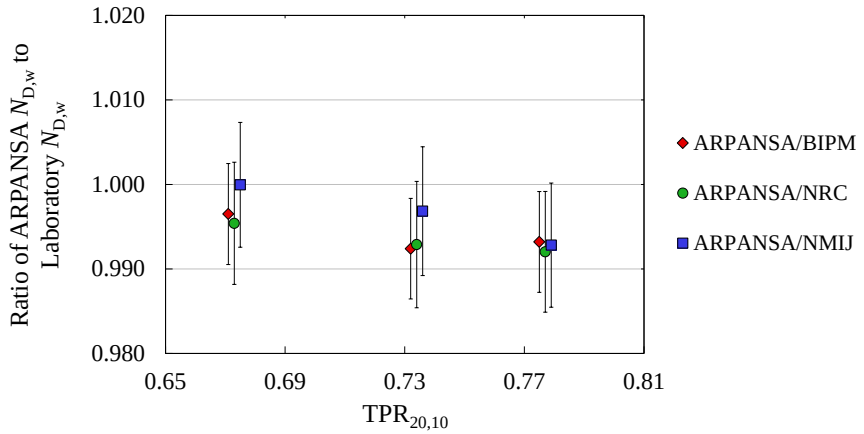

Figure 5-5: Results of the three international comparisons performed by ARPANSA. At each $TPR_{20,10}$ value the results are separated by a $TPR_{20,10}$ of 0.002 so the individual points can be seen. The results for the ARPANSA/NMIJ comparison are the averages of the two chamber types at each energy (reproduced from Butler *et al*. (2014)).

5.4 Consistency of comparison results

Comparisons between multiple international standards laboratories create closed loops that enable us to assess the agreement between primary standards laboratories. The comparison between ARPANSA and the NRC is one such example. The BIPM has performed K6 comparisons with both laboratories. If we assume the BIPM measurement should be self-consistent, the ratio of K6 comparison results ($\left(N_{\mathrm{D,w}}\right)_{\mathrm{BIPM}}^{\mathrm{ARP}} / \left(N_{\mathrm{D,w}}\right)_{\mathrm{BIPM}}^{\mathrm{NRC}}$) should be equivalent to $\left(N_{\mathrm{D,w}}\right)_{\mathrm{NRC}}^{\mathrm{ARP}}$ obtained during the ARPANSA:NRC comparison performed in November 2012. Table 5-13 and Figure 5-6 show all the comparison results and the table lists the differences between the two ARPANSA:NRC comparison methods. The beam qualities at NRC are somewhat different to those at ARPANSA. All results have been interpolated (or extrapolated in the case of the 6 MV beam) to the ARPANSA beam qualities. The relative standard uncertainty (k = 1) of each comparison value is shown in brackets.

Figure 5-6(a) shows the results of the K6 comparisons with the BIPM. In Figure 5-6(b) the closed purple circles are the direct ARPANSA:NRC comparison results. The open purple circles are the indirect ARPANSA:NRC comparison via the BIPM K6 comparison. These should be in agreement. Although the results are separated by up to 0.54%, the relative standard uncertainties on each of these points is 0.7-0.8% so there is no statistical difference between them at the 1σ level. This is an important outcome in the context of international consistency of absorbed dose standards.

Table 5-13: Results of comparisons of absorbed dose to water between ARPANSA, NRC and the BIPM. The NRC K6 comparison results shown in the table are extrapolated (6 MV) or interpolated (10 MV and 18 MV) from those at the NRC beam qualities (Picard *et al.*, 2010). The relative standard uncertainty is shown in brackets for each result. In the ratio of K6 results (column 4) the BIPM results should cancel so the ratio should be comparable to the direct comparison between ARPANSA and NRC. The differences between the K6 ratio and the direct ARPANSA:NRC comparison are shown in column 6 and are less than the uncertainties in the values being compared.

ARPANSA $TPR_{20,10}$	**ARPANSA K6 result: $N_{D,w,ARP}$ / $N_{D,w,BIPM}$ [A]**	**NRC K6 result: $N_{D,w,NRC}$ / $N_{D,w,BIPM}$, extrap./interp. to ARPANSA $TPR_{20,10}$ [B]**	**Ratio of ARPANSA and NRC K6 results (A/B) [C]**	**Result of ARPANSA:NRC comparison ($N_{D,w,ARP}$ / $N_{D,w,NRC}$) [D]**	**Difference between K6 ratio (C) and measured comparison (D) (%)**	**Difference between ARPANSA and NRC $TPR_{20,10}$ qualities (%)**
0.673	0.9965 (55)	0.996 (6)	1.0008 (81)	0.9954 (72)	0.54	1.2
0.734	0.9924 (60)	1.001 (6)	0.9919 (85)	0.9929 (75)	-0.10	-0.4
0.777	0.9932 (59)	0.997 (6)	0.9957 (84)	0.9920 (71)	0.37	2.9

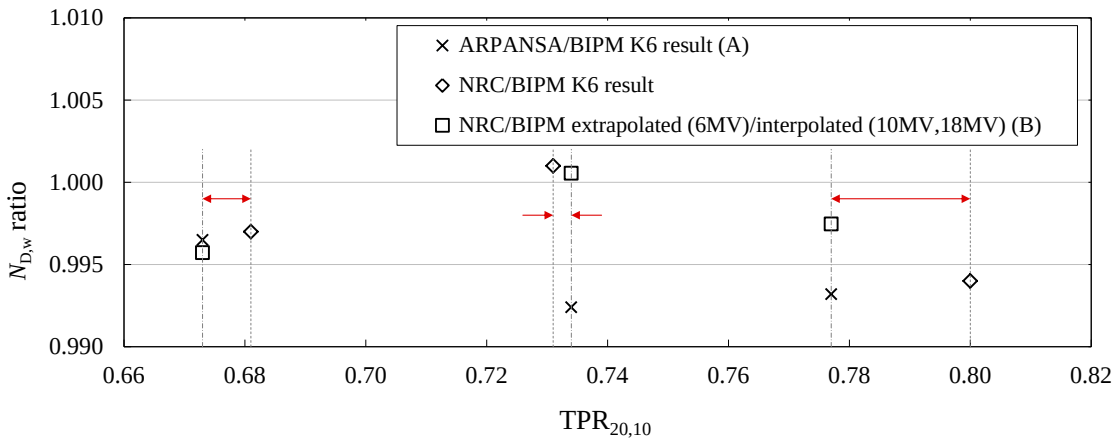

(a)

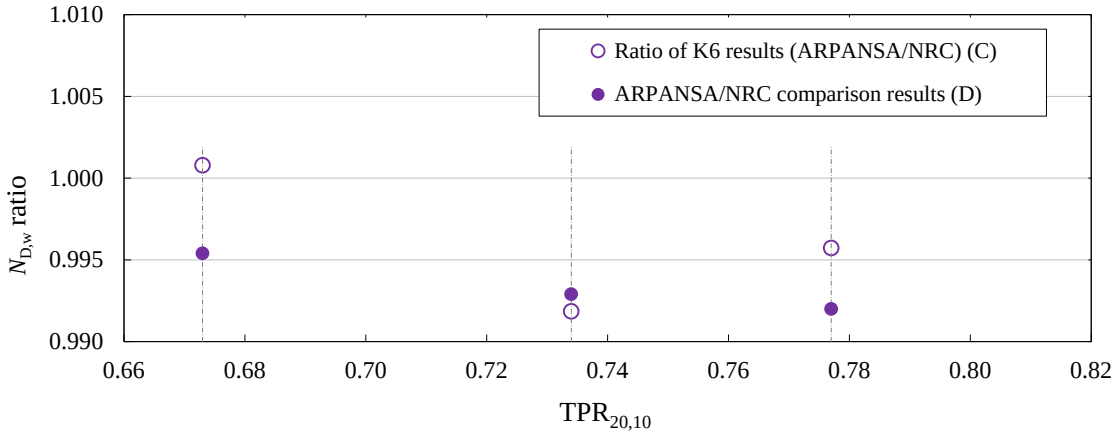

(b)

Figure 5-6: The results of comparisons between ARPANSA, NRC and the BIPM. The black markers in (a) show the individual K6 comparison results. The red arrows indicate the interpolation or extrapolation distance from NRC to ARPANSA for each beam quality. The purple markers in (b) represent the direct (solid) and indirect (open) ARPANSA/NRC ratios and should be in agreement. The relative standard uncertainties on the points in (b) range from 0.71 to 0.85%.

Table 5-14: Uncertainties in the direct ARPANSA:NRC comparison. The correlated uncertainty in the Monte Carlo transport, shown in brackets, is subtracted in quadrature from the other uncertainty contributions.

Source of uncertainty	**Relative standard uncertainty (%)**		
	6 MV	**10 MV**	**18 MV**
Uncertainty in $N_{D,w,Q_{ARP}}$ of the ionisation chamber	0.47	0.51	0.46
Uncertainty in $N_{D,w,Q_{NRC}}$ of the ionisation chamber	0.37	0.37	0.37
Uncertainty due to interpolation method	0.1	0.1	0.1
Spectral range of nominal beam quality ($TPR_{20,10}$)	0.4	0.4	0.4
Correlated uncertainty in the MC transport	(0.1)	(0.1)	(0.1)
Combined relative standard uncertainty (k = 1)	*0.72*	*0.75*	*0.71*

For the K6 comparison results (**A** and **B**) the uncertainties are taken directly from the published K6 comparison articles (Picard *et al.*, 2010; Picard *et al.*, 2014). The uncertainty in the indirect ARPANSA:NRC comparison (**C**) is calculated by summing the uncertainties in **A** and **B** in quadrature. The uncertainty calculation for the direct ARPANSA:NRC comparison (**D**) is shown in Table 5-14. The first four components are summed in quadrature and the final component for the correlated uncertainty in the Monte Carlo transport (shown in brackets) is subtracted in quadrature to reach the combined relative standard uncertainty in the direct comparison between ARPANSA and NRC.

5.5 Measured energy corrections (k_Q)

In ionisation chamber measurements an energy correction factor, k_Q, is required to correct the chamber calibration coefficient from the calibration beam quality to the measured beam quality. Previously the most common approach was to calibrate a chamber in ^{60}Co and apply a calculated k_Q factor. This is still the case in Australia where the current recommendation by the Australasian College of Physical Scientists and Engineers in Medicine (ACPSEM) is to use a generic calculated k_Q value interpolated from the values tabulated by the International Atomic Energy Agency in its code of practice TRS-398. These k_Q values were calculated for each chamber type as the ratios of the Spencer-Attix water/air stopping powers ratios and chamber perturbation corrections at the user and reference beam qualities and do not include any correction for stem effects. Many authors have published measured k_Q values for a number of chambers (Aalbers *et al.*, 2008 (rev. 2012); Delaunay, 2013; Katumba, 2010; Krauss and Kapsch, 2007; Krauss and Kapsch, 2014; González-Castaño *et al.*, 2009; McEwen, 2010; Palm and Mattsson, 2002; PTB, 2008; Seuntjens *et al.*, 2000; Stucki *et al.*, 2003; Thomas *et al.*, 2008). In addition, Muir and Rogers (2010) have modelled the k_Q values for various chambers and their results are consistent with the published measured values. These modelled k_Q values have been incorporated into the recent addendum to the AAPM TG-51 protocol (McEwen *et al.*, 2014) with a standard uncertainty of 0.4%.

The comparison of k_Q values measured at ARPANSA with other measured values reveals how the measurements of absorbed dose at ARPANSA compare with those performed at other laboratories. The k_Q values have been measured for the four most common clinical reference chambers used in Australia. These chambers are the Farmer chamber (model NE 2571) and the NE 2561/NE 2611, IBA FC65-G and PTW 30013 Farmer-type chambers and some of their key characteristics are listed in Table 5-15. The average measured k_Q values for each chamber type are presented in Table 5-16. As with the comparisons of

absorbed dose to water presented in Section 5.3, the measurements of k_Q values presented below were performed by my ARPANSA colleagues.

Figures 5-7, 5-8, 5-9 and 5-10 show the ARPANSA measured k_Q values alongside the values from TRS-398, Muir and Rogers' modelled values and other recent measured values. The TRS-398 values tend to be higher than measured values but include a 1% standard uncertainty. The NE 2571 and NE 2561/NE 2611 are graphite walled chambers that have historically been used as transfer standards for air kerma and absorbed dose measurements. For both of these chamber types the ARPANSA measured k_Q values trend lower than the TRS-398 values but are consistent with the modelled k_Q values. For the NE 2571 the measured data are also consistent with the ARPANSA results. The measured data for the NE 2561/NE 2611 tend to agree with the TRS-398 k_Q values at the lower beam qualities and fall toward the modelled values at the higher beam qualities. Although the data are quite spread, they agree within the 1σ limit.

Table 5-15: Physical characteristics of the four reference class chambers presented in the comparison of measured k_Q values (Andreo *et al.*, 2000).

	NE 2571	NE 2561 / NE 2611A	PTW 30013	IBA FC65-G
Cavity volume (cm^3)	0.6	0.33	0.6	0.67
Cavity length (mm)	24.0	9.2	23.0	23.0
Cavity radius (mm)	3.2	3.7	3.1	3.1
Wall material	graphite	graphite	PMMA (inner graphite layer)	graphite
Wall thickness (g/cm^2)	0.065	0.090	0.057	0.068
Central electrode material	aluminium	aluminium (hollow)	aluminium	aluminium
Waterproof	no	no	yes	yes

Table 5-16: Average measured k_Q values for the four most common clinical reference chambers in Australia. The relative standard uncertainty is shown in brackets for each value.

Chamber type	**Number of chambers**	**Beam quality**		
		6 MV ($TPR_{20,10}$ = 0.673)	**10 MV ($TPR_{20,10}$ = 0.734)**	**18 MV ($TPR_{20,10}$ = 0.777)**
NE 2571	2	0.9896 (61)	0.9773 (63)	0.9653 (59)
NE 2611A	1	0.9904 (61)	0.9778 (63)	0.9646 (59)
IBA FC65-G	3	0.9847 (61)	0.9730 (63)	0.9615 (59)
PTW 30013	7	0.9837 (61)	0.9705 (63)	0.9585 (59)

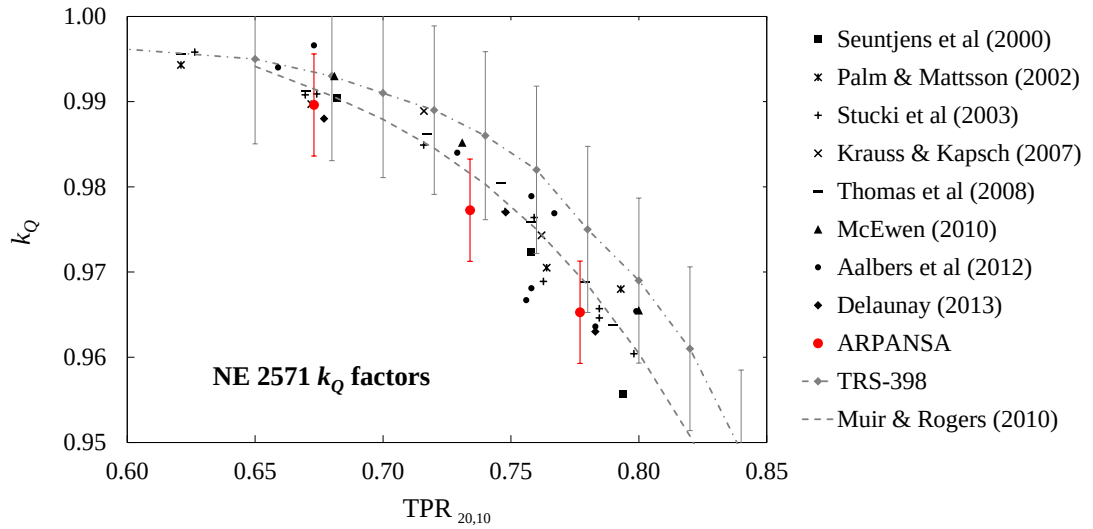

Figure 5-7: Experimental and modelled values of k_Q for an NE 2571 chamber. The values recommended by TRS-398 are also shown for comparison. The uncertainty bars on the TRS-398 data are at 1% and on the ARPANSA data are at 0.6% showing the k = 1 uncertainty on the points. The uncertainty on all points shown without uncertainty bars is of the order of 0.4 – 1%.

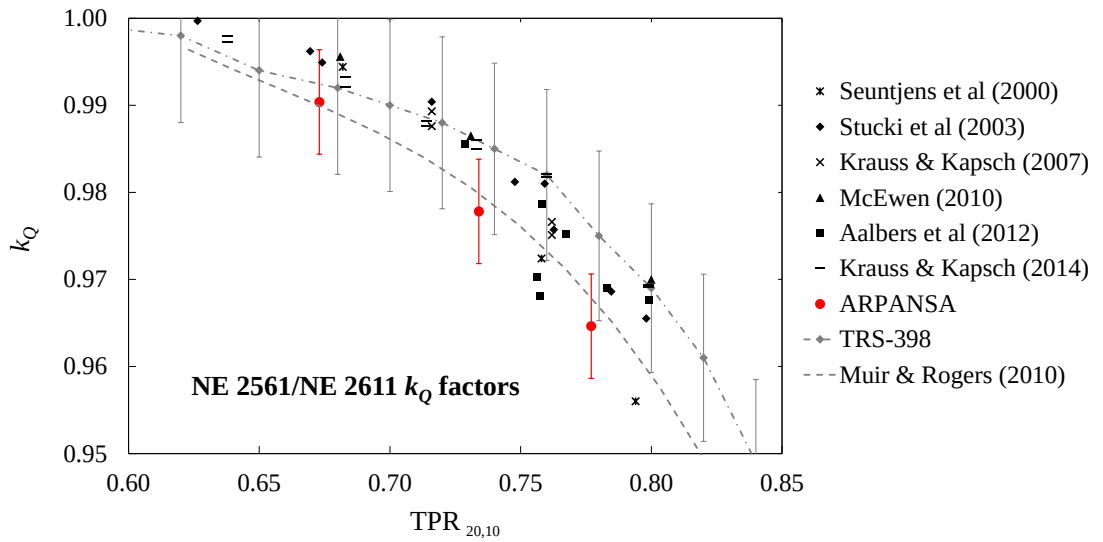

Figure 5-8: Experimental and modelled values of k_Q for an NE 2561/NE 2611 chamber. The values recommended by TRS-398 are also shown for comparison. The uncertainty bars on the TRS-398 data are at 1% and on the ARPANSA data are at 0.6% showing the k = 1 uncertainty on the points. The uncertainty on all points shown without uncertainty bars is of the order of 0.4 – 1%.

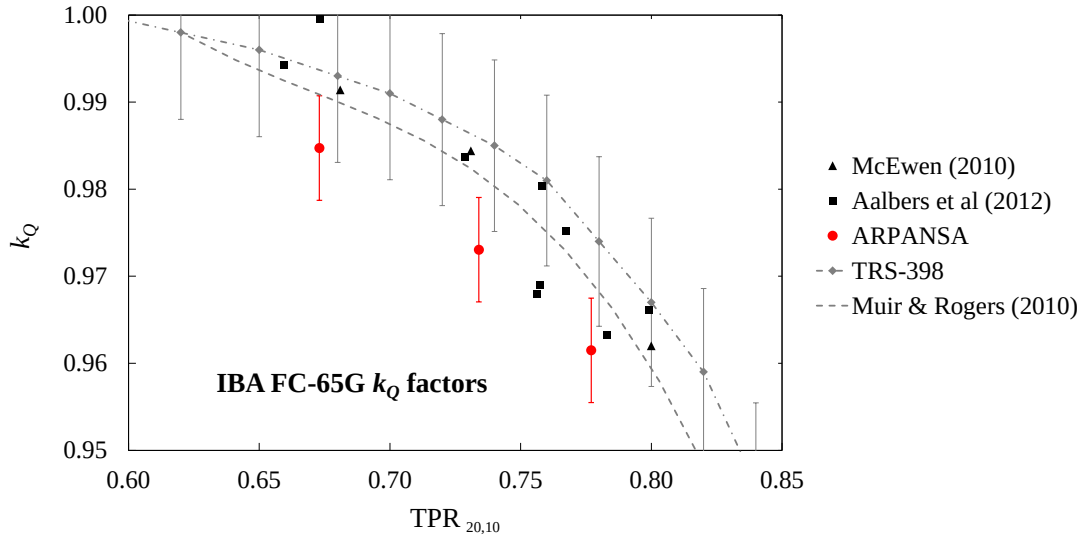

Figure 5-9: Experimental and modelled values of k_Q for an IBA FC65-G chamber. The values recommended by TRS-398 are also shown for comparison. The uncertainty bars on the TRS-398 data are at 1% and on the ARPANSA data are at 0.6% showing the k = 1 uncertainty on the points. The uncertainty on all points shown without uncertainty bars is of the order of 0.4 – 1%.

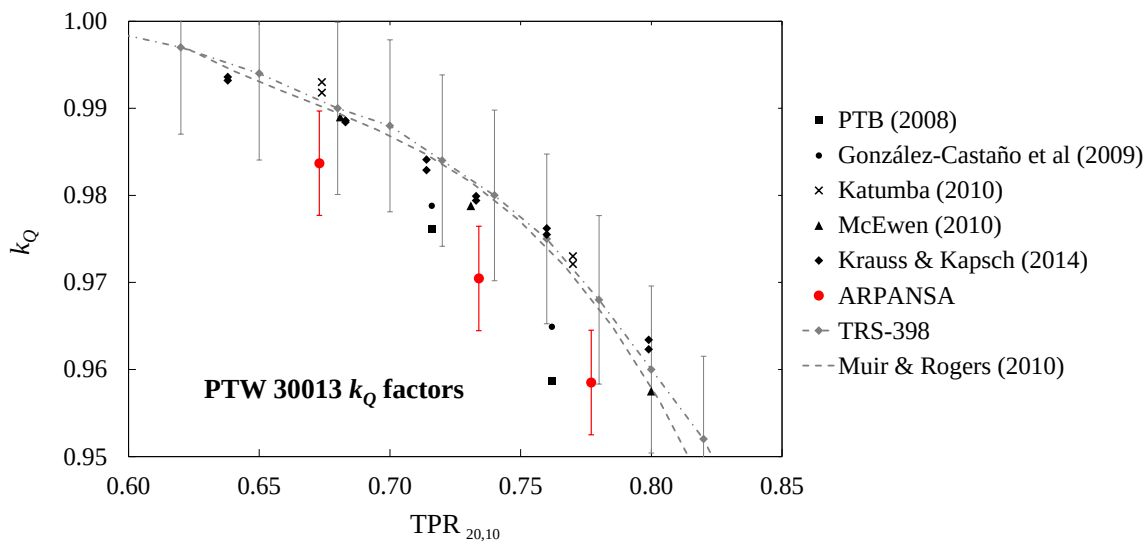

Figure 5-10: Experimental and modelled values of k_Q for a PTW 30013 chamber. The values recommended by TRS-398 are also shown for comparison. The uncertainty bars on the TRS-398 data are at 1% and on the ARPANSA data are at 0.6% showing the k = 1 uncertainty on the points. The uncertainty on all points shown without uncertainty bars is of the order of 0.4 – 1%.

The IBA FC65-G and Exradin A12 are part of the newer generation of waterproof chambers. They are increasingly being adopted in the clinical environment as evidenced by the increasing number ARPANSA receive for calibration. Calculated and modelled k_Q values are available in TRS-398 and Muir and Rogers (2010), however there are less data available for measured k_Q factors than for the older generation of graphite chambers. The ARPANSA k_Q values for the FC65-G sit very low compared to the calculated and modelled values, but remain within 1σ of both as seen in Figure 5-9. This chamber type has very few measured data points so it is difficult to draw conclusions but the data appear consistent with ARPANSA at the higher energies.

The PTW 30013 is the only chamber considered here where the values in TRS-398 agree very well with Muir and Rogers' (2010) modelled values. As shown in Figure 5-10, the 6 MV and 18 MV points are within 1σ of the modelled values, and the 10 MV point is in the 1σ to 2σ range, however the ARPANSA agreement with other measured data appears to be better than for the FC65-G.

Taking all the comparisons of absorbed dose and k_Q values into consideration, it is clear that the standard for absorbed dose to water in high energy photon beams at ARPANSA is on the low side of megavoltage photon beams and is lower than its own standard for absorbed dose to water in ^{60}Co. Despite this trend, the majority of comparison results agree within 1σ. Variations between international standards and between the ARPANSA standards at ^{60}Co and high energy photon energies have implications for clinical users of the primary standard, and these must be considered. This is one of the topics for discussion in Chapter 6.

CHAPTER 6 KEY RESULTS AND DISCUSSION

The work presented in this thesis has shown that the new ARPANSA method of direct calibrations using a Monte Carlo conversion from absorbed dose to graphite produces results consistent with other absorbed dose to water standards in high energy photon beams. The key points for discussion are the consistency of comparison results and the flow on effects of the new direct calibration method for radiotherapy clinics. The latter is an important point as any shift in the calibration coefficient of a clinical reference chamber will affect the beam calibration and dose delivered to patients. The uncertainty in this method is also compared to the uncertainties in other primary standard methods using graphite calorimeters.

6.1 The importance of dose

Before considering the clinical effect of the direct calibration method, there are three important concepts relating to dose that should be discussed.

1. How accurate is the measurement of dose?
2. Is dose measurement consistent between radiotherapy providers?
3. How does dose now compare to historical data?

Good patient outcomes depend on all of these factors. They are addressed in the following paragraphs.

Fundamentally, absorbed dose is defined as the amount of energy deposited per unit mass of a medium. Absorbed dose is measured independently by many primary standards institutions. This process was described broadly in Chapter 2 and in more detail for graphite calorimetry in Chapter 4. Outside primary standards laboratories, absorbed dose is measured in clinical beams by ionisation chambers that collect the charge created by radiation interactions in the air cavity inside the chamber. A calibration traceable to the primary standard of absorbed dose relates the charge collected (in nC) to the absorbed dose to water (in Gy).

The accuracy of the dose delivered during a patient treatment relies on accuracy in all steps from the determination of absorbed dose in the primary standards laboratory to the calibration of the clinical beam output. Dose accuracy is the first step in ensuring the quality of radiotherapy treatment delivery.

It is noted however that if all the radiotherapy providers in the world had been incorrect by the same amount, and continue to be so, there would be no effect on the efficacy of radiotherapy. Treatment outcomes are only indirectly related to dose. The more important factor is how the human tissues respond to the dose delivered and this is determined through clinical experience. The provision of an absorbed dose standard simply facilitates consistency in radiotherapy dose delivery.

A change to the absorbed dose standard without regard to the relationship between dose and clinical outcomes has the potential to affect the tumour control and normal tissue toxicity in patients. In a clinical environment, dose prescriptions are based primarily on experience of previous clinical outcomes. When a clinic begins a new treatment protocol, it has no history so its experience is drawn from other facilities' experiences. This is achieved through publications that relate treatment protocols including dose prescriptions and fractionation schemes to patient survival and toxicity outcomes. As the clinic gains experience with similar treatments, its own history becomes more important in guiding its prescriptions.

It is important for the dose delivered to patients to be correct. However, if improvements in the determination of absorbed dose in the primary standards laboratory cause changes in the beam calibration, the effect on dose prescriptions must also be considered. The equivalence of dose and related outcomes is the second important dose consideration required for positive radiotherapy outcomes.

Consistency of absorbed dose nationally and internationally is important for the sharing of treatment protocols. In addition, the efficacy of multi-centre clinical trials depends on the consistency of dose between facilities. Dose consistency allows for collation of trial results and reduces the uncertainty in the doses reported in the clinical trial. The advantage of this is twofold: fewer patients are required in the trial and the trial results are more reliable. This is important as clinical trials often form the basis of dose prescriptions for new treatment modalities and fractionation schemes worldwide.

Consistency of dose measurements is achieved through a number of methods. The purpose of international comparisons such as the K6 comparison described throughout this thesis is to ensure consistency among primary standards laboratories. Consistency between clinics is achieved through traceability to a primary standard. Finally, the IAEA Codes of Practice (Andreo *et al.*, 2000) and the AAPM protocol (Almond *et al.*, 1999; McEwen *et al.*, 2014) provide guidance on calibration methods to ensure consistency in the implementation of the dose calibration provided by the standards laboratory.

Consistency of absorbed dose is the third important dose consideration required for quality radiotherapy treatments. However, given the spread between the TRS-398 k_Q values, the Muir and Rogers k_Q values used in the TG-51 protocol addendum and results from NMIs already offering direct megavoltage photon calibration services, achieving this international consistency is a non-trivial task.

6.2 Comparison of other uncertainties

It is important to assess whether the uncertainties in the ARPANSA method are comparable to uncertainties by other methods. This assessment serves as a quality control check on the ARPANSA uncertainty calculation, and indicates whether the optimum precision in absorbed dose measurement has been achieved. To date six laboratories (including ARPANSA) have published results of the K6 comparison with the BIPM. Of those laboratories, ARPANSA, NPL, LNE-LNHB and the BIPM all use graphite calorimeters with a Monte Carlo conversion to achieve absorbed dose to water. Although the methods differ slightly, the uncertainties in the ARPANSA conversion factor should be similar to those of the conversion factors used by other laboratories. In Figure 6-1 the uncertainties in the Monte Carlo conversion factors for all four laboratories are compared. The photon energies are grouped into three ranges: low (6 MV), medium (10-12 MV) and high (18-25 MV). The ARPANSA uncertainties are higher compared to the other laboratories but are in broad agreement given the spread of values.

The uncertainty in the ARPANSA determination of the transfer chamber calibration coefficient should also be comparable to those at other primary standards laboratories. The uncertainties in the calibration coefficients from all K6 comparisons performed to date are compared in Figure 6-2. Once again they are grouped into the three photon energy ranges described above. The ARPANSA uncertainties are consistent with the other laboratories for all three beam qualities.

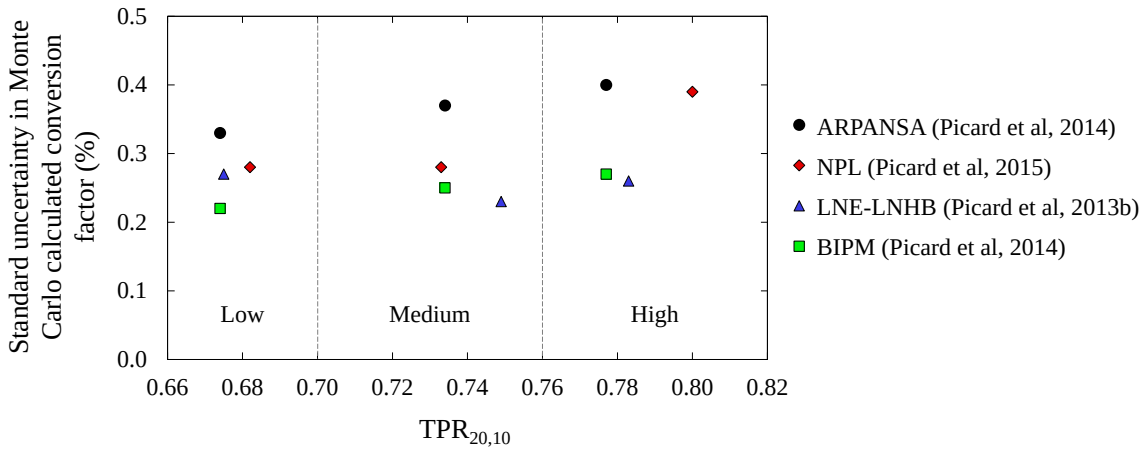

Figure 6-1: Uncertainties in the factors used to convert from absorbed dose to graphite measured with a graphite calorimeter to absorbed dose to water by primary standards laboratories. The dashed vertical lines indicate the grouping of comparisons in terms of energy ranges. In 2009 the $TPR_{20,10}$ values for the 6 MV beams used in Australia ranged from 0.661 to 0.687 (Lye *et al.*, 2012).

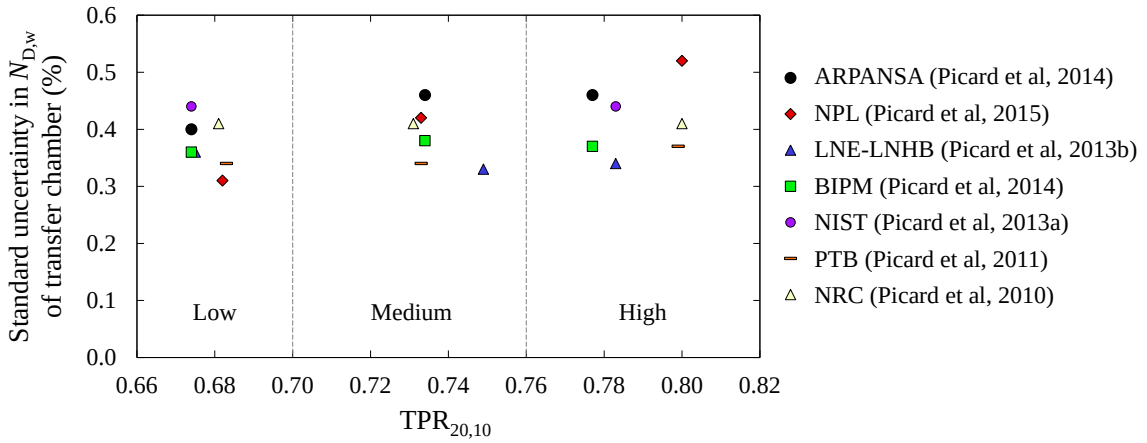

Figure 6-2: Uncertainties in the calibration coefficients ($N_{D,w}$) of transfer chambers from the K6 comparison at each of the laboratories. Since the BIPM has participated in all of the comparisons, the uncertainty shown was taken from the comparison with ARPANSA. The dashed vertical lines indicate the grouping of comparisons in terms of energy ranges.

6.3 Clinical effect of the direct calibration method

A change in the calibration coefficient of an ionisation chamber will result in a change in the therapeutic patient doses being delivered. Although the direct calibration method offers an improved uncertainty, the effect of the direct megavoltage calibration method on a chamber $N_{D,w,Q_{user}}$ must still be evaluated. For comparison purposes the $N_{D,w,Q_{ARP}}$ achieved for an NE 2571 chamber by the direct calibration method has been assessed against a ^{60}Co calibration using a k_Q interpolated from TRS-398 and the third order polynomial fit to the

k_Q values modelled by Muir and Rogers (2010). The NE 2571 is not waterproof and was placed in a waterproof sleeve during measurements. The tabulated k_Q values in TRS-398 include a 0.5 mm sleeve for non-waterproof chambers. A 1 mm PMMA sleeve is also included in the models for the k_Q values of non-waterproof chambers reported by Muir and Rogers (2010). Table 6-1 shows the calibration coefficients of an NE 2571 chamber calibrated in a ^{60}Co beam with the k_Q values from TRS-398 and Muir and Rogers applied for the ARPANSA beam qualities. The values of $N_{\mathrm{D,w},Q_{\mathrm{ARP}}}$ in the third column were obtained by the direct calibration method for the same chamber. The final two columns show the differences that can be expected when using the direct calibration method compared to the current TRS-398 k_Q values or the Muir and Rogers k_Q values.

Reviewing the results in Table 6-1 for the NE 2571 chamber, a direct calibration will cause a shift in the beam calibration of between 0.4% and 1.1% (with the chamber calibration coefficient being smaller, resulting in the linac output being higher and patients receiving more dose). The estimated uncertainty in an $N_{\mathrm{D,w}}$ based on a TRS-398 k_Q correction is 1.1%. It is important to realise that this shift will be consistent with an international shift moving from the calculated k_Q values in the original TG-51 protocol to the TG-51 protocol addendum with the Muir and Rogers (2010) modelled k_Q values.

The $N_{\mathrm{D,w},Q_{\mathrm{user}}}$ shift is dependent on the chamber type and other chamber models must also be considered. Many clinics are now opting for waterproof chambers as their reference chamber. Table 6-2 shows the expected shift in $N_{\mathrm{D,w}}$ values from a ^{60}Co calibration for the four most common reference class chambers in Australia. $N_{\mathrm{D,w}}$ shifts are shown for the IAEA k_Q values and the Muir and Rogers k_Q values recommended by the AAPM TG-51 protocol addendum. For this discussion references to the AAPM k_Q values will be referring

Table 6-1: Values of $N_{\mathrm{D,w},Q_{\mathrm{ARP}}}$ for an NE 2571 chamber using the TRS-398 k_Q values, the Muir and Rogers Monte Carlo k_Q values or an ARPANSA direct calibration. The final two columns show the expected shift in $N_{\mathrm{D,w},Q_{\mathrm{ARP}}}$ with a direct calibration compared to using the TRS-398 or Muir and Rogers k_Q values.

Nominal beam energy	$\mathrm{TPR}_{20,10}$	$N_{\mathrm{D,w},Q_{\mathrm{ARP}}}$ TRS-398 (mGy/nC)	$N_{\mathrm{D,w},Q_{\mathrm{ARP}}}$ Muir and Rogers (mGy/nC)	$N_{\mathrm{D,w},Q_{\mathrm{ARP}}}$ direct (mGy/nC)	Ratio of $N_{\mathrm{D,w}}$ values ARPANSA/ TRS-398	Ratio of $N_{\mathrm{D,w}}$ values ARPANSA/Muir and Rogers
^{60}Co	-	45.89	45.89	45.89	1.000	1.000
6 MV	0.673	45.59	45.50	45.41	0.996	0.998
10 MV	0.734	45.29	45.07	44.84	0.990	0.995
18 MV	0.777	44.79	44.48	44.30	0.989	0.996

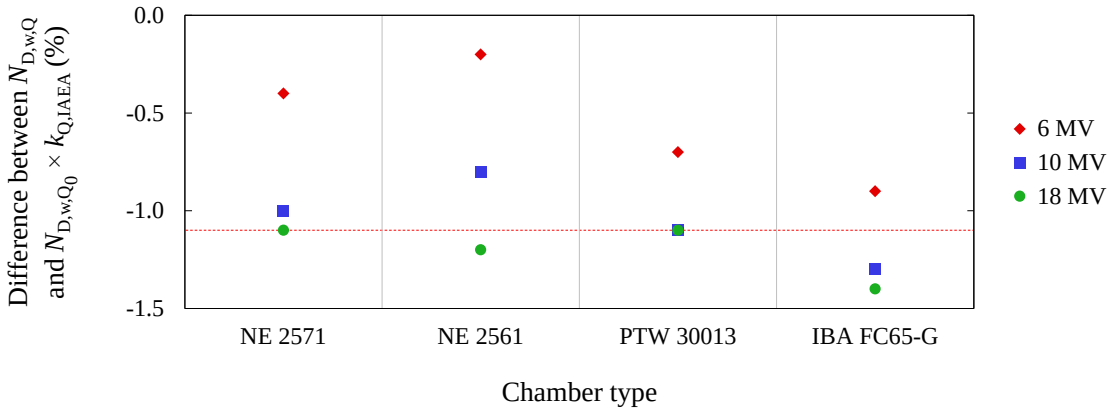

Figure 6-3: Differences in $N_{D,w}$ between an ARPANSA direct megavoltage calibration and a ^{60}Co calibration used with the IAEA k_Q values for four common chamber types. The dashed red line shows one relative standard uncertainty in $N_{D,w,Q_0} \times k_{Q,IAEA}$.

to those in the TG-51 protocol addendum (McEwen *et al.*, 2014) and not the original TG-51 protocol (Almond *et al.*, 1999). The expected shifts for the IAEA k_Q values and AAPM k_Q values are also shown graphically in Figures 6-3 and Figure 6-4 respectively. In each of the figures a dotted line shows the relative standard uncertainty in the $N_{D,w,Q}$ of the comparison method.

When comparing to the current Australian practice of using IAEA k_Q values, the shifts are quite spread across both chamber types and beam energies. At 6 MV none of the chambers shift beyond the 1σ uncertainty in the current method. For all chambers the shifts will be greater at the 10 MV and 18 MV beam qualities and for two chambers shifts greater than the current 1σ uncertainty of 1.1% can be expected.

Table 6-2: The first three results tabulate the differences in $N_{D,w}$ between a direct megavoltage calibration and a ^{60}Co calibration used in conjunction with the k_Q values listed in the IAEA TRS-398 Code of Practice. The second three results show the same comparison for the k_Q values calculated using the formula from the AAPM TG-51 protocol addendum. These are the changes in $N_{D,w}$ that can be expected when transitioning to a direct megavoltage calibration provided by ARPANSA.

Chamber type	**Shift in $N_{D,w}$ compared to current Australian practice (%)**			**Shift in $N_{D,w}$ compared to Muir and Rogers (2010) (%)**		
	6 MV	**10 MV**	**18 MV**	**6 MV**	**10 MV**	**18 MV**
NE 2571	-0.4	-1.0	-1.1	-0.2	-0.4	-0.4
NE 2561	-0.2	-0.8	-1.2	0.0	-0.2	-0.3
PTW 30013	-0.7	-1.1	-1.1	-0.7	-1.1	-1.0
IBA FC65-G	-0.9	-1.3	-1.4	-0.6	-0.9	-0.8

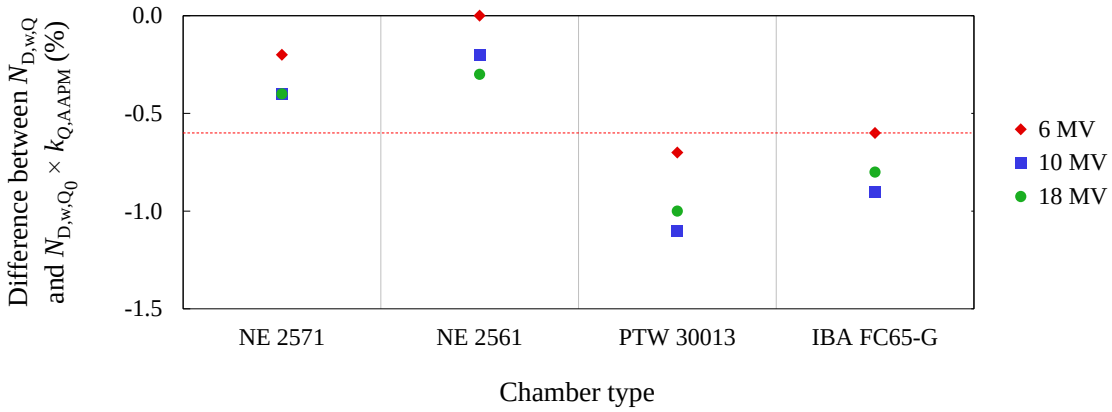

Figure 6-4: Differences in $N_{D,w}$ between an ARPANSA direct megavoltage calibration and a ^{60}Co calibration with the AAPM k_Q values for four common chamber types. The dashed red line shows one relative standard uncertainty in $N_{D,w,Q_0} \times k_{Q,AAPM}$.

In the comparison between the proposed direct ARPANSA method and the use of the AAPM k_Q with an ARPANSA ^{60}Co calibration, a difference between the original graphite and newer waterproof chambers can be seen. For the graphite chambers the shifts expected are less than the 1σ uncertainty in $N_{D,w,Q_0} \times k_{Q,AAPM}$ of 0.6%. In contrast, for the waterproof chambers all shifts are expected to be at the 1σ uncertainty limit or beyond. This is an alternate way of considering the k_Q data presented in Figures 5-9 and 5-10 for the two waterproof chambers. With the limited amount of measured k_Q data available for these chamber types it is difficult to determine whether the ARPANSA k_Q values are low or the modelled k_Q values of TG-51 are high. This highlights the need for more measured k_Q values for waterproof chambers. The difference between the two methods for evaluating the calibration coefficient at user energies for waterproof chambers is an area that requires further investigation.

6.4 Further work

As with any research project, there is always more work that can be done. Two significant extensions are planned on the work that has already been completed. The first is to establish an ionisation chamber model and the second is to extend this work into smaller field sizes.

6.4.1 Ionisation chamber modelling

Modelling an ionisation chamber at many depths along the central beam axis in a water phantom will enable the linac model to be directly compared to the PDI measured with an

ionisation chamber. A validated chamber model will remove the requirement to convert the measured PDI to a depth dose curve which will reduce the uncertainty in the linac model. In addition, the ability to model ionisation chambers will allow k_Q values to be modelled for a variety of ionisation chambers in the ARPANSA linac beams. The observed difference between the ARPANSA k_Q values and other modelled k_Q values for waterproof ionisation chambers is an important result that requires further investigation. With models of the PTW 30013 and the IBA FC65-G chambers the k_Q values can be modelled in the ARPANSA linac beams to explore possible causes for the observed discrepancies.

6.4.2 Small fields

The second planned project is the extension of the linac model to more field sizes, especially small fields defined by the multi-leaf collimator and cones. Currently calibrations are available only for large (10×10 cm^2) reference fields. Farmer-type chambers are suitable for measuring the dose in fields down to 4×4 cm^2, but this is still a relatively large field size. Small fields down to less than 1 cm are widely used for radiotherapy treatments for intensity-modulated radiation therapy (IMRT) and increasingly for stereotactic ablative radiotherapy treatments (Lagerwaard *et al.*, 2012). Small field treatments can be delivered using regular linacs or specialised equipment such as CyberKnife (Accuray Incorporated, 2015a), TomoTherapy (Accuray Incorporated, 2015b). Small fields introduce many complexities in the measurement of dose. Detector size and volume averaging effects mean that Farmer-type chambers usually used for reference dosimetry are not suitable for these fields, and even detectors designed for small fields are problematic.

Source occlusion caused by overlapping beam penumbra cause the field intensity to be peaked on the central axis so there is no uniform region to measure the dose. The lack of lateral electronic equilibrium and loss of scattered radiation increases the average energy of the beam compared to the reference conditions. Many clinics use a ‘daisy-chain’ technique (Dieterich and Sherouse, 2011) where a relative dosemeter, such as a small volume ionisation chamber, diode or diamond detector, is cross-calibrated against a Farmer-type chamber in an intermediate field where the response of both detectors is acceptable. The cross-calibrated chamber is then used at smaller field sizes where the Farmer-type chamber is too large. It is ARPANSA’s goal to extend the calibration services offered to include smaller field sizes, and modelling of the small fields is a critical step in this process.

CHAPTER 7 CONCLUSIONS

The Monte Carlo method described in this thesis is a conceptually simple method to convert absorbed dose to graphite to absorbed dose to water. The work presented can be split up into four broad categories: modelling (including validation steps), complete method validation, uncertainty analysis and assessment of the clinical impact of the work.

The modelling component of this work occurred in two distinct stages. The first stage was the establishment of a model for the ARPANSA linac beam. The linac model has been thoroughly validated by comparison of modelled dose distributions with measured data in two media: water and graphite. The second stage of the project was the modelling of the calorimeter and water phantom for the Monte Carlo conversion ratio.

The primary method of validation for the method is the comparison with the international reference laboratory, the BIPM, through the key comparison BIPM.RI(I)-K6. The ARPANSA determination of absorbed dose to water was lower than that of the BIPM by 0.35%, 0.76% and 0.68% at the beam energies of 6 MV, 10 MV and 18 MV respectively. The comparison result at 6 MV was within 1σ and at 10 MV and 18 MV was within 2σ of the BIPM value. When compared to the average of all comparison participants the ARPANSA result differed by -0.20%, -0.57% and -0.26% at the three respective beam energies. All results were within 1σ of the participant average. Additional indirect comparisons were performed with the Japanese and Canadian primary standards laboratories, NMIJ and NRC. The trend of good agreement at 6 MV and reasonable agreement at 10 MV and 18 MV continued with the two indirect comparisons. Finally, further validation comes from excellent agreement with cavity ionisation theory.

This thesis has presented a rigorous approach to determine the uncertainty in the Monte Carlo method via comparison to measured PDDs. The details of the uncertainty budget for an absorbed dose to water measurement at the beam qualities of ^{60}Co or high energy accelerator photon beams has not previously been published by any standards laboratory. Despite the inability to compare details of the uncertainty analysis method the uncertainty values for the Monte Carlo conversion factor and the resulting ionisation chamber calibration coefficient compare favourably to other similar methods.

The uncertainties achieved with the direct calibration method of 0.6 to 0.7%, are significantly less than those in current use with a reference beam quality of ^{60}Co and the TRS-398 energy correction. This is of benefit to the clinical users with increasing interest being placed on the accuracy of radiotherapy treatments.

Lastly, the calibration coefficients determined by the direct calibration method have been compared to those obtained by ^{60}Co calibration and an energy correction to the user beam quality. It is expected that the change to the direct calibration method will result in a shift in the calibration coefficient of clinical reference chambers. The expected shift depends on the beam quality and chamber type. The analysis was performed for four common clinical reference chambers: the NE 2571, NE 2561, PTW 30013 and the IBA FC65-G. The calibration coefficient is expected to reduce for all chamber types in the range of 0.2-0.9% for the 6 MV beam, 0.8-1.3% for the 10 MV beam and 1.1-1.4% for the 18 MV beam. The reduction in calibration coefficients will cause a reduction in the dose calibration of linacs and clinics must bear this in mind when changing to the direct calibration service.

APPENDIX A PUBLICATIONS ARISING FROM THIS WORK

The following publications resulted from the work presented in this thesis.

Peer reviewed publications:

Wright T, Lye J E, Ramanathan G, Harty P D, Oliver C, Webb D V and Butler D J 2015 Direct calibration in megavoltage photon beams using Monte Carlo conversion factor: validation and clinical implications *Phys. Med. Biol.* **60** 883-904
(Reproduced in Appendix D)

Picard S, Burns D T, Roger P, Harty P D, Ramanathan G, Lye J E, Wright T, Butler D J, Cole A, Oliver C and Webb D V 2014 Key comparison BIPM.RI(I)-K6 of the standards for absorbed dose to water of the ARPANSA, Australia and the BIPM in accelerator photon beams *Metrologia* **51** 06006

Shimizu M, Morishita Y, Kato M, Tanaka T, Kurosawa T, Takata N, Saito N, Ramanathan G, Harty P, Oliver C, Wright T and Butler D 2015 Comparison of the NMIJ and the ARPANSA standards for absorbed dose to water in high-energy photon beams *Radiat. Prot. Dosim.* **164** 181-6

Butler D, Ramanathan G, Oliver C, Cole A, Lye J, Harty P, Wright T, Webb D and Followill D 2014 Direct megavoltage photon calibration service in Australia *Australas. Phys. Eng. Sci. Med.* **37** 753-61

Reports:

Ramanathan G, Harty P, Wright T, Lye J, Butler D, Webb D and Huntley R 2014 The Australian Primary Standard for absorbed dose to water (graphite calorimeter). In: *Technical Report No. 166,* (Yallambie: Australian Radiation Protection and Nuclear Safety Agency)

Conference presentations/posters:

Wright T, Lye J, Butler D, Ramanathan G, Harty P, Oliver C, Cole A and Webb D 2013 Validating a Monte Carlo linac model: how good is good? (presentation, EPSM-ABEC, Perth)

Wright T, Lye J and Butler D 2013 Uncertainties in a Monte Carlo linac model – validation for primary standard accuracy (poster, ICCR, Melbourne)

Wright T, Lye J and Webb D 2012 Commissioning the Elekta MCLi and MLCi2 leaf designs using BEAMnrc (poster, EPSM, Gold Coast)

APPENDIX B COMPLETE SET OF MATCHING PROFILES

The figures in this appendix show the comparison of measured beam profiles and modelled dose distributions in a water phantom for the 6 MV, 10 MV and 18 MV beams. The profiles are shown at depths of d_{max}, 5 cm, 10 cm and 20 cm for 10×10 cm^2 and 30×30 cm^2 field sizes.

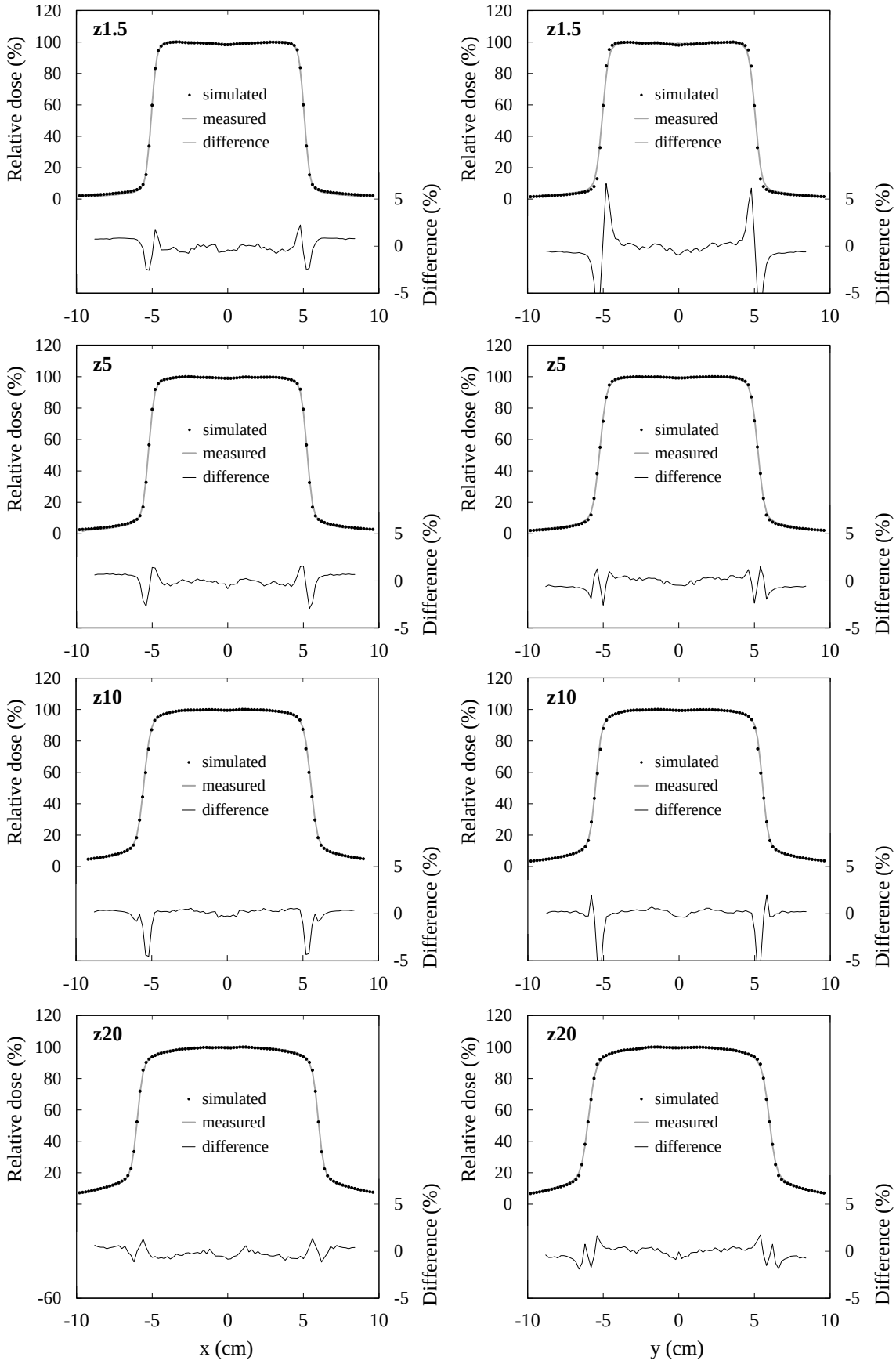

Figure B-1: Comparison of measured and modelled profiles in water for the 6 MV beam at depths of 1.5 cm (d_{max}), 5 cm, 10 cm and 20 cm for a 10×10 cm^2 field. The differences between measured and modelled profiles relative to the central axis dose are shown underneath each profile.

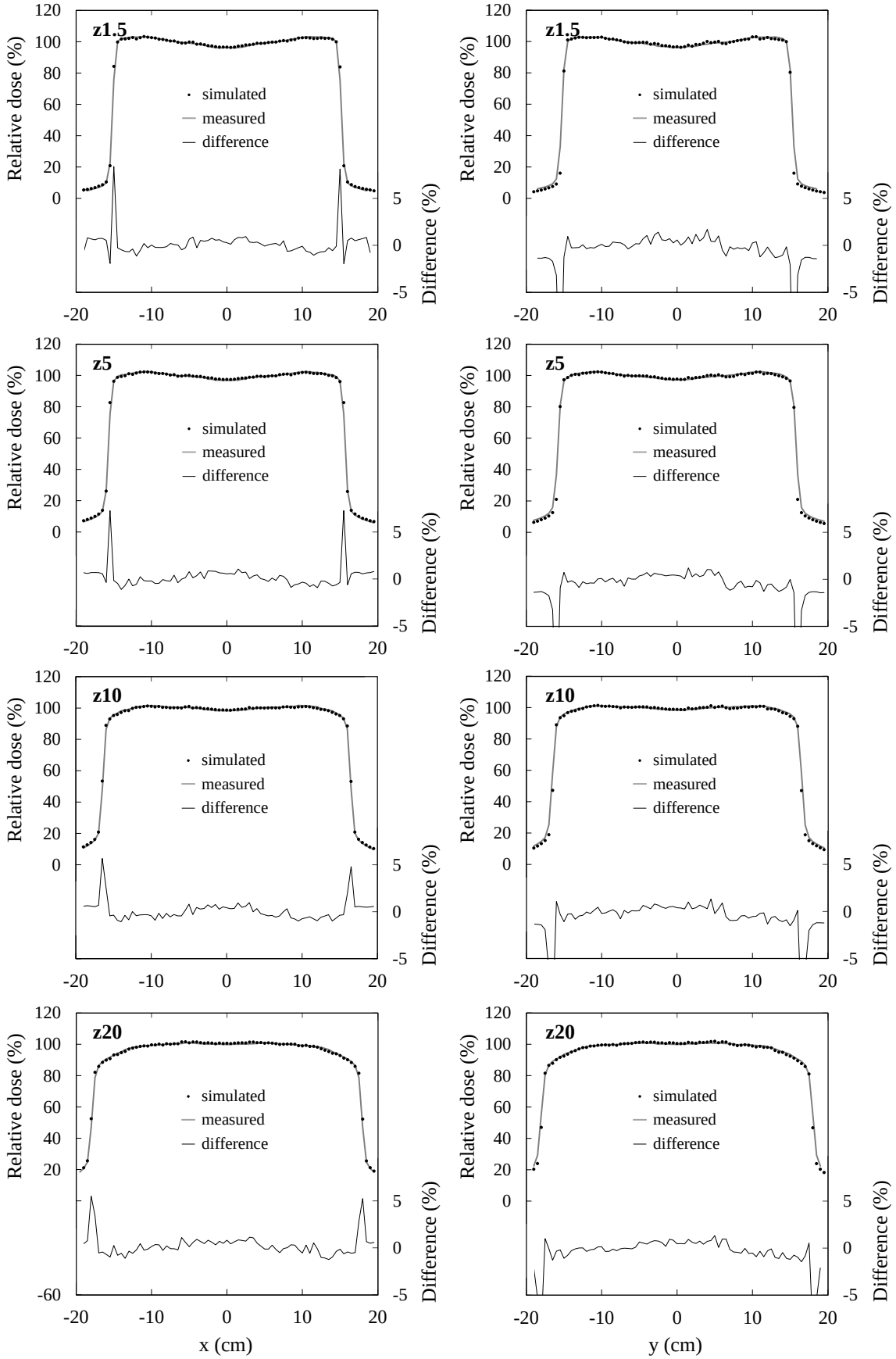

Figure B-2: Comparison of measured and modelled profiles in water for the 6 MV beam at depths of 1.5 cm (d_{max}), 5 cm, 10 cm and 20 cm for a 30×30 cm^2 field. The differences between measured and modelled profiles relative to the central axis dose are shown underneath each profile.

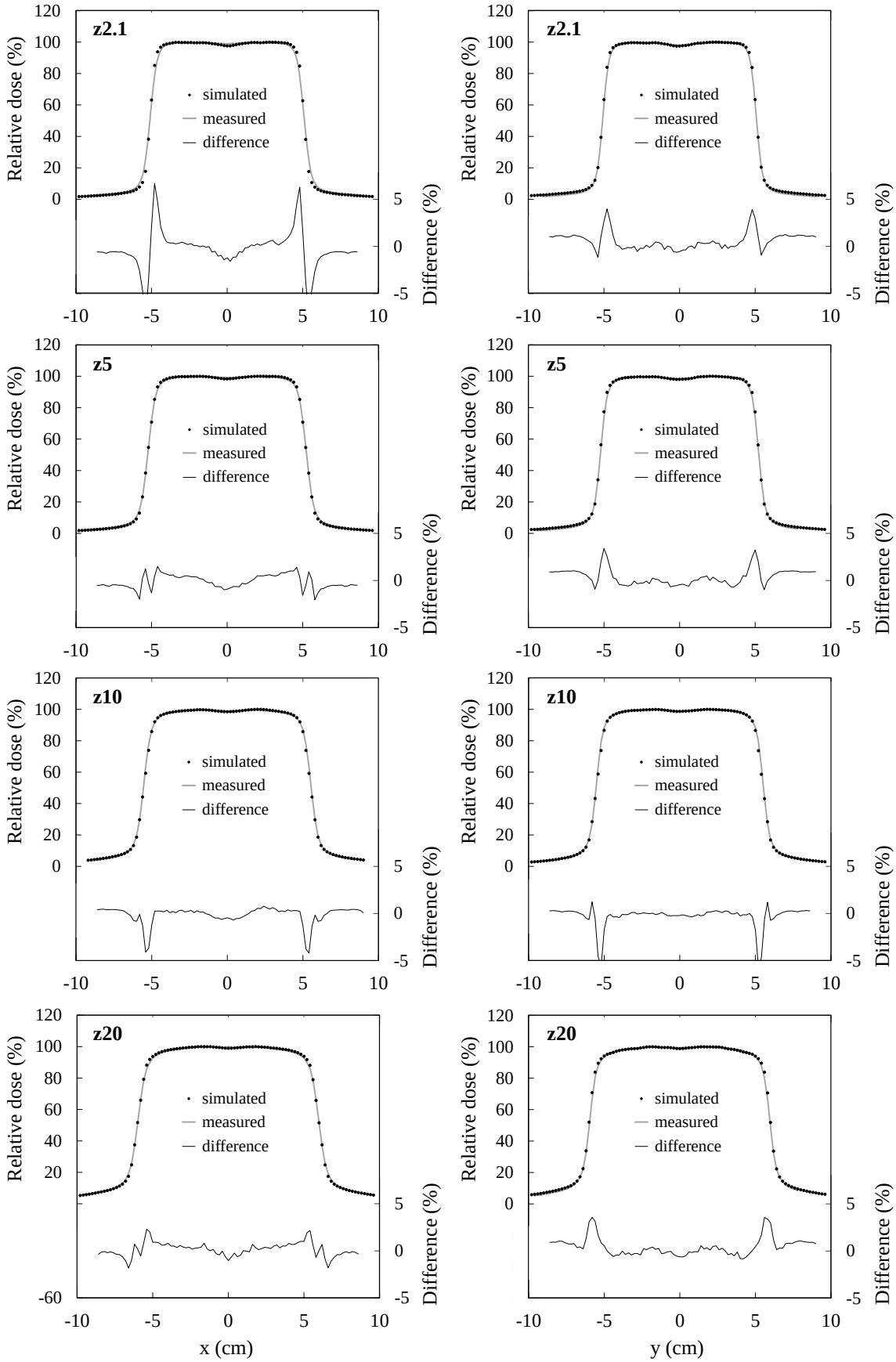

Figure B-3: Comparison of measured and modelled profiles in water for the 10 MV beam at depths of 2.1 cm (d_{max}), 5 cm, 10 cm and 20 cm for a 10×10 cm^2 field. The differences between measured and modelled profiles relative to the central axis dose are shown underneath each profile.

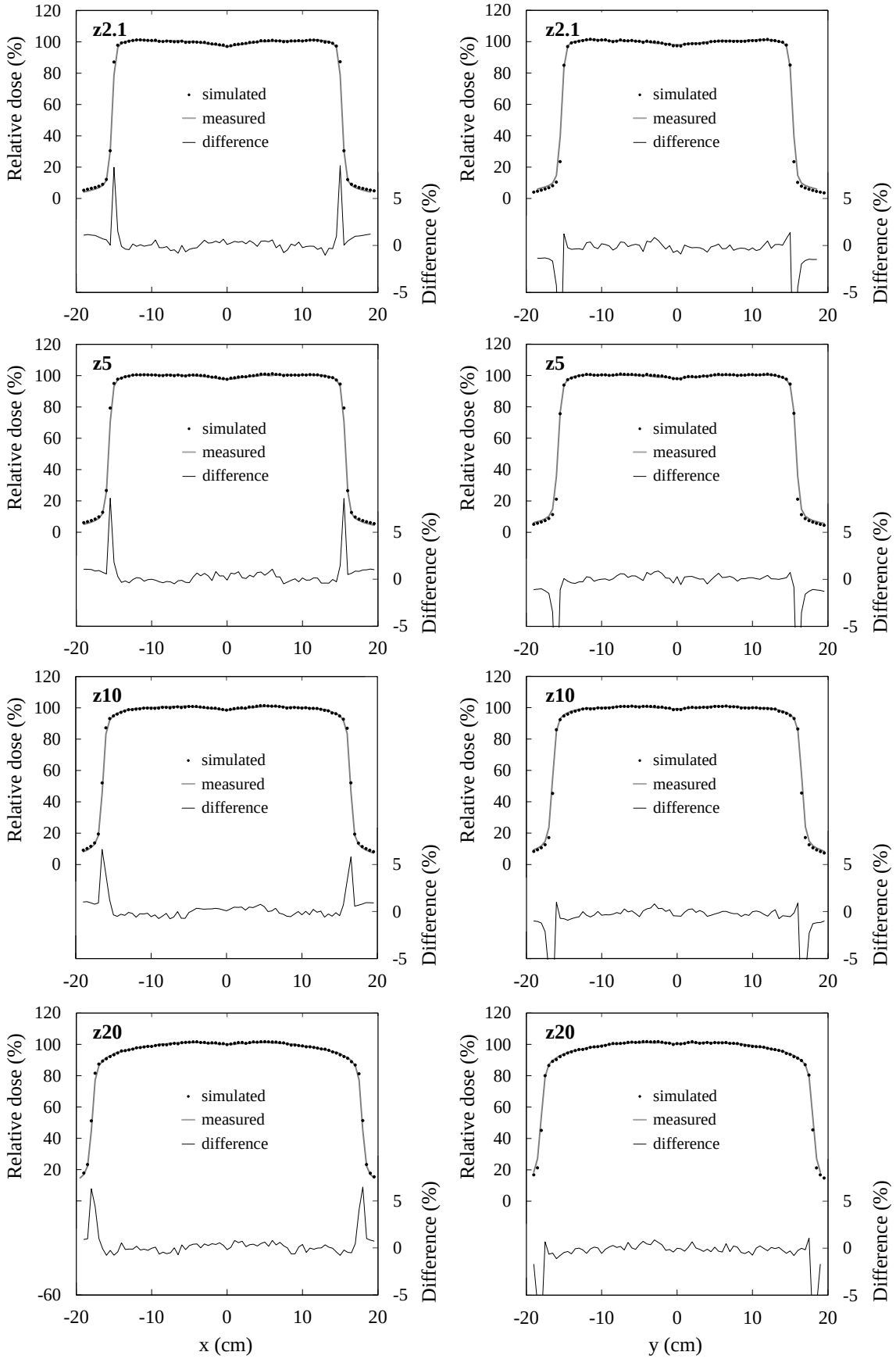

Figure B-4: Comparison of measured and modelled profiles in water for the 10 MV beam at depths of 2.1 cm (d_{max}), 5 cm, 10 cm and 20 cm for a 30×30 cm^2 field. The differences between measured and modelled profiles relative to the central axis dose are shown underneath each profile.

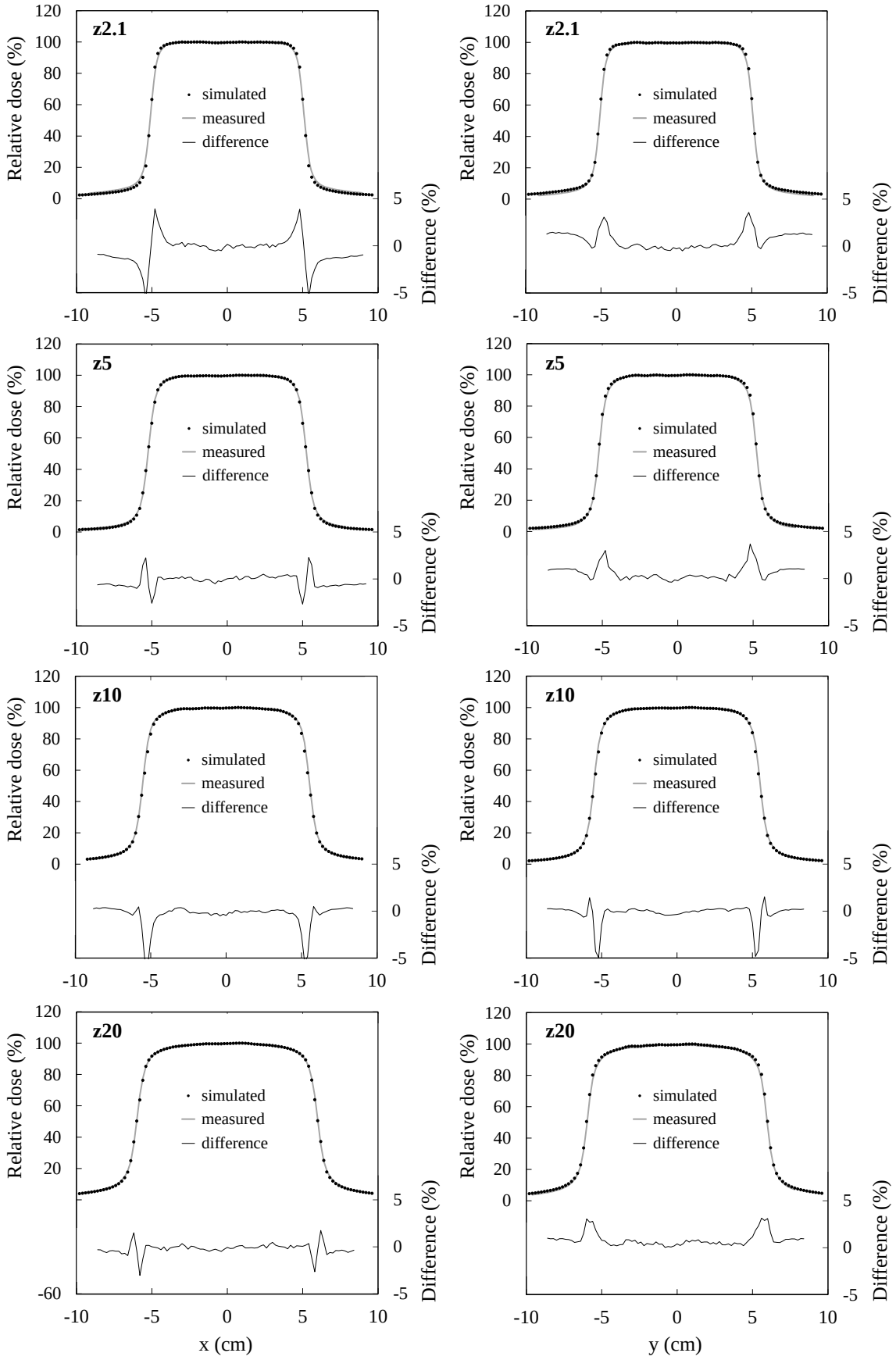

Figure B-5: Comparison of measured and modelled profiles in water for the18 MV beam at depths of 2.1 cm (d_{max}), 5 cm, 10 cm and 20 cm for a 10×10 cm2 field. The differences between measured and modelled profiles relative to the central axis dose are shown underneath each profile.

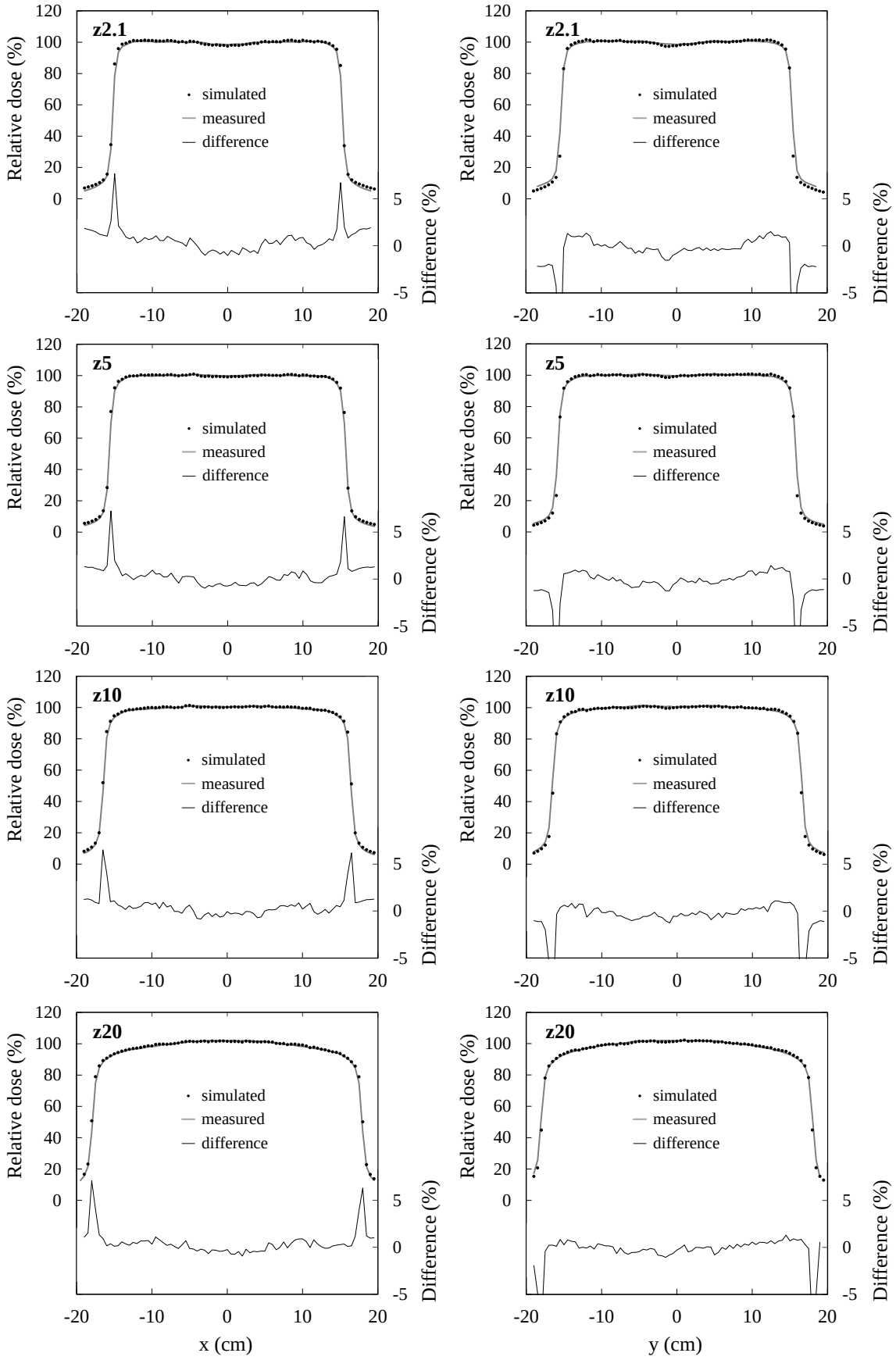

Figure B-6: Comparison of measured and modelled profiles in water for the18 MV beam at depths of 2.1 cm (d_{max}), 5 cm, 10 cm and 20 cm for a 30×30 cm^2 field. The differences between measured and modelled profiles relative to the central axis dose are shown underneath each profile.

APPENDIX C COMPLETE UNCERTAINTY TABLES FOR 10 MV AND 18 MV BEAMS

Table C-1: Uncertainties in calorimeter geometry and resulting uncertainty in the dose to the core, D_g at 10 MV.

Uncertainty contribution	Value	Standard uncertainty (k = 1)	Comment on uncertainty	Sensitivity	Comment on sensitivity	Standard uncertainty in D_g (%)
Density of plates	1.79 g/cm^3	0.49 %		0.19% (change in relative dose at reference depth) per 1% increase in density	Assessed by MC density analysis	0.09
Density of calorimeter	1.79 g/cm^3	3%	variation in the manufacturer specifications	0.025% Calculated by 0.16% (change in relative dose at reference depth) per 1% increase in density × ratio of calorimeter-only depth to total reference depth (0.48/5.48)	Assessed by MC density analysis	0.05
Calorimeter vacuum gaps	0.19 cm	10%	0.02 cm, estimated from design specs and radiographs	2% per cm	Assessed by MC gap correction scaled by ratio of gap uncertainty:gap used to calculate correction	0.04
Plate air gaps	0.2 cm	25%	estimated from radiographs	2% per cm	Inverse square law	0.10
Core mass	1.5622 g	0.01%		1	1:1	0.01
Combined uncertainty in D_g due to calorimeter geometry						*0.15*

Table C-2: Uncertainties in calorimeter geometry and resulting uncertainty in the dose to the core, D_g at 18 MV.

Uncertainty contribution	Value	Standard uncertainty (k = 1)	Comment on uncertainty	Sensitivity	Comment on sensitivity	Standard uncertainty in D_g (%)
Density of plates	1.79 g/cm^3	0.49 %		0.15% (change in relative dose at reference depth) per 1% increase in density	Assessed by MC density analysis	0.07
Density of calorimeter	1.79 g/cm^3	3%	variation in the manufacturer specifications	0.025% Calculated by 0.13% (change in relative dose at reference depth) per 1% increase in density × ratio of calorimeter-only depth to total reference depth (0.48/5.48)	Assessed by MC density analysis	0.04
Calorimeter vacuum gaps	0.19 cm	10%	0.02 cm, estimated from design specs and radiographs	1.5% per cm	Assessed by MC gap correction scaled by ratio of gap uncertainty:gap used to calculate correction	0.03
Plate air gaps	0.2 cm	25%	estimated from radiographs	2% per cm	Inverse square law	0.10
Core mass	1.5622 g	0.01%		1	1:1	0.01
Combined uncertainty in D_g due to calorimeter geometry						*0.13*

Table C-3: Uncertainties in the Monte Carlo model of the linac beam and resulting uncertainty in the conversion ratio, $[D_w/D_g]_{MC}$, for the 10 MV beam. The first section relates how an imperfect match between the measured and modelled PDDs affects the dose conversion ratio and is obtained from the difference between the measured and modelled PDDs (see Figures 3-3 and 3-6). The second section combines the contributions of the uncertainty in the measured PDD. The uncertainties due to modelling and measurement are then combined to give the uncertainty in the model representation of the real beam.

Uncertainty contribution	**Material**	**Value**	**Standard uncertainty (k = 1)**	**Comment on uncertainty**	**Sensitivity**	**Comment on sensitivity**	**Standard uncertainty in $[D_w/D_g]_{MC}$ (%)**
Uncertainty in the match between the modelled and measured beams							
Gradient, *m*, of the relative difference between measured and modelled PDDs	graphite	4.1×10^{-4} cm^{-1}	4.1×10^{-4} cm^{-1}	Difference gradients from Figs 3-3 and 3-6	4.5×10^{2} %.cm	Sensitivity of dose at the reference depth to a change in the residual gradient **(C)**	0.19
	water	-2.3×10^{-4} cm^{-1}	2.3×10^{-4} cm^{-1}		6.7×10^{2} %.cm		0.15
Combined uncertainty in the match between the modelled and measured beams							*0.24*
Uncertainty in the PDD measurement							
Density	graphite	1.79 g/cm^3	0.49%		0.19% (change in relative dose at reference depth) per 1% increase in density	Assessed by MC density analysis	0.09
	water	0.99821 g/cm^3	0.05%	±4 °C	0.21% (change in relative dose at reference depth) per 1% increase in density	Assessed by MC density analysis	0.01
EPOM	graphite	2.32 mm	Uncertainty in dose (>d_{max}) estimated directly from Tessier and Kawrakow (2010), see Section 3.3.1				0.1
	water	1.8 mm					0.1
Stopping powers	graphite water	Included in the uncertainty in EPOM					
Relative positioning of chamber	graphite	Variable	0.025 cm		-5.7% per cm	Gradient of PDD at reference depth **(D)**	0.14
	water	Variable	0.025 cm		-4.48% per cm		0.11
Combined uncertainty in the PDD measurement							*0.25*
Combined uncertainty in $[D_w/D_g]_{MC}$ due to the model representation of the real beam							*0.35*

Table C-4: Uncertainties in the Monte Carlo model of the linac beam and resulting uncertainty in the conversion ratio, $[D_w/D_g]_{MC}$, for the 18 MV beam. The first section relates how an imperfect match between the measured and modelled PDDs affects the dose conversion ratio and is obtained from the difference between the measured and modelled PDDs (see Figures 3-3 and 3-6). The second section combines the contributions of the uncertainty in the measured PDD. The uncertainties due to modelling and measurement are then combined to give the uncertainty in the model representation of the real beam.

Uncertainty contribution	**Material**	**Value**	**Standard uncertainty (k = 1)**	**Comment on uncertainty**	**Sensitivity**	**Comment on sensitivity**	**Standard uncertainty in $[D_w/D_g]_{MC}$ (%)**
Uncertainty in the match between the modelled and measured beams							
Gradient, *m*, of the relative difference between measured and modelled PDDs	graphite	5.2×10^{-4} cm^{-1}	5.2×10^{-4} cm^{-1}	Difference gradients from Figs 3-3 and 3-6	3.1×10^{2} %.cm	Sensitivity of dose at the reference depth to a change in the residual gradient **(C)**	0.16
	water	1.7×10^{-4} cm^{-1}	1.7×10^{-4} cm^{-1}		7.6×10^{2} %.cm		0.13
Combined uncertainty in the match between the modelled and measured beams							*0.21*
Uncertainty in the PDD measurement							
Density	graphite	1.79 g/cm^3	0.49%		0.15% (change in relative dose at reference depth) per 1% increase in density	Assessed by MC density analysis	0.07
	water	0.99821 g/cm^3	0.05%	±4 °C	0.18% (change in relative dose at reference depth) per 1% increase in density	Assessed by MC density analysis	0.01
EPOM	graphite	2.27 mm	Uncertainty in dose (>d_{max}) estimated directly from Tessier and Kawrakow (2010), see Section 3.3.1				0.1
	water	1.8 mm					0.1
Stopping powers	graphite water	Included in the uncertainty in EPOM					
Relative positioning of chamber	graphite	Variable	0.025 cm		-5.04% per cm	Gradient of PDD at reference depth **(D)**	0.13
	water	Variable	0.025 cm		-4.4% per cm		0.11
Combined uncertainty in the PDD measurement							*0.23*
Combined uncertainty in $[D_w/D_g]_{MC}$ due to the model representation of the real beam							*0.31*

APPENDIX D REPRODUCTION OF PEER-REVIEWED PUBLICATION

The primary peer-reviewed publication resulting from this work is reproduced in this appendix.

Wright, T., Lye, J.E., Ramanathan, G., Harty, P.D., Oliver, C., Webb, D.V. & Butler, D.J. (2015). Direct calibration in megavoltage photon beams using Monte Carlo conversion factor: validation and clinical implications.
Physics in Medicine and Biology 60(2), 883-904.

APPENDIX E GLOSSARY OF TERMS

^{60}Co: A radioactive source with two high energy gamma emissions. Historically ^{60}Co was used in many radiotherapy treatment machines and it remains an important reference beam quality for the calibration of medical *linacs*.

Absorbed dose: Defined as the energy imparted by ionising radiation per unit mass in a medium. The absorbed dose is the energy absorbed as a result of many interactions between the medium and an electron set in motion by a *kerma* interaction. The SI unit of absorbed dose is the gray (Gy). One Gy is equal to one joule per kilogram.

Absorbed dose to water: The *absorbed dose* where the medium is water.

Air kerma: The *kerma* in air.

BEAMnrc: A user code of *EGSnrc* with the primary purpose of modelling radiotherapy sources.

Bureau International des Poids et Mesures (BIPM): An international standards laboratory whose mandate is to promote and facilitate world-wide traceability of measurement quantities.

Calibration coefficient, $N_{D,w}$: A multiplicative factor to convert the charge measured by an *ionisation chamber* to *absorbed dose to water*.

Calorimeter: A device capable of precise temperature measurement.

Calorimetry: The measurement of heat exchanged using a *calorimeter*. In radiation measurement, calorimetry is used to measure the heat absorbed by the *calorimeter* during irradiation.

Component module: A pre-defined geometry within *BEAMnrc* that is customised by entering values for the available geometry parameters that determine the size, shape and material of the component module.

Coverage factor, k: The coverage factor specifies the confidence with which an uncertainty is quoted. For a coverage factor of $k = 1$ the measured value should be within 68% of the real value. At $k = 2$ the measured value should be within 95% of the real value.

Cross-line: A measurement direction at a fixed distance in a *linac* beam that indicates the direction perpendicular to a line drawn between the electron gun and the target in the *linac* head, shown by the dash-dotted line below.

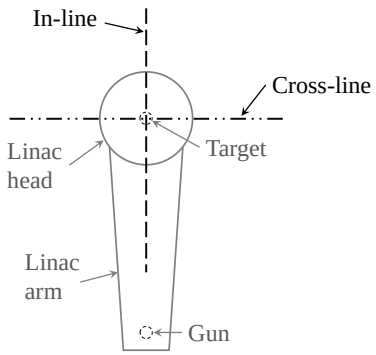

d_{max}: The depth in a *phantom* where the dose maximum occurs.

Dosemeter: An instrument or device used to measure dose.

DOSXYZnrc: A user code of *EGSnrc* for the calculation of dose deposition in a rectilinear voxel phantom.

Effective point of measurement (EPOM): A point within an ion chamber that usually lies upstream of the centre of the chamber. A measurement with an ion chamber is considered to be made at the EPOM rather than the centre of the chamber in order to correct for the displacement of phantom material (usually water) by the air cavity of the chamber.

EGSnrc: A *Monte Carlo* code designed to model coupled electron and photon interactions in the energy range of a few keV to hundreds of GeV. EGSnrc can be used as directly or through user codes that are designed for specific applications.

Energy correction factor, k_Q: A factor to correct for the difference in the response of an *ionisation chamber* between the calibration beam quality and the measurement beam quality.

Estimated standard deviation of the mean (ESDM): The ESDM is a common method of quantifying the uncertainty in a measurement. It estimates the standard deviation of the averages of many sets of measurements. The ESDM is calculated as $\sigma/\sqrt{n}$.

Field instrument: An instrument that is cross-calibrated periodically in the clinical beam against a *reference instrument* and then used for routine measurements. The requirements for a field instrument are less stringent than those for a *reference instrument*.

Global difference: The difference between two values relative to a single point in the measurement series (for example, the difference relative to the maximum dose in a *PDD* or to the dose on the central axis in a *profile*).

In-line: A measurement direction at a fixed distance in a *linac* beam that indicates the direction parallel to a line drawn between the electron gun and the target in the *linac* head, shown by the dashed line (see *cross-line*).

Ionisation chamber: An instrument that collects the charge created by radiation interactions in an air cavity. The charge collected is then related to *absorbed dose* or *air kerma* by applying a *calibration coefficient*.

Kerma: The Kinetic Energy Released per unit MAss, or the energy transferred to a charged particle in a medium in an interaction between the charged particle and a photon. The SI unit of kerma is the gray (Gy). One Gy is equal to one joule per kilogram.

Key comparison: A metrological comparison for which the *BIPM* provides the comparison reference value through participation in the comparison.

Key comparison database (KCDB): An online searchable database that records the results of *key and supplementary comparisons* and subsequent calibration and measurement capabilities (CMCs) that are recognised through a mutual recognition arrangement by participating countries.

Linear accelerator (linac): A commonly-used machine for external beam radiotherapy. A beam of Bremsstrahlung photons is created by accelerating electrons toward a metal target and the beam is flattened and shaped by collimators, filters and beam shaping devices within the linac head. The linac head is held on an arm that rotates around the patient to deliver the treatment isocentrically.

Local difference: The difference between two values relative to the value at the point of comparison in the measurement series. The difference between the local difference and *global difference* in high dose areas is usually minimal, but in low dose areas the difference is usually significant.

Monte Carlo: Monte Carlo is a simulation method that relies on statistical power by utilising many repeats of the simulation to determine the expected outcome. In radiotherapy simulations one outcome that is often sought is a dose calculation where the accuracy of the calculated dose increases as the number of histories increases.

National Measurement Institute (NMI): A laboratory that maintains measurement standards and disseminates those standards nationally.

Percentage depth dose (PDD): A plot of doses measured at many depths in a homogenous *phantom* with each dose normalised to one of the measurements. The normalisation point is commonly chosen to be d_{max} or a depth that is important in the measurement, such as the reference depth.

Phantom: A block of material in which measurements of dose are made when the phantom is irradiated. Water and water-equivalent plastic are both common phantom materials.

Phase space file: A file that contains information about the energy and particle type, and the position and direction coordinates of every particle that has reached the phase space plane at the end of a simulation.

Primary standard: A standard obtained with high accuracy and precision by a measurement of only fundamental physical quantities.

Profile: A series of dose measurements across the radiation beam through the central axis. Profiles can be in the *in-line* or cross-*line* directions.

Recombination: Refers to the process where ions within an ion chamber combine to form a stable atom before they reach the collecting electrodes.

Reference class instrument: *Ion chambers* with the required accuracy, precision and stability to provide the traceability link between the *primary standards* laboratory and a clinical *linac* output.

Reference position: The position (depth) at which an *ion chamber* is placed during a calibration. In *calorimetry* the sensitive part of the *calorimeter* is placed at the reference position which is converted from units of cm to g/cm^2.

Relative standard uncertainty: The uncertainty in a measurement that is calculated as the estimated standard deviation of the measurement and expressed as a percentage of the value.

Scoring: In a *Monte Carlo* simulation, scoring refers to the recording of the integrated dose in a defined volume due to interactions in the simulation. For each interaction in the defined volume the dose deposited is added to the doses previously deposited in the same volume. At the end of the simulation the integrated dose that has been scored is reported in an output file.

Specific heat capacity: The amount of energy required to increase the temperature of one gram of a material by one degree Celsius.

Supplementary comparison: A metrological comparison that does not include the *BIPM* as a participant where the BIPM comparison reference value is provided by a linking laboratory that has previously participated in a *key comparison* for the same quantity.

Tissue phantom ratio ($TPR_{20,10}$): A beam quality indicator that is calculated as the ratio of doses at a distance of 100 cm from the source at depths of 20 cm (D_{20}) and 10 cm (D_{10}), D_{20}/D_{10}.

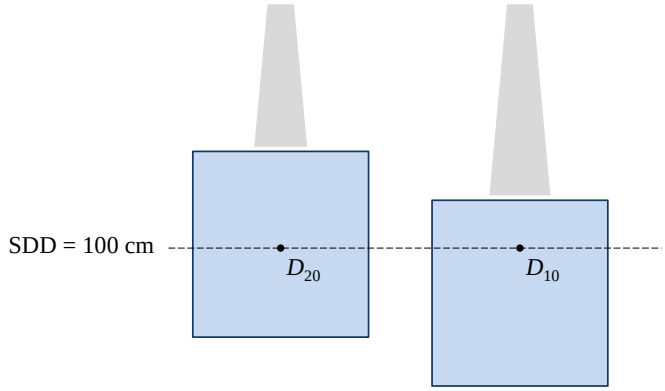

REFERENCES

Aalbers A H L, Hoornaert M-T, Minken A, Palmans H, Pieksma M W H, de Prez L A, Reynaert N, Vynckier S and Wittkamper F W 2008 (rev. 2012) Code of Practice for the Absorbed Dose Determination in High Energy Photon and Electron Beams. In: *Report 18*, (Delft: Netherlands Commission on Radiation Dosimetry)

Absorbed Dose Working Group 2013 Calorimetric comparison of absorbed dose to water at high energies. BIPM key comparison BIPM.RI(I)-K6. Protocol 1.7. (Sevres: Bureau International des Poids et Mesures)

Accuray Incorporated 2015a What is the CyberKnife system? (available at http://www.cyberknife.com/, accessed 13 June 2015)

Accuray Incorporated 2015b Why TomoTherapy®? (available at http://www.tomotherapy.com/whytomo/, accessed 13 June 2015)

Ali E S 2012 Accurate unfolding of photon spectra of clinical linear accelerators using transmission measurements. (Doctoral dissertation, Ottawa: Carleton University)

Ali E S M, McEwen M R and Rogers D W O 2012 Detailed high-accuracy megavoltage transmission measurements: A sensitive experimental benchmark of EGSnrc *Med. Phys.* **39** 5990-6003

Allisy-Roberts P J and Burns D T 2005 Summary of the BIPM.RI(I)-K4 comparison for absorbed dose to water in ^{60}Co gamma radiation *Metrologia* **42** 06002

Almond P R, Biggs P J, Coursey B, Hanson W, Huq M S, Nath R and Rogers D 1999 AAPM's TG-51 protocol for clinical reference dosimetry of high-energy photon and electron beams *Med. Phys.* **26** 1847-70

Andreo P and Brahme A 1986 Stopping power data for high-energy photon beams *Phys. Med. Biol.* **31** 839-58

Andreo P, Burns D T, Hohlfeld K, Huq M S, Kanai T, Laitano F, Smythe V G and Vynckier S 2000 Absorbed Dose Determination in External Beam Radiotherapy: An International Code of Practice for Dosimetry Based on Standards of Absorbed Dose to Water. In: *Technical Report Series No. 398*, (Vienna: International Atomic Energy Agency)

Andreo P and Nahum A 2007 *Handbook of radiotherapy physics: theory and practice* (Boca Raton, FL: CRC Press) pp 385-427

Australian Institute of Health and Welfare 2012 Cancer incidence projections Australia, 2011 to 2020. (Canberra: Australian Institute of Health and Welfare) (available at http://www.aihw.gov.au/publication-detail/?id=10737421461, accessed 18 May 2015)

Briesmeister J F 2000 MCNPTM-A general Monte Carlo N-particle transport code *Version 4C, LA-13709-M, Los Alamos National Laboratory*

Butler D, Ramanathan G, Oliver C, Cole A, Lye J, Harty P, Wright T, Webb D and Followill D 2014 Direct megavoltage photon calibration service in Australia *Australas. Phys. Eng. Sci. Med.* **37** 753-61

Consultative Committee for Ionizing Radiation (CCRI) 2014 Calorimetric comparison of absorbed dose to water at high energies: BIPM key comparison BIPM.RI(I)-K6 protocol 1.8. (Sèvres: Bureau International des Poids et Mesures), available online at http://kcdb.bipm.org/appendixB/appbresults/bipm.ri(i)-K6/BIPM.RI(I)-K6_Technical_Protocol.pdf, accessed 25 July 2015

Delaney G, Jacob S, Featherstone C and Barton M 2005 The role of radiotherapy in cancer treatment *Cancer* **104** 1129-37

Delaunay F, de Carlan L, Daures J, Garcia T, Gouriou J, Le Roy M, Lourenco V, Ostrowsky A, Sommier L, Sorel S and Vermesse D 2011 LNE-LNHB realisation of the unit of the absorbed-dose-to-water under IMRT conditions. In: *Presentation at Conference on Advanced Metrology for Cancer Therapy,Braunschweig Germany,* (available at http://vic-px04.arpansa.local:8080/ProgressMessages/part0302.pdf?proxy=172.16.6.191&action=complete&index=69&id=45971801&filename=part0302.pdf, accessed 15 May 2014)

Delaunay F 2013 LNE-LNHB Highlights 2011-2012, Report to the 2013 CCRI(I) meeting.

Dieterich S and Sherouse G W 2011 Experimental comparison of seven commercial dosimetry diodes for measurement of stereotactic radiosurgery cone factors *Med. Phys.* **38** 4166-73

Domen S R and Lamperti P J 1974 A heat-loss-compensated calorimeter: theory, design, and performance *J. Res. Nat. Bur. Stand. A Phys. Chem. A* **78** 595-610

Elekta Limited 2009 *private communication with manufacturer per confidentiality agreement*

González-Castaño D, Hartmann G, Sánchez-Doblado F, Gómez F, Kapsch R, Pena J and Capote R 2009 The determination of beam quality correction factors: Monte Carlo simulations and measurements *Phys. Med. Biol.* **54** 4723-41

Guerra A S, Laitano R F and Pimpinella M 1996 Characteristics of the absorbed dose to water standard at ENEA *Physics in Medicine and Biology* **41** 657-74

Guerra A S, Caporali C, Laitano R F and Pimpinella M 2007 Improvements in absorbed dose standards at INMRI-ENEA (Italy). In: *Workshop on Absorbed Dose and Air Kerma Primary Standards,* (Paris, 9-11 May 2007)

Hartmann Siantar C L, Walling R S, Daly T P, Faddegon B, Albright N, Bergstrom P, Bielajew A F, Chuang C, Garrett D, House R K, Knapp D, Wieczorek D J and Verhey L J 2001 Description and dosimetric verification of the PEREGRINE Monte Carlo dose calculation system for photon beams incident on a water phantom *Med. Phys.* **28** 1322-37

Hirayama H, Namito Y, Nelson W R, Bielajew A F, Wilderman S J and Michigan U 2005 The EGS5 code system. (United States: Department of Energy)

Hubbell J H 1982 Photon mass attenuation and energy-absorption coefficients *Int. J. Appl. Radiat. Isot.* **33** 1269-90

Huntley R B, Boas J F and Van der Gaast H 1998 The 1997 determination of the Australian standards of exposure and absorbed dose at ^{60}Co. In: *Technical Report No. 126,* (Yallambie: Australian Radiation Protection and Nuclear Safety Agency)

ISO/IEC 2008 *Guide to the expression of uncertainty in measurement* (Geneva: International Organization for Standardization)

Johansson K, Mattsson L, Lindborg L and Svensson H 1978 *National and International Standardization of Radiation Dosimetry,* (Vienna: IAEA) pp 243-69

Katumba M F 2010 Experimental determination of beam quality correction factors in clinical high-energy photon and electron beams. (Johannesburg: University of Witwatersand)

Kawrakow I 2000 Accurate condensed history Monte Carlo simulation of electron transport. I. EGSnrc, the new EGS4 version *Med. Phys.* **27** 485-98

Kawrakow I, Rogers D and Walters B 2004 Large efficiency improvements in BEAMnrc using directional bremsstrahlung splitting *Med. Phys.* **31** 2883-98

Key Comparison Database 2014 The BIPM Key Comparison Database is available online at http://kcdb.bipm.org/, accessed 25 July 2015

Krauss A and Kapsch R-P 2007 Calorimetric determination of k_Q factors for NE 2561 and NE 2571 ionization chambers in 5 cm × 5 cm and 10 cm × 10 cm radiotherapy beams of 8 MV and 16 MV photons *Phys. Med. Biol.* **52** 6243-59

Krauss A and Kapsch R P 2014 Experimental determination of k_Q factors for cylindrical ionization chambers in 10 cm × 10 cm and 3 cm × 3 cm photon beams from 4 MV to 25 MV *Phys. Med. Biol.* **59** 4227-46

Lagerwaard F J, Verstegen N E, Haasbeek C J A, Slotman B J, Paul M A, Smit E F and Senan S 2012 Outcomes of Stereotactic Ablative Radiotherapy in Patients With Potentially Operable Stage I Non-Small Cell Lung Cancer *Int. J. Radiat. Oncol. Biol. Phys.* **83** 348-53

Libby B, Siebers J and Mohan R 1999 Validation of Monte Carlo generated phase-space descriptions of medical linear accelerators *Med. Phys.* **26** 1476-83

Lide D R (ed.) 2009 *CRC Handbook of Chemistry and Physics 2009-2010: A Ready-Reference Book of Chemical and Physical Data* (Boca Raton, FL: CRC press)

Lye J E 2012 Monte Carlo evaluation of the dosimetric uncertainty in matched 6 MV Elekta and Varian linear accelerators. (Melbourne: RMIT University), available online at http://researchbank.rmit.edu.au/eserv/rmit:160350, accessed 25 July 2015

Lye J E, Butler D J, Ramanathan G and Franich R D 2012 Spectral differences in 6 MV beams with matched PDDs and the effect on chamber response *Phys. Med. Biol.* **57** 7599-614

Lye J E, Butler D J, Franich R D, Harty P D, Oliver C P, Ramanathan G, Webb D V and Wright T 2013 Direct MC conversion of absorbed dose to graphite to absorbed dose to water for ^{60}Co radiation *Radiat. Prot. Dosim.* **155** 100-9

Ma C and Li J 2011 Dose specification for radiation therapy: dose to water or dose to medium? *Phys. Med. Biol.* **56** 3073-89

Mayles P, Nahum A and Rosenwald J C (eds.) 2007 *Handbook of radiotherapy physics: theory and practice* (Boca Raton, FL: CRC Press)

McCall R C, McIntyre R D and Turnbull W G 1978 Improvement of linear accelerator depth-dose curves *Med. Phys.* **5** 518-24

McEwen M, Kawrakow I and Ross C 2008 The effective point of measurement of ionization chambers and the build-up anomaly in MV x-ray beams *Med. Phys.* **35** 950-8

McEwen M R 2010 Measurement of ionization chamber absorbed dose k_Q factors in megavoltage photon beams *Med. Phys.* **37** 2179-93

McEwen M, DeWerd L, Ibbott G, Followill D, Rogers D W, Seltzer S and Seuntjens J 2014 Addendum to the AAPM's TG-51 protocol for clinical reference dosimetry of high-energy photon beams *Med. Phys.* **41** 041501

Mesbahi A, Fix M, Allahverdi M, Grein E and Garaati H 2005 Monte Carlo calculation of Varian 2300C/D Linac photon beam characteristics: a comparison between MCNP4C, GEANT3 and measurements *Appl. Radiat. Isot.* **62** 469-77

Morishita Y, Kato M, Takata N, Kurosawa T, Tanaka T and Saito N 2013 A standard for absorbed dose rate to water in a ^{60}Co field using a graphite calorimeter at the National Metrology Institute of Japan *Radiat. Prot. Dosim.* **154** 331-9

Muir B R and Rogers D W O 2010 Monte Carlo calculations of k_Q, the beam quality conversion factor *Med. Phys.* **37** 5939-50

Nahum A 2007 *Handbook of radiotherapy physics theory and practice,* (Boca Raton, FL: Taylor & Francis) pp 89-121

Nahum A and Kutcher G 2007 *Handbook of radiotherapy physics theory and practice,* (Boca Raton, FL: Taylor & Francis) pp 731-71

Nutbrown R F, Duane S, Shipley D R and Thomas R A S 2002 Evaluation of factors to convert absorbed dose calibrations from graphite to water for the NPL high-energy photon calibration service *Phys. Med. Biol.* **47** 441-54

Oldham M 2007 *Handbook of radiotherapy physics theory and practice,* (Boca Raton, FL: Taylor & Francis) pp 321-31

Palm Å and Mattsson O 2002 Experimental determination of beam quality conversion factors k_Q in clinical photon beams using ferrous sulphate (Fricke) dosimetry *Med. Phys.* **29** 2756-62

Pearce J A D, Shipley D R and Duane S 2011 Transfer of the UK absorbed dose primary standard for photon beams from the research linac to the clinical linac at NPL *Metrologia* **48** 365-74

Petti P L, Goodman M S, Gabriel T A and Mohan R 1983 Investigation of buildup dose from electron contamination of clinical photon beams *Med. Phys.* **10** 18-24

Physikalisch-Technische Bundesanstalt (PTB) 2008 Chamber-to-chamber variation of the energy dependence of the response of ionization chambers (available at: https://www.ptb.de/cms/en/service-seiten/news/newsdetails.html?tx_news_pi1%5Bnews%5D=4498&tx_news_pi1%5Bcontroller%5D=News&tx_news_pi1%5Baction%5D=detail&tx_news_pi1%5Bday%5D=29&tx_news_pi1%5Bmonth%5D=9&tx_news_pi1%5Byear%5D=2008&cHash=165021fd0f08d84a8812bb4c6734cbbd, accessed 25 July 2015)

Picard S, Burns D T, Roger P, Allisy-Roberts P J, McEwen M R, Cojocaru C D and Ross C K 2010 Comparison of the standards for absorbed dose to water of the NRC and the BIPM for accelerator photon beams *Metrologia* **47** 06025

Picard S, Burns D T, Roger P, Allisy-Roberts P J, Kapsch R P and Krauss A 2011 Key comparison BIPM.RI(I)-K6 of the standards for absorbed dose to water of the PTB, Germany and the BIPM in accelerator photon beams *Metrologia* **48** 06020

Picard S, Burns D T, Roger P, Bateman F B, Tosh R E and Chen-Mayer H 2013a Key comparison BIPM.RI(I)-K6 of the standards for absorbed dose to water of the NIST, USA and the BIPM in accelerator photon beams *Metrologia* **50** 06004

Picard S, Burns D T, Roger P, Delaunay F, Gouriou J, Roy M L, Ostrowsky A, Sommier L and Vermesse D 2013b Key comparison BIPM.RI(I)-K6 of the standards for absorbed dose to water of the LNE–LNHB, France and the BIPM in accelerator photon beams *Metrologia* **50** 06015

Picard S, Burns D T and Los Arcos J M 2013c Establishment of degrees of equivalence of national primary standards for absorbed dose to water in accelerator photon beams *Metrologia* **50** 06016

Picard S, Burns D T, Roger P, Harty P D, Ramanathan G, Lye J E, Wright T, Butler D J, Cole A, Oliver C and Webb D V 2014 Key comparison BIPM.RI(I)-K6 of the standards for absorbed dose to water of the ARPANSA, Australia and the BIPM in accelerator photon beams *Metrologia* **51** 06006

Picard S, Burns D T, Roger P, Duane S, Bass G A, Manning J W and Shipley D R 2015 Key comparison BIPM.RI(I)-K6 of the standards for absorbed dose to water at 5 g cm^{-2} and 7 g cm^{-2} of the NPL, United Kingdom and the BIPM in accelerator photon beams *Metrologia* **52** 06010

Pruitt J S and Loevinger R 1982 The photon-fluence scaling theorem for Compton-scattered radiation *Med. Phys.* **9** 176-9

Ramanathan G, Harty P, Wright T, Lye J, Butler D, Webb D and Huntley R 2014 The Australian Primary Standard for absorbed dose to water (graphite calorimeter). In: *Technical Report No. 166*, (Yallambie: Australian Radiation Protection and Nuclear Safety Agency), available online at http://arpansa.gov.au/pubs/technicalreports/tr166.pdf, accessed 25 July 2015

Rangel A, Ploquin N, Kay I and Dunscombe P 2007 Towards an objective evaluation of tolerances for beam modeling in a treatment planning system *Phys. Med. Biol.* **52** 6011-25

Rogers D 2006 Fifty years of Monte Carlo simulations for medical physics *Phys. Med. Biol.* **51** R287-301

Rogers D W O, Walters B and Kawrakow I 2007 BEAMnrc Users Manual. (Ottawa: National Research Council of Canada)

Salvat F, Fernandez-Varea J M and Sempau J 2009 PENELOPE-2008: A code system for Monte Carlo simulation of electron and photon transport. In: *Nuclear Energy Agency No. 6416*, (Paris: Organisation for Economic Co-operation and Development/ Nuclear Energy Agency), available online at https://www.oecd-nea.org/science/pubs/2009/nea6416-penelope.pdf, accessed 25 July 2015

Scott A J D, Nahum A E and Fenwick J D 2009 Monte Carlo modeling of small photon fields: Quantifying the impact of focal spot size on source occlusion and output factors, and exploring miniphantom design for small-field measurements *Med. Phys.* **36** 3132-44

Seco J and Verhaegen F (eds.) 2013 *Monte Carlo techniques in radiation therapy* (Boca Raton, FL: CRC Press)

Seuntjens J P, Ross C K, Shortt K R and Rogers D W O 2000 Absorbed-dose beam quality conversion factors for cylindrical chambers in high energy photon beams *Med. Phys.* **27** 2763-79

Seuntjens J, Olivares M, Evans M and Podgorsak E 2005 Absorbed dose to water reference dosimetry using solid phantoms in the context of absorbed-dose protocols *Med. Phys.* **32** 2945-53

Seuntjens J and Duane S 2009 Photon absorbed dose standards *Metrologia* **46** S39-58

Sheikh-Bagheri D, Rogers D W O, Ross C K and Seuntjens J P 2000 Comparison of measured and Monte Carlo calculated dose distributions from the NRC linac *Med. Phys.* **27** 2256-66

Shimizu M, Morishita Y, Kato M, Tanaka T, Kurosawa T, Takata N, Saito N, Ramanathan G, Harty P, Oliver C, Wright T and Butler D 2015 Comparison of the NMIJ and the ARPANSA standards for absorbed dose to water in high-energy photon beams *Radiat. Prot. Dosim.* **164** 181-6

Stucki G, Schafer R and Quintel H 2003 The METAS photon-beam primary standard sealed water calorimeter. In: *Proc. Australian Radiation Protection and Nuclear Safety Agency Workshop on Recent Advances in Absorbed Dose Standards,* (Yallambie, Victoria 19-21 Aug 2003: http://www.arpansa.gov.au/news/events/absdos.cfm)

Tessier F and Kawrakow I 2010 Effective point of measurement of thimble ion chambers in megavoltage photon beams *Med. Phys.* **37** 96-107

Thomas R A S, Duane S and Simon M 2008 Measurements of k_Q factors, ion recombination, polarity and sleeve effects of Farmer type chambers calibrated in terms of absorbed dose to water at NPL. In: *Radiotherapy Standards Users' Group,* (Teddington, UK: NPL)

Verhaegen F and Seuntjens J 2003 Monte Carlo modelling of external radiotherapy photon beams *Phys. Med. Biol.* **48** R107-64

Walters B, Kawrakow I and Rogers D W O 2007 DOSXYZnrc Users Manual. (Ottawa: National Research Council of Canada)

Wise K N 2001 Monte Carlo methods used to develop the Australian absorbed dose standard. In: *Technical Report No. 132,* (Yallambie: Australian Radiation Protection and Nuclear Safety Agency)

Witzani J, Duftschmid K, Strachotinsky C and Leitner A 1984 A graphite absorbed-dose calorimeter in the quasi-isothermal mode of operation *Metrologia* **20** 73-9

Wulff J, Heverhagen J and Zink K 2008 Monte-Carlo-based perturbation and beam quality correction factors for thimble ionization chambers in high-energy photon beams *Phys. Med. Biol.* **53** 2823-36